REPORT DOCUMENTATION PAGE	*Form Approved* *OMB No. 0704-0188*

The public reporting burden for this collection of information is estimated to average 1 hour per response, including the time for reviewing instructions, searching existing data sources, gathering and maintaining the data needed, and completing and reviewing the collection of information. Send comments regarding this burden estimate or any other aspect of this collection of information, including suggestions for reducing the burden, to the Department of Defense, Executive Services and Communications Directorate (0704-0188). Respondents should be aware that notwithstanding any other provision of law, no person shall be subject to any penalty for failing to comply with a collection of information if it does not display a currently valid OMB control number.

PLEASE DO NOT RETURN YOUR FORM TO THE ABOVE ORGANIZATION.

1. REPORT DATE *(DD-MM-YYYY)* 28-05-2010	**2. REPORT TYPE** Final Performance Report	**3. DATES COVERED** *(From - To)* 1 July, 2004 - 28 February, 2010

4. TITLE AND SUBTITLE (DARPA) Nonlinear Optics at Low Light Levels	**5a. CONTRACT NUMBER** FA9550-04-1-0442
	5b. GRANT NUMBER
	5c. PROGRAM ELEMENT NUMBER
6. AUTHOR(S) S. E. Harris	**5d. PROJECT NUMBER**
	5e. TASK NUMBER
	5f. WORK UNIT NUMBER
7. PERFORMING ORGANIZATION NAME(S) AND ADDRESS(ES) Leland Stanford Junior University 651 Serra Street Stanford, CA 94305-6215	**8. PERFORMING ORGANIZATION REPORT NUMBER**
9. SPONSORING/MONITORING AGENCY NAME(S) AND ADDRESS(ES) AF Office of Scientific Research (AFOSR) 875 North Randolph Street Arlington, VA 22203-1768	**10. SPONSOR/MONITOR'S ACRONYM(S)**
	11. SPONSOR/MONITOR'S REPORT NUMBER(S) AFRL-SR-AR-TR-10-0274

12. DISTRIBUTION/AVAILABILITY STATEMENT

Unlimited.

13. SUPPLEMENTARY NOTES

14. ABSTRACT

The principal accomplishments of this program were: 1)The use of slow light to demonstrate a source of biphotons with temporal lengths as long as four hundred nanoseconds and wavepacket lengths exceeding a football field. 2) The first observation of optical precursors at the single photon level. 3) The first electrooptic shaping and modulation of single photons. 4) The demonstration of the modulation of biphotons and the invention and demonstration of a Fourier technique for measuring the temporal length of biphotons by using fast modulators instead of fast detectors. 5) The prediction and first demonstration of a novel quantum effect that we have termed as nonlocal modulation, and 6) the demonstration of spread spectrum technology to allow the hiding and regeneration of single photons. These accomplishments would not have been possible without the joint support of the Air Force Office of Scientific Research and the Army Research Office.

15. SUBJECT TERMS

electromagnetically induced transparency, photon interactions with atoms, nonclassical states of the electromagnetic field, including entangled photon states, quantum engineering and measurements, parametric down conversion and production of entangled photons.

16. SECURITY CLASSIFICATION OF:			**17. LIMITATION OF ABSTRACT**	**18. NUMBER OF PAGES**	**19a. NAME OF RESPONSIBLE PERSON**
a. REPORT	**b. ABSTRACT**	**c. THIS PAGE**		83	**19b. TELEPHONE NUMBER** *(Include area code)*

Reset

Final Performance Report

(DARPA) NONLINEAR OPTICS AT LOW LIGHT LEVELS

Grant/Contract FA9550-04-1-0442

Prepared for

DARPA
and
AIR FORCE OFFICE OF SCIENTIFIC RESEARCH

For the Period
JULY 2004 to FERUARY 2010

Submitted by

S. E. Harris[1], Principal Investigator

Edward L.Ginzton Laboratory
Stanford University

---

[1] seharris@stanford.edu

Contents

1 Executive Summary 2

2 First Experiments 5

3 Subnatural Linewidth Biphoton Generation with a 2-D MOT 8

4 Theory of EIT- based Paired Photon Generation 13

5 Electro-Optic Modulation of Single Photons 14

6 Modulation and Measurement of Time-Energy Entangled Photons 19

7 Observation of Nonlocal Modulation with Entangled Photons 24

8 Hiding Single Photons with Spread Spectrum Technology 35

9 Joint Support 40

APPENDIX 41

A DARPA Supported Publications During Grant Period 41

B Construction and Operation of the 2-D MOT 43

C Optical Layout 44

D Lasers 45

E Vacuum System 49

F Experimental Cycle 50

G MOT Characteristics 52

H Chapter 4 of Pavel Kolchin's Dissertation 54

1 Executive Summary

Our work on this program began in 2004 with a long-shot: We would attempt to construct a new first-of-kind source of biphotons and conditional single photons that have a linewidth on the scale of atomic transitions, that is about several MHz. Such photons are about a microsecond long. A single photon therefore has a physical length equal to that of a football field. Our proposed technique was based on the use of electromagnetically induced transparency and slow light, where basically the temporal length of the biphoton is equal to the physical length of our atomic sample (about two cm) divided by the optical group velocity. This idea worked almost immediately and the publication "Generation of Paired Photons with Controllable Waveforms," appeared in Physical Review Letters in May of 2005.

As time progressed, the objectives of this program, with joint support from AFOSR and ARO, was aimed at both improving the performance of this new light source, and also at demonstrating novel effects that are only possible with long biphotons. Work on a new quantum effect termed as nonlocal modulation and requiring the use of short biphotons was included in the program.

We begin by summarizing a key property of time-energy entangled biphotons. This is: if an observer at point A chooses to measure the frequency of an arriving photon he will then know to high accuracy the frequency of the photon which will be measured by an observer at point B. But instead, if the observer at point A chooses to measure the time of arrival of a photon at his location, he will then know, again to high accuracy, the time of arrival of the photon at point B. The accuracy of these measurements is not limited by the Heisenberg uncertainty principle.

We turn next to what is meant by long and short. Typical biphotons as generated by nonlinear optical crystals have temporal lengths in the range of between 0.1 ps and 10 ps. Such photons are not resolvable by presently existing photo detectors. These detectors, measure whether or not a photon is present, but may not be used to examine the functional form of the photonic wave packet.

A key accomplishment of the present program was the generation of photons whose length could be continuously varied from 50 to 900 ns. Of importance, the line width of these photons is less than the natural linewidth of the rubidium vapor that was used to produce them. This is important because optical nonlinearities when produced using electromagnetically induced transparency continue to increase in the subnatural linewidth regime and in the absence of dephasing may be made arbitrarily large.

We mention a surprise that occurred during this work. In the course of observing long biphotons with a length determined by the slow optical group velocities, we found that the photonic wave packets had a sharp leading edge spike on their front edge. Following a suggestion by Dan Gauthier we recognized that this front edge spike is a Sommerfeld-Brillouin precursor. This observation is important because it clarifies, for both slow light and fast light, that information will always be transmitted at the speed of light in vacuum.

In January 2008 we recognized that we had the capability to modulate single photons for the first time. To do this we used the Stokes photon of a biphoton pair to set the time origin for electro-optic modulation of the wave function of the anti-stokes photon. With the time origin determined, the modulator could arbitrarily modulate either the amplitude or phase of the anti-stokes photon. The technique therefore provides the technology for studying the response of atoms to shaped single-photon waveforms on a time scale comparable to the natural linewidth of target atoms.

The next step in our work in modulating biphotons was the development of a method for measuring their length using slow detectors. The essential idea is that modulation in the time domain followed by slow integration constitutes a Fourier transformation. The experimental technique is to measure the coincidence count rate between single photon counting modules as a function of an applied sinusoidal frequency. The inverse Fourier transform of the data then yields the biphoton waveform. Though this experiment was a proof of principle experiment, ultimately it could be used to measure wavepacket profile of biphotons when sufficiently fast photo detectors are not available.

In recent months we have demonstrated an important extension of our work on modulating single photons. This is the application of spread spectrum techniques at the single photon level. Spread spectrum is well known in the communications industry as a technique for avoiding interference and jamming, and at times increasing information capacity. Our work is the first demonstration of this technique to single photons. As described in this report this has allowed us to send a single photon with a known temporal shape through an environment of thousands of times more intense background photons deliberately produced by a jamming laser. We have thus shown that a single photon as used for to send a secure cryptographic key may be deliberately hidden, and recovered at the receiving end.

During the course of this work we recognized that there should be a new quantum effect that we have termed as nonlocal modulation. Assume that single and idler photons pass through sinusoidal phase modulators located at different locations. These modulators are driven at the same modulation frequency and are connected by cable such that their relative phase may be varied. After passing through the modulators the single and idler photons are dispersed, for example by a prism, and the relative positions of the single and idler photons are correlated. We find and have experimentally demonstrated : When the modulators are run with the same phase the modulation depths add; when they are run in phase opposition the modulation depths subtract. Two distant modulators with the same modulation depth and opposite phase therefore have the same frequency correlation as when both modulators are absent. This effect is entirely quantum mechanical. Mathematically it results because, quantum mechanically, one adds probability amplitudes before squaring, while classically one squares before adding.

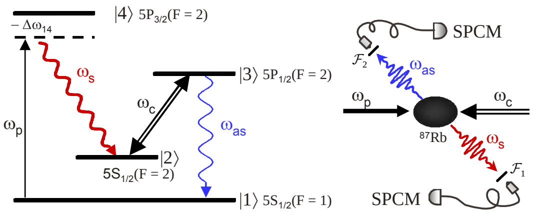

Figure 1: Energy Schematic for Biphoton Generation

2 First Experiments

Figure 1 shows an energy schematic of the process of the biphoton generation process. In the presence of two counter-propagating cw pump and coupling lasers paired spontaneous Stokes and anti-Stokes photons are generated and propagate in opposite directions. The anti-Stokes photon has a center frequency equal to that of a highly-absorbing transition in the atom. The coupling laser creates transparency and causes the anti-Stokes wave to travel at a slow and variable group velocity. This group velocity determines the width of the paired photon wave packet.

Our first experiments demonstrating the generation of 100 ns time scale biphotons were done using a standard-design all metal spherical MOT with an atom cloud with a diameter of a about 2 mm. In order to contrast with the results of the greatly improved 2D MOT described below, Figures 2 and 3 show these first results. The shape of the wave packet depends on the relation of two characteristic times that are the essence of this work. The first is a Rabi-like coherence time and the second is the group delay time. The experimental result in the regime where the Rabi time is less than the group delay time is shown in Fig. 2. One observes behavior like that of a single atom where, at $t = 0$, a Stokes photon causes the excitation of the upper state and the probability amplitude oscillates between the ground and upper state. When the group delay is sufficiently large that the delay time is longer than the Rabi time, then the wave packet approximates the correlation function of an ideal parametric emitter. Here, the width of the wave packet is approximately equal to the delay time. Figure 3 shows experiment and theory as the parameters approach, but are not quite in the ideal group delay regime.

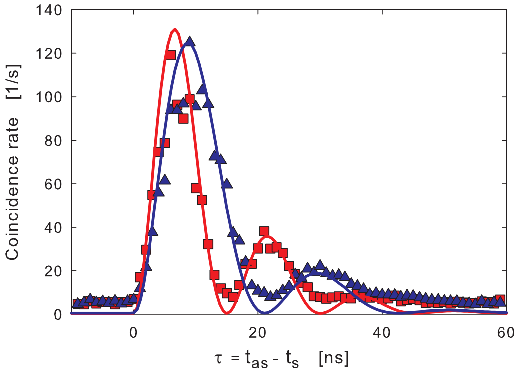

Figure 2: Generation in the oscillatory regime

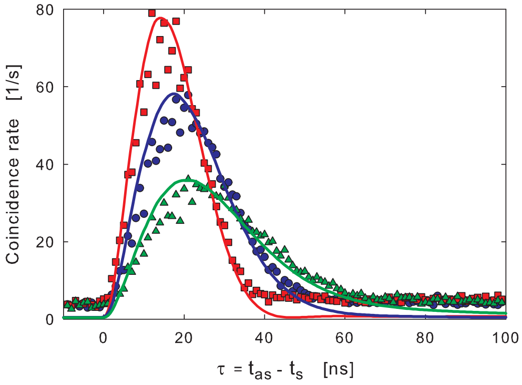

Figure 3: Generation nearing the group delay regime

In a second experiment still using the spherical trapped atom geometry, in May of 2005 we reported an improvement for generating narrow band time-energy entangled photons. Here, working in a standing wave right angle geometry, we use a single driving laser with two AOM's to parametrically pump the ^{87}Rb atoms, and also to trap and cool the Rb atoms. This technique results in a modification and narrowing of the Glauber intensity correlation function, and at the same time the elimination of Rayleigh scattering. An energy level diagram, and the geometry and timing for the experiment are shown in Fig. 4. We replace the three driving lasers of the earlier experiment with a single (Ti:Sapphire) laser. The Ti:Sapphire laser frequency is down shifted by 123.5 MHz so as to be resonant with the $|5S_{1/2}, F = 2\rangle \rightarrow |5P_{3/2}, F = 2\rangle$ transition. This frequency, denoted by ω_p, acts as

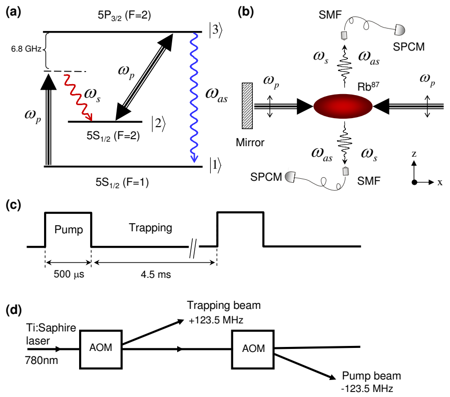

Figure 4: Energy schematic for biphoton generation using a single pumping laser. (a) Energy level diagram. (b) Geometry (c) Timing: The photon generation window of 500 μs is followed by a trapping and cooling period of 4.5 ms. (d) Pumping: The Ti:Sapphire laser is up-shifted to trap and cool atoms and down-shifted to serve as a pump for the paired photon generation process.

the coupling laser of earlier experiments and creates transparency on the $|5S_{1/2}, F = 1\rangle \rightarrow |5P_{3/2}, F = 2\rangle$ transition. This same frequency pumps the four wave down-conversion process that generates the paired photons. To cool and trap ^{87}Rb atoms the incident Ti:Sapphire laser beam is up-shifted by 123.5 MHz to 20 MHz below the $|5S_{1/2}, F = 2\rangle \rightarrow |5P_{3/2}, F = 3\rangle$ transition (not shown). This is done periodically so as to create a 10% duty cycle, with the trapping process occurring for 4.5 ms, followed by an experimental window of 500 μs. The trapping magnetic field remains on during this experimental window.

Of importance we find that the use of a retro-reflected laser for both pumping and coupling results in an unexpected change in the shape of the Glauber intensity correlation function for the Stokes and anti-Stokes photons. In the earlier Stanford work the shape of the correlation function was set by the longer of two characteristic times. These times are the group delay time between the Stokes and anti-Stokes photons, and the inverse Rabi frequency of the coupling laser. Here, because of the much larger Rabi-frequency (200 MHz) of the common pump and coupling laser, the group delay time is short and the Rabi-period dominates. We therefore expect a damped- periodic correlation function similar to that of the earlier work with a period of about 5 ns. We find experimentally and verify theoretically that the interference fringes (in the x-direction) that are caused by the counter-propagating pumping beams result in a reduction of the outer Rabi side lobes of the intensity correlation function.

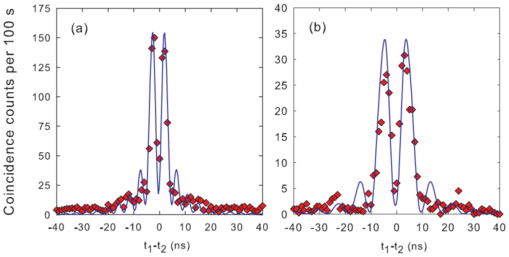

Figure 5: Coincidence count rate as a function of the delay between detected photons. (a) Pump power = 160 mW; $\Omega_{c0} = 80\gamma_{13}$ and $\Omega_{p0} = 140\gamma_{13}$. (b) Pump power = 40 mW, $\Omega_{c0} = 40\gamma_{13}$ and $\Omega_{p0} = 70\gamma_{13}$. The pump is tuned to resonance with the $|2\rangle \rightarrow |3\rangle$ transition. Data ($\diamond$) was collected over 200 s. Theoretical curves (solid lines) are scaled vertically by a common factor and are averaged over a 1 ns bin.

These results are shown in the Fig. 5 where we plot coincidence counts versus delay time between the Stokes and anti-Stokes photons. Here, the pump laser is tuned to resonance of the $|2\rangle \rightarrow |3\rangle$ transition. Since the Stokes and anti-Stokes photons are present in both fibers, the correlation function is symmetric.

3 Subnatural Linewidth Biphoton Generation with a 2-D MOT

A major breakout is this program occurred with the successful operation of a two-dimensional MOT which allowed much higher optical depth and performance in all respects. Of particular importance, it allowed, for the first time, the generation of photons having a sub-natural linewidth. Figure 6 shows both experimental configuration (geometry) and mechanism of parametric paired-photon generation. In contrast to previous (spherical) MOT, the new 2-D ^{85}Rb MOT has a cigar shaped atom cloud(~1.7 cm long and an aspect ratio of 25) and consequently a large optical depth in the longitudinal direction; moreover, its cylindrical quadrupole trapping field results in minimal longitudinal magnetic field gradient and

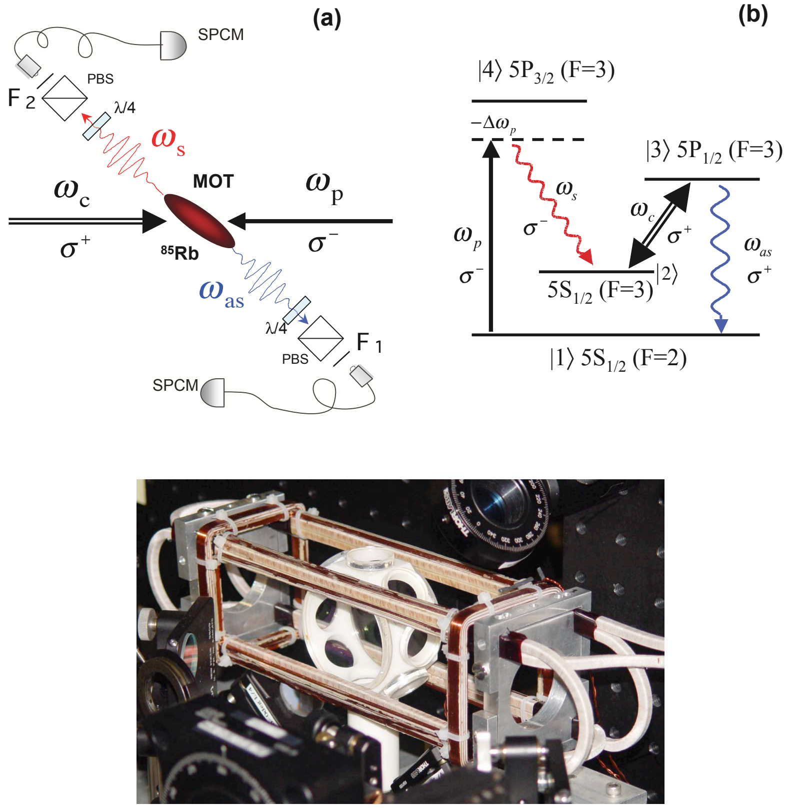
(a)
SPCM
PBS
F 2
λ/4
ω_s
MOT
ω_c
ω_p
σ^+
σ^-
^{85}Rb
ω_{as}
λ/4
PBS
F 1
SPCM
(b)
|4⟩ 5P$_{3/2}$ (F=3)
$-\Delta\omega_p$
|3⟩ 5P$_{1/2}$ (F=3)
ω_s
σ^-
ω_c
σ^+
ω_p
σ^-
ω_{as}
σ^+
5S$_{1/2}$ (F=3)
|2⟩
|1⟩ 5S$_{1/2}$ (F=2)

Figure 6: **Upper:** Biphoton generation in a double-Λ system. (a) Experimental configuration. F_1 and F_2 are narrow-band optical frequency filters. (b) ^{85}Rb energy level diagram. In the presence of counter-propagating pump (ω_p) and coupling (ω_c) beams, Stokes (ω_s)and anti-Stokes, (ω_{as}) photons are generated into opposing single-mode fibers. **Lower:** 2-D MOT apparatus. The vacuum cell is 6 cm size ceramic structured octagon. The cell is located in the middle of water cooled trapping coil(racetrack-shaped cage).

hence greatly reduces the inhomogeneous Zeeman broadening of the m-states of the $5S_{1/2}$ level. The experimental cycle comprises 4.5 ms of trapping time and 0.5 ms paired photon generation window. At the end of the trapping cycle, the rubidium cloud is prepared in $5S_{1/2}$ level by turning off the repumping laser 0.3 ms before turning off the trapping laser; counter-propagating, circularly polarized, cw pump (ω_p) and coupling (ω_c) lasers are subsequently turned on and phase-matched, paired Stokes (ω_s) and anti-Stokes (ω_{as}) photons are spontaneously generated and propagate in opposite directions as shown in the figure.

The optical depth of the 2-D ^{85}Rb MOT can be varied up to 62, which gives us enough parameter space to verify the relation between the optical group delay and the length of

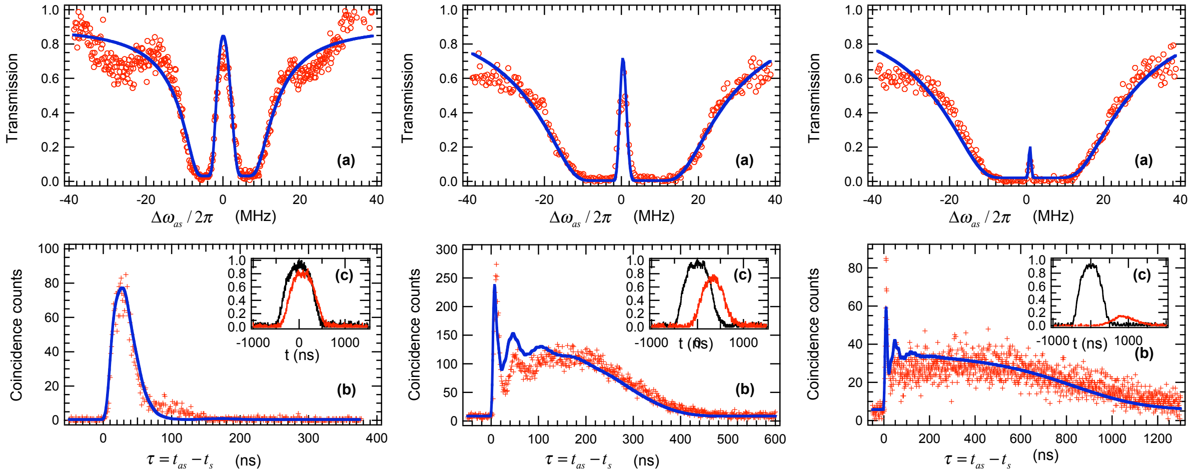

Figure 7: Biphoton wave packet data for three slow group delay cases. The upper row plots are anti-Stokes EIT scan data(○) and EIT fit(blue curve), the lower row plots are paired-photon coincidence count data(+) and predicted wave packet shape with time bin width of 1 ns for 800 s(lower row). Propagation delay of anti-Stokes pulse(red traces in inserts of lower row plots) are also presented for three slow group delay((τ_g) cases. Experimental parameters are: **Left:** ($\tau_g \sim 50ns$) OD=7, $\Omega_c = 4.20\gamma_{13}$, $\Omega_p = 1.16\gamma_{13}$, and $\Delta_p = 48.67\gamma_{13}$. **Middle:** ($\tau_g \sim 320ns$) OD=53, $\Omega_c = 4.20\gamma_{13}$, $\Omega_p = 1.16\gamma_{13}$, and $\Delta_p = 48.67\gamma_{13}$. **Right:** ($\tau_g \sim 900ns$) OD=53, $\Omega_c = 2.35\gamma_{13}$, $\Omega_p = 1.16\gamma_{13}$, and $\Delta_p = 48.67\gamma_{13}$.

the biphoton waveform. Figure 7 shows sets of anti-Stokes EIT scan and paired-photon coincidence counts for three anti-Stokes EIT group delay cases, which is controlled by varying the optical depth and the coupling laser power($\tau_g \simeq (2\gamma_{13}/|\Omega_c|^2)N\sigma L$, where $N\sigma L$ is the optical depth and γ_{13} is the dephasing rate of level $|3\rangle$). The trapping laser used for these experimental runs has a power of 160 mW, a beam diameter of 2 cm, and is red detuned by 20 MHz from the $|5S_{1/2}, F = 3\rangle \rightarrow |5P_{3/2}, F = 4\rangle$ transition. A repumping laser is locked to the $|5S_{1/2}, F = 2\rangle \rightarrow |5P_{3/2}, F = 2\rangle$ transition, has a power of 80 mW, and overlaps one of six trapping beams. The pump laser is circularly polarized (σ^-), has a $1/e^2$ diameter of 1.46 mm, and is blue detuned from the $|1\rangle \rightarrow |4\rangle$ transition by 146 MHz, i.e. $\Delta_p = 48.67\gamma_{13}$. The coupling laser is circularly polarized (σ^+), has a $1/e^2$ beam diameter of 1.63 mm and is on resonance with the $|2\rangle \rightarrow |3\rangle$ transition. The counter-propagating pump and coupling beams are collinear and set at a 2 degree angle from the longitudinal axis of the MOT. The Stokes (σ^-) and anti-Stokes (σ^+) photons are coupled into opposing single mode fibers after passage through $\lambda/4$ wave plates and polarization beam splitters (PBS). The Stokes and anti-Stokes fiber coupling efficiency is 70% and the $1/e^2$ waist diameter of their foci is 220 μm.

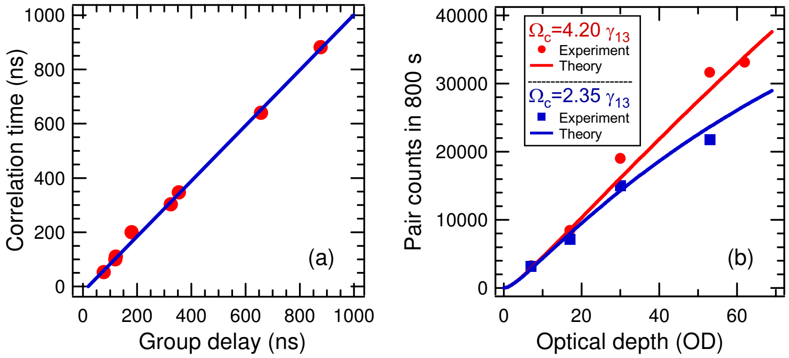

Figure 8: (a) Measured correlation time vs measured anti-Stokes group delay. The solid line is a linear least squares fit. (b) Paired counts in a 1 ns bin in 800 s as a function of the optical depth.

As shown in Fig. 7, the temporal length of biphoton wavepacket generated in high OD case are much longer(by more than one order) than previously reported in our phase I research. It also means that the generated biphoton has much narrowed bandwidth. The predicted biphoton packet waveforms in lower row plots of Fig. 7 are computed with all parameters obtained from the EIT measurements and vertically scaled to fit the experimental data. The calculated biphoton linewidths are 9.66, 2.36 and 0.75 MHz respectively. These linewidths are comparable to the measured EIT bandwidths and in the latter two cases are less than the 6 MHz natural linewidth of Rb D line. The biphoton generation now is in the linear group delay regime where $\tau_g > \tau_r$ and the correlation width directly follows group delay time. This is shown in Fig. 8(a).

Having taken into account the filter and etalon transmissions, the fiber to fiber coupling efficiency, the detector quantum efficiencies and the duty cycle. For the conditions of Fig. 7, we observe a total of 3213, 31674, and 22000 paired counts in 800 seconds, which correspond to generation rates of 1275, 12569, and 8730 pair/s, respectively. Higher generation rates can be achieved by increasing the pump laser power. With $\Omega_p = 6.88\gamma_{13}$, the paired photon generation rates are 4.0×10^4 and 9.0×10^4 pair/s at OD=17 and 30, respectively. Figure 8(b) shows that the number of paired counts varies linearly with the optical depth. Though the generation rate per spectral bandwidth varies as the square of the optical depth, the bandwidth reduces linearly with this depth leading to the linear dependence. Experimentally, under optimum conditions, we observe 74% of the Stokes photons to be paired. We also observe that all of the correlation data violate the Cauchy-Schwarz inequality by as much as a factor of 11600.

It is noticeable that there is a sharp peak at the leading edge of the correlation data generated for high optical depth case as shown in lower plots in middle and right column of Fig. 7. This feature is Sommerfeld-Brillouin precursor type as in the case for propagating classical wave packets. The physical picture is the following: the detectors register biphoton coincidence counts versus the time $\tau = t_{as} - t_s$; the earliest portion of the biphoton wave packet comes from the high frequency portion of the spectrum, which is not in the range of large group delay, and is thought of as the Sommerfeld precursor. At slightly later times the low frequency Brillouin components arrive at the detector and beat with the simultaneously arriving high frequency components. Though precursors are now understood in the optical region and have even been observed long ago with correlated gamma-ray photons, our work reports the first observation of precursors as measured by single photon correlation.

For more details please see: 1) Shengwang Du, Pavel Kolchin, Chinmay Belthangady, G. Y. Yin, and S. E. Harris, "Subnatural Linewidth Biphotons with Controllable Temporal Length," *Phys. Rev. Lett.* **100**, 183603 (May, 2008); 2) Shengwang Du, Pavel Kolchin, Chinmay Belthangady, G. Y. Yin, and S. E. Harris, "Observation of Optical Precursors at the Biphoton Level," *Optics Letters* **33**, 2149 (September, 2008).

4 Theory of EIT- based Paired Photon Generation

Our theoretical model is based on paired photon generation in the double-lambda atomic system. We first reexamine the conditions required for the system to operate in the group delay regime. We find that the optical depth of the atomic system has to be sufficiently high in order to avoid the filtering of the generation bandwidth of paired photons by the transparency window. Second, we have extended the theoretical treatment beyond the ground state approximation. This allows us to properly include and analyze the effect of Langevin noise fluctuation on the atomic system and solve the problem of its return to the ground state after the emission of Stokes and anti-Stokes photon pairs. We also addressed the important questions: 1) "What are the effects of the optical thickness of the atomic sample on paired and single photon generation?" 2) "Does every Stokes photon have its paired anti-Stokes photon?"

With low parametric gain and high optical depth we show that the system can produce highly correlated photon pairs. The shape of the intensity correlation function and the emission bandwidth depend on the coupling laser Rabi frequency and the optical depth of the atomic sample. Compared to SPDC, paired photon generation in the double-lambda atomic system is affected by Raman gain in the Stokes channel and EIT in the anti-Stokes channel. EIT, through the absorption at the poles, cuts the emission bandwidth. In order to enter a regime where the EIT window is sufficiently large and therefore the emission bandwidth is controlled to a large extent by the phase-matching process in the presence of large group delay, the optical depth of the atomic sample has to be larger than 10. High optical depth substantially reduces the influence of Langevin noise fluctuations and Raman scattering on paired photon generation so that the Stokes and anti-Stokes photons are generated mostly in pairs.

For more details please see: P. Kolchin, "Electromagnetically-Induced-Transparency-Based Paired Photon Generation," Phys. Rev. A 75, 033814 (March 2007). Kolchin's dissertation chapter 4 "Theory of EIT based Paired Photon Generation" is included in this report as Appendix C.

5 Electro-Optic Modulation of Single Photons

A highlight of our work on this DARPA program has been the demonstration of conditional shaping of single photon waveforms using electro-optic modulators. We use the Stokes photon of a biphoton pair to set the time origin for electro-optic modulation of the wave function of the anti-Stokes photon. This technique allows arbitrary control of both phase and amplitude of single photons. A key requirement for this modulation scheme is that the temporal length of biphoton wavepacket, which is represented by correlation time in experiment, is much longer than modulation response time designed for experiment. The subnatural linewidth biphoton source described in the previous section producing biphotons with correlation times adjustable in the 50-900 ns range is ideally suited for this application. Our single photon counting modules(about 350 ps of timing resolution) and data system has fast enough temporal resolution to observe AM modulation in this work.

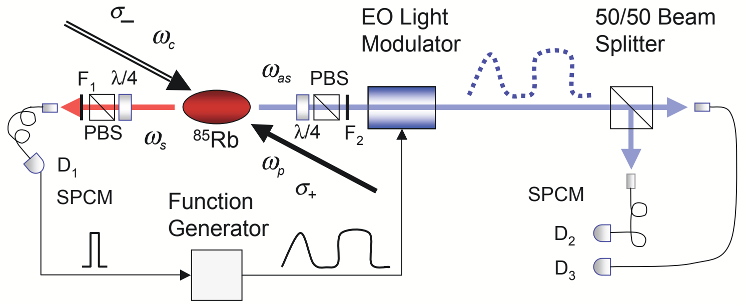

Figure 9: Schematic of paired photon generation and conditional modulation. A Stokes photon detected by an SPCM sets the time origin for shaping the anti-Stokes photon with an electro-optic modulator. To within the accuracy of the SPCM, this allows shaping of both the amplitude and phase of the anti-Stokes photon.

Figure 9 shows the schematic of the experiment. We use counterpropagating cw pump and coupling lasers to generate time-energy entangled pairs of Stokes and anti-Stokes photons which propagate in opposite directions and are collected into single mode fibers as described in section A. The detection of the Stokes photon at D1 sets the time origin for firing the function generator that drives the electro-optic modulator which in turn modulates the anti-Stokes photon. Verification of the single photon nature of the modulated anti-Stokes photon is done using a 50-50 beam splitter and detectors D2 and D3. Their coincidence data $G_{23}^{(2)}(\tau)$ is expected to show a dip at $\tau = 0$ proving nonclassical nature of modulated anti-Stokes signal.

The electro-optic amplitude modulator consists of phase modulators in both arms of a Mach-Zehnder (MZ) interferometer. The degree of phase control in both arms depends on the type of the modulator. We use a z-cut modulator that requires $V_\pi = 1.75$ volts to cause the π phase shift required to go from minimum to maximum transmission and can be operated at a maximum frequency of 10 GHz. One port of the output beam splitter of the MZ interferometer is terminated so that the portion of the photon wave function that is not transmitted is lost. In general, if a Stokes photon is detected at time t_1, and the modulator is activated conditioned on this detection then, in the Heisenberg picture, the anti-Stokes operator at the output of the modulator is related to the input operator by $\hat{a}_{out}(t_2) = \int g(t_2, t_2')\hat{a}_{in}(t_2')dt_2'$. If there are no dispersive elements, then to within an unimportant phase factor we may write $\hat{a}_{out}(t_2) = m(\tau)\hat{a}_{in}(t_2)$. The correlation function in the presence of the modulator is related to that in the absence of the modulator by

$$G_m^{(2)}(\tau) = |m(\tau)|^2 G^{(2)}(\tau) \tag{5.1}$$

With the biphoton wavefunction given by $\Psi(t_1, t_1 + \tau)$ the modulated (conditional) single photon wavefunction is $m(\tau)\Psi(t_1, t_1 + \tau)$. We adjust the bias voltage at the input of modulator so that the output of the modulator $m(\tau)$ is related to the input voltage $V(\tau)$ by $m(\tau) = \sin[\phi(\tau)] \exp[i\alpha\phi(\tau)]$, where $\phi(\tau) = \pi V(\tau)/(2V_\pi)$, and α is a phase modulation parameter. For a z-cut amplitude modulator as used here $\alpha = 0.75$, but may be eliminated by using an x-cut modulator.

The principal experimental results of this work are shown in Figure 10. In part (a), the modulation signal, shown as an inset, is a set of two square pulses. Of importance, there is no vertical scaling between the modulated and non-modulated waveforms. In Fig. 10(b), we show photons modulated with two different waveforms. In the first case the modulator is driven with a gaussian pulse. In the second case we design the function generator output so as to compensate for the nonlinear distortion of the modulator in such a way that the output of the modulator is an exact rising exponential.

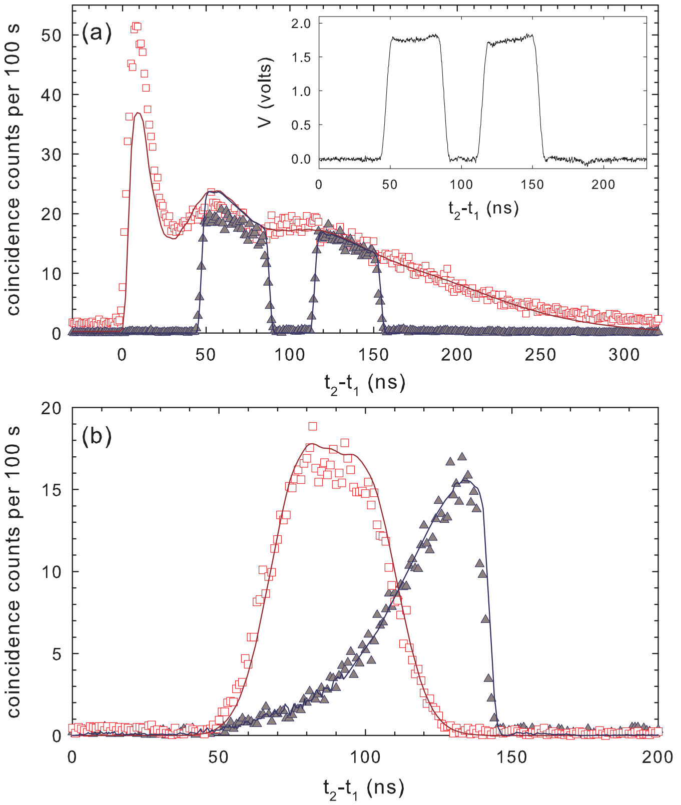

Figure 10: D_1-D_2 coincidence counts in a 1 ns bin as a function of the delay between Stokes and anti-Stokes photons. (a) Modulated (▲) and unmodulated (□) waveforms. (b) Waveforms with Gaussian (□) and rising exponential (▲) shapes. The experimental data (□, ▲) were collected over 2000 s. The solid curves for cases (a) and (b) are plotted from theory. The inset in part (a) is the scope trace of the output voltage of the function generator.

We define the retrieval efficiency, $\mathcal{E}_R$ of a paired photon source as the probability to generate a single anti-Stokes photon on the condition that its paired Stokes photon is detected. For the non-modulated photon we measure $\mathcal{E}_R = 3.5\%$. When losses at the beamsplitter, modulator, filters, fiber to fiber coupling and detector efficiency are backed out, this corresponds to a retrieval efficiency of 55%. For the modulated photons the measured retrieval efficiencies of the two square pulses, the rising exponential and gaussian waveforms are $\mathcal{E}_R = 1.3\%, 0.61\%$ and 0.9% respectively. With losses backed out these efficiencies are $21\%, 9.4\%$ and 11.2% respectively.

Since single photons incident on a beamsplitter must go into one output port or the other, in the ideal case where there are no two-photon events and there is no excess scattered light,

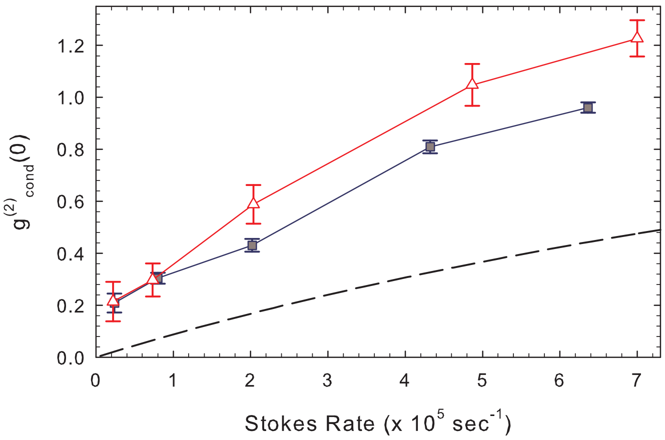

Figure 11: (color online) Conditional three-fold correlation function $g^{(2)}_{cond}(0)$ as a function of the Stokes rate for unmodulated (□) and modulated (△) single-photon generation. The dashed curve shows the theoretical limit for $g^{(2)}_{cond}(0)$ in the absence of excess light scattering (see text).

we would expect no three-fold coincidences at the detectors. A measure of the quality of heralded single photons that quantifies suppression of two photon events is given by the conditional correlation function:

$$g^{(2)}_{cond}(0) = \frac{N_{123}N_1}{N_{12}N_{13}}. \tag{5.2}$$

Here N_1 is the number of the Stokes counts at D_1, N_{12}, and N_{13} are the number of two-fold coincidence counts within a time window T_c at detectors D_1, D_2 and D_1, D_3; and N_{123} is the number of three-fold coincidence counts within this same time window.

In Figure 11 triangles and squares show measured $g^{(2)}_{cond}(0)$ versus Stokes rate with and without modulation. The modulation is done with the same signal as in Fig. 10(a). We set T_c equal to the nominal length of the unmodulated biphoton (285 ns). At a Stokes rate of 2.2×10^4 sec^{-1} which corresponds to $\Omega_p = 0.26\ \Gamma_3$, we obtain $g^{(2)}_{cond}(0) = 0.2 \pm 0.04$ and $g^{(2)}_{cond}(0) = 0.21 \pm 0.07$ for the unmodulated and modulated waveforms respectively. The fact that the measured $g^{(2)}_{cond}(0)$ is less than 0.5, (the limiting value for a two photon Fock state), is indicative of the near-single photon character of the light source.

Because there is a small probability for the parametric down conversion process to generate multiple pairs of biphotons, even in the absence of spurious light scattering, the conditional correlation function is not zero. The dashed curve In Fig. 11 shows the theoretical prediction for the conditional correlation function that results from such multiple scattering events. Because of light scattering from both the pump and coupling lasers, the experimental curves lie above this limiting value.

We perform two control experiments: In the first we remove the 30 m long optical fiber so as to modulate the uncorrelated background noise in the tail of the correlation function. Here, we measure $g^{(2)}_{cond}(0) = 1.2$. In the second experiment we apply modulation at random times, using an external 10 MHz digital signal as a trigger for the function generator. As expected, we observe a reduced rate of paired counts and no change in the shape of the correlation function.

The method demonstrated in this work might be used to optimally load a single photon into an optical cavity, or instead, to study the transient response of atoms to different single photon waveforms. In the context of light-matter interfaces, it may improve the efficiency of storage and retrieval of single photons in atomic ensembles. For quantum information applications, both amplitude and phase modulators could be used to allow full control over the single photon waveforms. For example, one could a construct a single photon waveform that is a train of identical pulses with information encoded into the relative phase difference between consecutive pulses. The importance of the electro-optic method is its speed and ability to modulate phase as well as amplitude. The technique provides the technology for studying the response of atoms to shaped single photon waveforms on a time-scale comparable to the natural linewidth.

For more details please see: P. Kolchin, Chinmay Belthangady, Shengwang Du, G.Y. Yin, and S.E. Harris, "Electro-Optic Modulation of Single Photons," *Phys. Rev. Lett.* **101**, 103601 (September, 2008).

6 Modulation and Measurement of Time-Energy Entangled Photons

In this section of the final report, we extend our work on the modulation of single photons to the modulation of biphotons. The essential difference is that we no longer measure and set the timing by the measurement of a single photon. Instead, biphoton pairs arrive at random at their respective detectors. A highlight of this work is the invention and first experimental demonstration of a Fourier technique that allows the measurement of fast biphotons using slow detectors. Figure 12 shows (a) the schematic of our proof-of-principal experiment and (b) the laser/rubidium-atom interaction diagram for paired photon generation. Parametrically down-converted spontaneous signal and idler photons, or as in the experiment of this work, Stokes and anti-Stokes photons, are incident on synchronously driven sinusoidal amplitude modulators. Without any modulation, in general, the setup will directly yield the Glauber correlation function $G^{(2)}(\tau)$, where τ is the relative arrival time of the signal and idler photons, with its time resolution limited by the speed of photon detector (SPCM) and TDC system. As shown below, our new method, by adding AM photon modulation, will give temporal biphoton correlation measurement with time resolution beyond the SPCM-TDC limit.

When amplitude modulators $m_1(t)$ and $m_2(t)$ are introduced between the down conversion source and the detectors, the modulated correlation function is then written as

$$G_M^{(2)}(t, t+\tau) = |m_1(t)|^2 \, |m_2(t+\tau)|^2 \, G_0^{(2)}(\tau) \tag{6.1}$$

where the subscripts M and 0 indicate cases of modulation on or off. In real experiments, photons arrive at a random time t which is averaged out over the data collection period T:

$$\begin{aligned} &\overline{G_M^{(2)}(\tau)} = \mathcal{M}(\tau) G_0^{(2)}(\tau), \\ &\mathcal{M}(\tau) = \frac{1}{T} \int_0^T |m_1(t)|^2 \, |m_2(t+\tau)|^2 \, dt, \end{aligned} \tag{6.2}$$

where $\mathcal{M}(\tau)$ is the intensity correlation function of the modulators in the signal and idler channels. If both channels are modulated by sinusoidal amplitude modulators with frequency ω and a common phase φ, that is by modulators $m_1(t) = m_2(t) = \cos(\omega t + \varphi)$, then, irrespective of this phase, $\mathcal{M}(\tau) = 1/4 + 1/8\cos(2\omega\tau)$.

If the detectors are slow in the sense that they integrate over the length of the biphoton wave packet , but short as compared to the inverse rate of biphoton generation, the measurement becomes an integral

$$\int_0^\infty \overline{G_M^{(2)}(\tau,\omega)}d\tau = 1/8\int_0^\infty \left[2+\cos(2\omega\tau)\right] G_0^{(2)}(\tau)d\tau. \tag{6.3}$$

We neglect the DC term and normalize to obtain the Fourier cosine transform pair

$$\begin{aligned} F(2\omega) &= \sqrt{\frac{2}{\pi}}\int_0^\infty G_0^{(2)}(\tau)\cos(2\omega\tau)d\tau, \\ G_0^{(2)}(\tau) &= \sqrt{\frac{2}{\pi}}\int_0^\infty F(2\omega)\cos(2\omega\tau)d\omega. \end{aligned} \tag{6.4}$$

In the measurement procedure, $F(2\omega)$ is the measured coincidence count rate between low speed single photon counting modules (SPCMs) as a function of the sinusoidal modulation frequency ω. The slow detection system (SPCM+TDC) means that hardware integrates signals over τ, which is the relative arrival time of the signal and idler photons. We then apply the above inverse Fourier cosine transform to yield the Glauber correlation function $G_0^{(2)}(\tau)$ and therefore the square of the absolute value of the biphoton wavefunction.

Our experiment makes use of long biphotons that are produced using the techniques of electromagnetically induced transparency and slow light. The use of long biphotons allows us to compare the correlation function measured by our Fourier transform technique with a direct measurement using fast detectors and a TDC. The experimental configuration is shown in Fig. 12(a). Paired photons are generated with cold Rb atoms using the method of Balic et al. We apply strong counterpropagating pump and coupling lasers (not shown) to produce phase matched counter-propagating pairs of time-energy entangled Stokes and anti-Stokes photons. We use a ^{85}Rb two-dimensional magneto-optic trap with an optical depth which can be varied between 10 to 60 to generate biphotons with temporal lengths between 50 and 900 ns. The inset in Fig. 13(a) shows the biphoton wavefunction obtained at an optical depth of 35 as directly measured using a TDC. Two features are of interest. First,

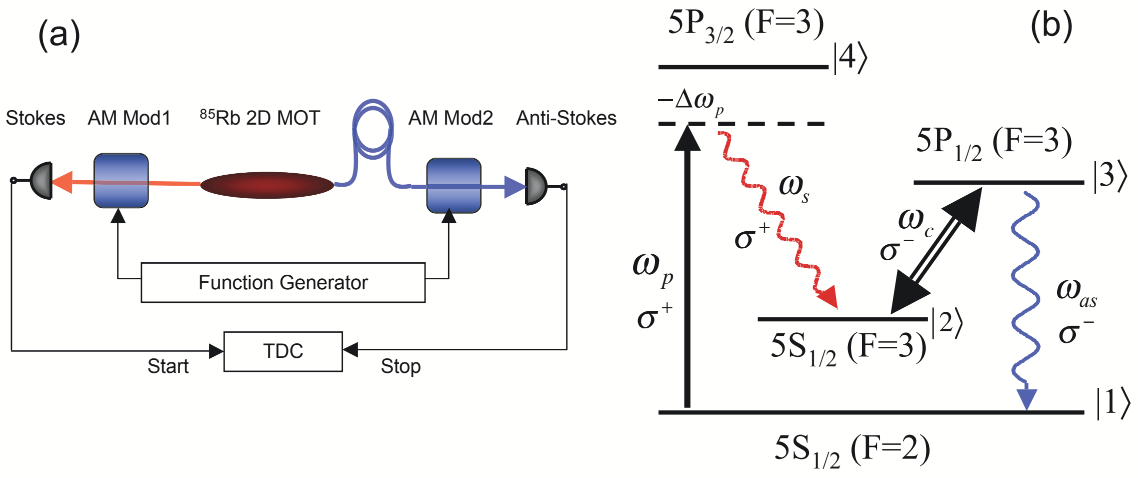
(a)
Stokes
AM Mod1
^{85}Rb 2D MOT
AM Mod2
Anti-Stokes
Function Generator
TDC
Start
Stop
(b)
$5P_{3/2}$ (F=3)
$|4\rangle$
$-\Delta\omega_p$
ω_s
σ^+
$5P_{1/2}$ (F=3)
$|3\rangle$
ω_c
σ^-
ω_p
σ^+
ω_{as}
σ^-
$|2\rangle$
$5S_{1/2}$ (F=3)
$|1\rangle$
$5S_{1/2}$ (F=2)

Figure 12: (a) Schematic of experiment. Long biphotons are generated in the cold-atom Rb cell. Using an optical fiber, the anti-Stokes photon is delayed by 175 ns, and the photons are modulated by synchronously-driven sinusoidal modulators before correlation detection with a time-to-digital converter. (b) Energy level diagram for paired photon generation in Rb.

the width of the wavefunction is determined by the slow group velocity of the anti-Stokes photon and varies linearly with the optical depth. Second, the distinctive sharp feature at the leading edge is a Sommerfield-Brillouin precursor that ensures that the earliest signal reaches a detector at the speed of light in vacuum.

The generated Stokes and anti-Stokes photons are transmitted through 10 GHz electro-optic amplitude modulators (Eospace Inc.) with a half-wave voltage, V_π of 1.3V. To obtain a perfectly sinusoidal output, the modulators are biased at maximum transmission and the input voltage is varied linearly using a triangular waveform that varies between $-V_\pi$ and $+V_\pi$. This waveform is generated by a fast function generator (Tektronics AFG3252) with two output channels whose frequencies and phases can be varied independently. The modulated photons are then sent to SPCMs (Perkin Elmer SPCM-AQR-13), which are connected to the start and stop inputs of a TDC (Fast-Comtec TDC 7886S). Coincidence counts are binned into histograms and plotted as a function of the time difference between the detection of a Stokes and an anti-Stokes photon.

In Fig. 13 (color online) we demonstrate the modulation of a biphoton wavefunction. The data are recoded by binning coincidence counts versus time into 1 ns bins. In Fig. 13(a), the

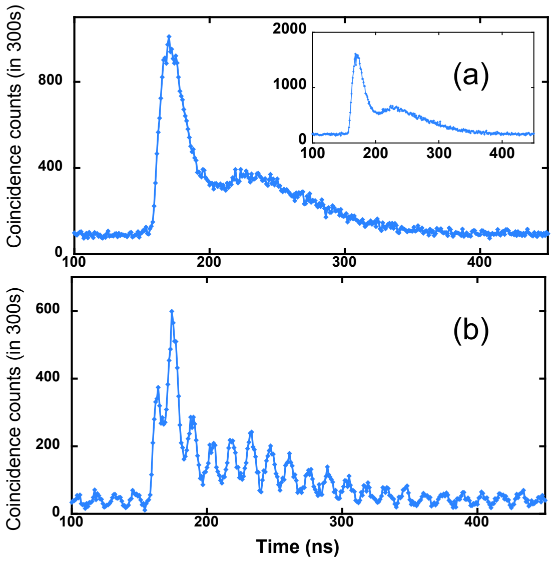

Figure 13: (color online) Modulation of the biphoton correlation function. (a) $m_1(t) = 1$ and $m_2(t) = \cos(\omega t + \varphi)$. The inset in (a) shows the correlation function with both modulators open. (b) $m_1(t) = m_2(t) = \cos(\omega t + \varphi)$. Here $\omega = 2\pi\times$ 35 $\times 10^6$.

Stokes modulator is turned off and is biased at maximum transmission; and the anti-Stokes modulator is driven at 35 MHz. In agreement with theory, the biphoton wavefunction is not modulated. In Fig. 13(b), both modulators are modulated at 35 MHz with the same, but arbitrary, phase. The correlation function is now modulated at twice the applied frequency, i.e. at 70 MHz. When driven by non-sinusoidal waveforms, the correlation function is modulated by the cross-correlation of the two modulating signals. In agreement with Eq. (6.2), we have verified that when the two modulating signals are square waves with the same frequency, the correlation function is modulated by a triangular function.

We next demonstrate the Fourier measurement technique. A 35 m long polarization-maintaining fiber is used to delay the anti-Stokes photon by 175 ns in the experiment. The modulators are driven synchronously at frequencies between 0 and 30 MHz. To simulate slow detectors, we bin coincidences into 1 μs bins, and since the temporal extent of the waveform is less than 1 μs, the entire biphoton is contained within the first time bin. From the Fourier transform property that delay in the time domain corresponds to oscillation in the frequency domain, the plot of coincidence counts versus modulation frequency shows ripples with a frequency (5.7 MHz) equal to the inverse of the time delay. We show two

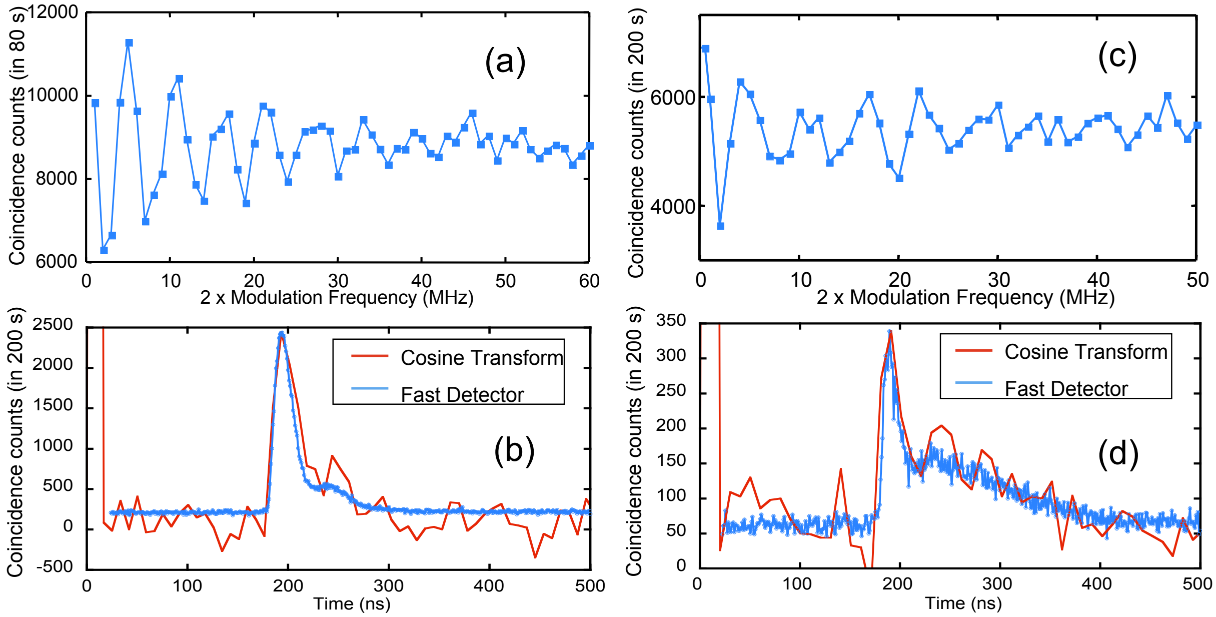

Figure 14: Fourier Transform measurement technique at an optical depth of 15(Left) and 35(Right). **Upper:** Frequency domain data, **Lower:** Fourier Cosine transforms (red) of corresponding frequency domain data, and real-time fast direct temporal correlation data (blue). The term modulation frequency on the x-axis of (a) and (c) refers to the applied frequency. The observed modulation frequency [Eq. (6.4)] is a factor of 2 higher.

data sets in Fig. 14 for optical depth of 15 (left) and 35 (right), for relatively short and long biphoton wave packets, respectively. In Figs. 14(b) and (d), we compare the biphoton wavefunction as directly measured with 1 ns bins (blue line) to the Fourier cosine transform of the traces in Figs. 14(a) and (c), (red line), vertically scaled to match the peak value. We find reasonable agreement between the two methods. We note that the sharp spike in the temporal trace near $t = 0$ results from the DC component in the frequency domain trace.

We have shown how biphotons may be modulated, and how this modulation may be used to measure the magnitude of the biphoton wavefunction. Though we have used long biphotons and low modulation frequencies, we believe that this technique should be extendable to short biphotons. A commercially available telecommunication modulator driven at a frequency of 60 GHz and therefore modulating at 120 GHz will allow measurement of biphotons with a minimum length of about 8 picoseconds. This is about a factor of five faster than state-of-the-art commercial SPCMs. If the comparison is made on the basis of state-of-the-art polymer light modulators operating at 200 GHz and therefore modulating at 400 GHz, then the Fourier technique, will allow measurement down to about 2.5 ps. This is about eight times faster than the fastest reported superconducting detector. Looking further to the future, all-optical light modulators have been demonstrated at frequencies greater than 1 THz; thereby in principle allowing measurement of photons on femtosecond time scales. We note that an advantage of the Fourier technique as compared to either sum frequency correlation or Hong-Ou-Mandel interference is that the signal and idler photons may be correlated at distant detectors and do not need to be brought together at a summing crystal or at a beam splitter.

For more details please see: Chinmay Belthangady, Shengwang Du, Chih-Sung Chuu, G.Y. Yin, and S.E. Harris, “Modulation and measurement of time-energy entangled photons”, *Phys. Rev. A*, Rapid Communications, **80**, 031803 (September 2009).

7 Observation of Nonlocal Modulation with Entangled Photons

The idea of what we term here as nonlocal modulation was published about two years ago; i.e., S. E. Harris, “Nonlocal Modulation of Entangled Photons,” *Phys. Rev.* A **78**, 021807(R) (2008). This section of the report describes the first experimental observation of this effect.

When the photons of a time-energy entangled pair are sent through different channels having arbitrary dispersions, the dispersion in one channel may be negated by dispersion of the opposite sign in the other channel. This effect results from a quantum mechanical interference and has no classical analog. This is now termed as nonlocal dispersion compensation. We report the first observation of a time-frequency analog to nonlocal dispersion cancellation and term this effect as nonlocal modulation. Consider a simplified concept system as shown in left portion of Fig. 15, where a monochromatic pump generates non-degenerate time-energy entangled photon pairs. The signal and idler photons (Channels 1 and 2) pass through sinusoidal phase modulators. These modulators are driven at the same modulation frequency, and their relative phase may be varied. After passing through the modulators, the signal and idler photons are dispersed, for example, by a prism, and the relative positions (frequencies) of the signal and idler photons are correlated. When the modulation frequency is small as compared to the spectral bandwidth of the signal or idler, we find a consequence of time-energy entanglement that we term as nonlocal modulation. Specifically, these distant modulators act cumulatively to determine the apparent modulation depth. If the two identical modulators have opposite phase, they negate each other and act as if neither modulator were present. Conversely, if operated with the same phase, they produce the same correlation as does a single modulator with twice the modulation depth acting on only one of the photons.

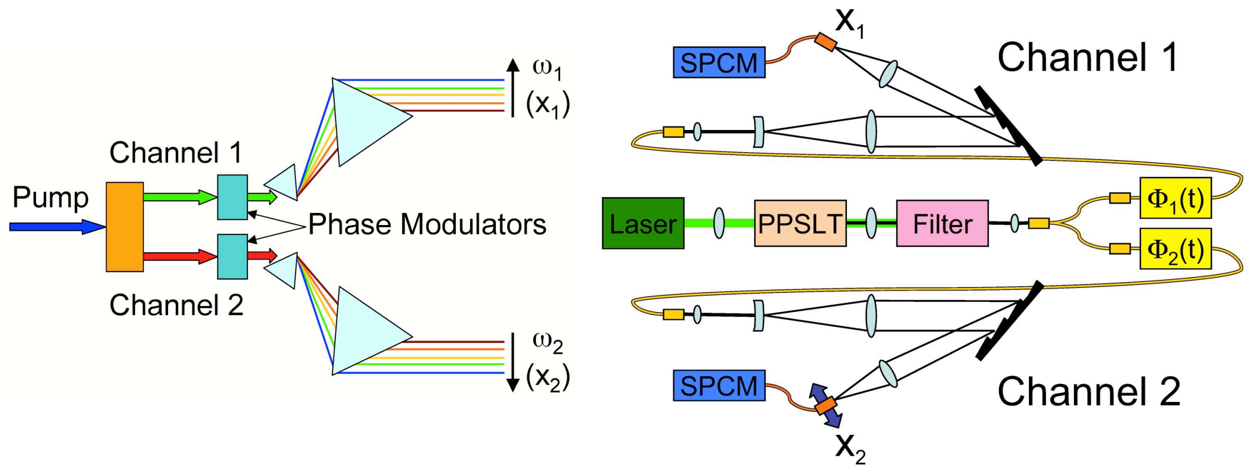

Figure 15: Nonlocal modulation. Signal and idler photons are phase modulated at the same frequency and with controllable phase. The signal and idler beams are frequency-dispersed, and the positions (frequencies) of the detected photons on the photodetectors are correlated. **Left:** simplified concept diagram. **Right:** experimental configuration.

If the resolution of the frequency correlator of Fig. 15 (left) is infinite, the resulting correlation traces for phased and anti-phased modulators may look something like Fig. 16. Since the pump laser which generates the entangled photons is monochromatic, they are delta-function correlated in frequency before any modulation occurs. The modulators act

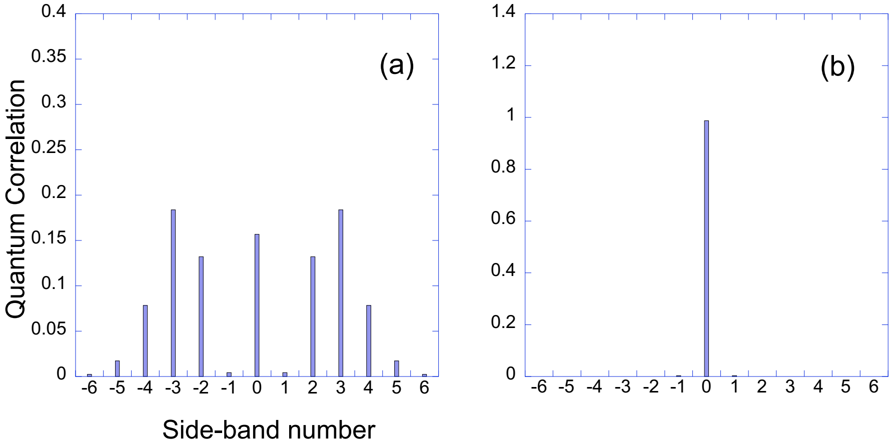

Figure 16: Example frequency correlation function with (a) phased and (b) anti-phased sinusoidal modulators. Because the modulators have the same amplitude, cumulative modulation results in either (a) doubling of modulation depth or (b) cancellation of modulation in the spectral correlation.

on this delta function correlation by generating sidebands whose distribution depends on the amplitude of the sinusoidal driving signal. If the modulators are run in phase with each other, the distribution of sidebands resembles that of a single modulator with twice the driving amplitude [Fig. 16(a)]. If run with opposite phase, the modulators cancel each other, and a single delta function is present in the correlation, as if neither modulator were present [Fig. 16(b)].

The more detailed experimental configuration is shown in right part of Fig. 15. We pump a 20 mm long, periodically-poled, magnesium oxide-doped stoichiometric lithium tantalate crystal (PPSLT) with 0.8 W from a 532 nm cw laser. The nonlinear crystal is phase matched to produce 32 nm bandwidth, degenerate photon pairs at 1064 nm. All fields are polarized along the extraordinary axis of the crystal. The generated photons are filtered from the strong 532 nm pumping beam using a four-prism setup and are then coupled into a polarization-maintaining fused-fiber beam splitter (AFW PFC-64-1-50-L-P-7-1-F) which diverts the photons into Channels 1 and 2 with equal probability. The photons are passed through identical sinusoidal phase modulators (EOSPACE) which are driven at 30 GHz with modulation depths of about 1.5 radians. To set the modulation depth, we adjust the variable attenuators in the microwave driver circuit and verify the depth by measuring the sideband amplitudes of a 1064 nm Nd:YAG reference laser. The relative phase between the modulators is controlled using a calibrated phase trimmer. The microwave circuit schematic is detailed in Fig. 17.

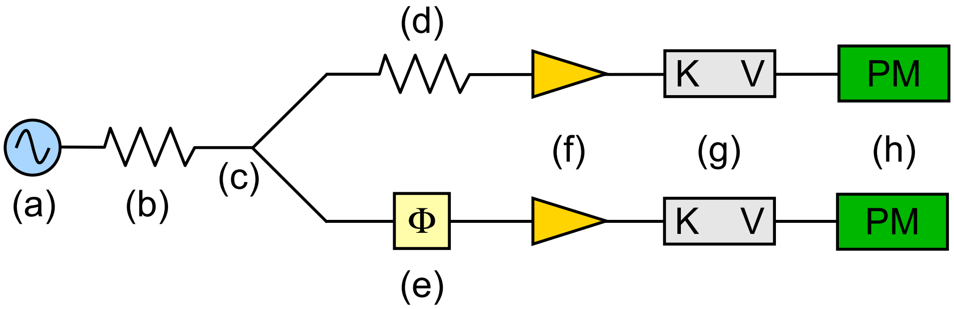

Figure 17: Driver circuit for 30 GHz phase modulators: (a) Microwave Dynamics PLO-3072 30 GHz source, (b) Weinschel Associates 953K-3dB variable attenuator, (c) Picosecond Pulse Labs 5350-218 power divider, (d) Weinschel Associates 953K-10dB variable attenuator, (e) Atm Inc. P1409-360 phase trimmer, (f) Nextec-RF NA00435 amplifiers, (g) MegaPhase CA-V1K2 K to V coaxial adapters, (h) EOSPACE PM-DV5-40-PFU-PFU-106-LV-UL custom phase modulators.

The photons then pass through identical monochromators, each having a linear dispersion of 210 GHz/mm and a Gaussian instrument response function with a FWHM of 8.5 GHz. The monochromators each consist of a 1200 grooves/mm, aluminum-coated grating (Thorlabs GR50-1210) operating at a deviation angle of about 8 degrees. Lenses with focal lengths of -12.75 and 250 mm are used, in a telescope arrangement, to magnify the beam before diffraction by the grating. A 750 mm lens focuses the diffracted beam through a 50 μm slit. To obtain frequency domain correlation curves, we fix the output slit in Channel 1 at x_1 and scan the position x_2 in Channel 2. The photons that are transmitted through the monochromator slits are coupled into multimode fibers and detected with time-resolved single photon counting modules (SPCMs, id Quantique id400 and PerkinElmer SPCM-AQR-16-FC). A photograph of the monochromators is shown in Fig. 18.

The primary experimental results of this work are shown in Fig. 19. For each case, we set the monochromator slit in Channel 1 at an arbitrary position x_1 that is near the center of the generated 32 nm spectrum and leave the position of this slit fixed thereafter. The slit in Channel 2 is scanned over positions x_2, and the coincidence rate of the two detectors (with

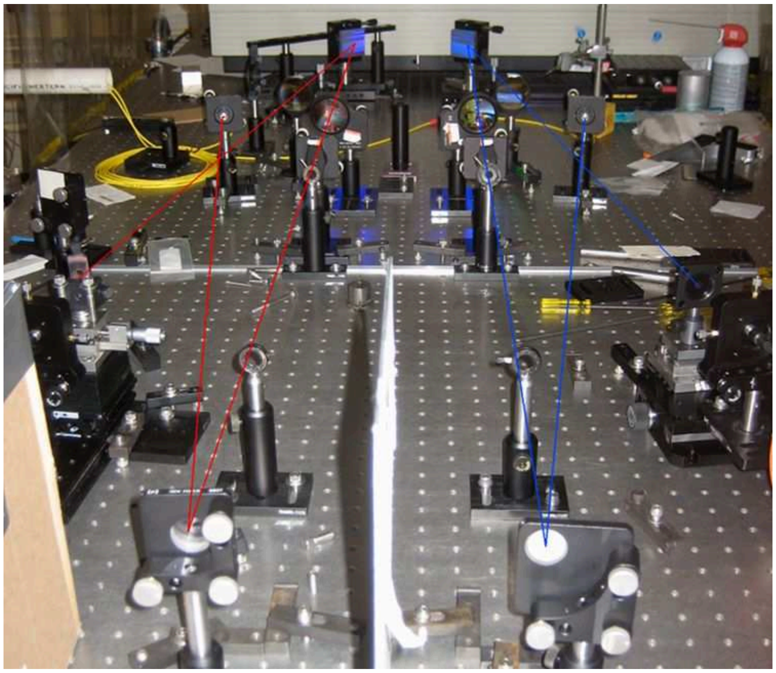

Figure 18: Photo of frequency correlation setup. Identical monochromators measure the frequencies of the entangled photons. Red and blue lines show the beam path for Channel 1 and Channel 2, respectively.

gate width $T = 1.25$ ns) is recorded as a function of this position. For each position, the rate is averaged for 20 s.

With the pump frequency defined as ω_p, and the position x_2 proportional to the frequency ω_2, we express the coincidence rate as a function of relative frequency $\Delta \equiv \omega_2 - (\omega_p - \omega_1)$. The scale of the frequency axis is calibrated by measuring the sideband spacing of a single-mode 1064 nm laser modulated at 30 GHz, with the zero position chosen (at the start of the experiment) as the location of the correlation peak for unmodulated photon pairs.

The upper portion of Fig. 19 shows the experimental results without modulation and with modulation in a single channel. In Fig. 19(a) (upper), both modulators are turned off by disconnecting their 30 GHz drive signals. As expected by energy conservation, a single correlation peak is observed. In Fig. 19(b) (upper), Channel 1 is phase modulated as $\exp[i\delta \sin(\omega_m t)]$ with a modulation depth of $\delta = 1.5$, and Channel 2 is not modulated. The frequency correlation is now distributed over a set of sidebands, having Bessel function amplitudes $J_n^2(\delta)$, whose total area is equal to that of upper (a) of Fig. 19.

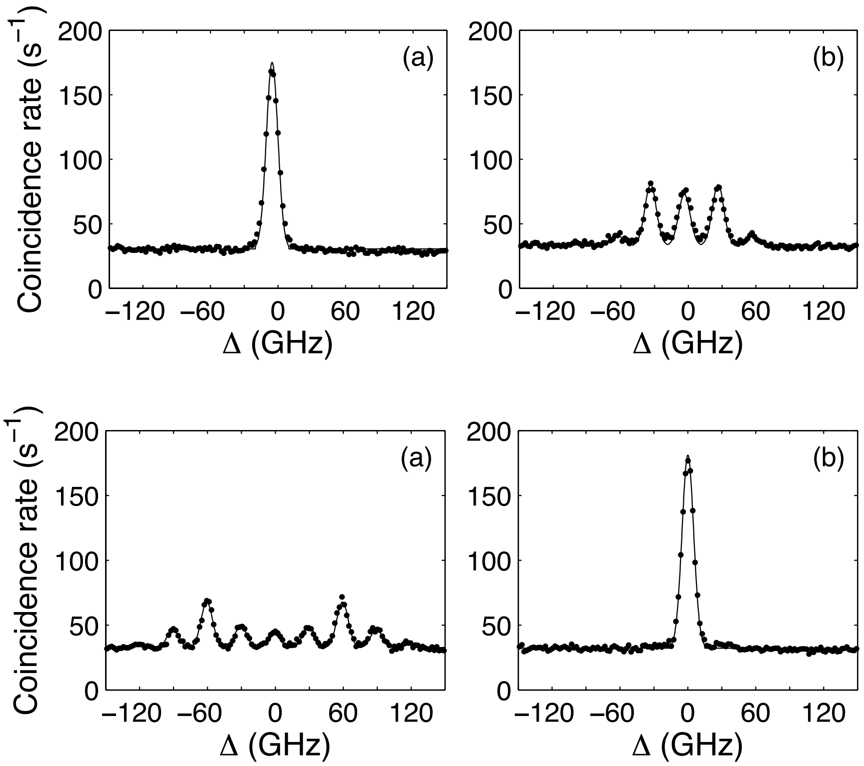

Figure 19: Frequency correlation measurements. The horizontal axes measure relative frequency changes as slit position x_2 is scanned. **Upper:** (a) both modulators turned off and (b) the modulator in Channel 1 running at a modulation depth of 1.5. **Lower:** both modulators running (a) with the same phase and (b) with opposite phase. The modulation depth for both modulators is 1.5. Circles are data; curves are theoretical fits (see text).

In Fig. 19(a) (lower), both modulators are turned on at a modulation depth of $\delta = 1.5$, and the cable length is adjusted so that they have the same phase. They now act cumulatively (constructively interfere) to produce a set of sidebands having a Bessel function distribution $J_n^2(2\delta)$. The frequency-domain correlation function of two distant modulators is therefore the same as that which would be obtained by correlating an unmodulated photon with a photon modulated at twice the modulation depth.

In Fig. 19(b) (lower), the modulators are run at the same depth as in the previous paragraph, but now the relative cable length is adjusted so that the modulators are run in phase opposition. The modulators now destructively interfere, and no sidebands are visible.

The striking difference between Figs. 16 and 19 is that the sidebands are not delta functions but have widths determined by the resolution of the frequency correlator in Fig. 15

(right). We have developed a theory to predict the measured correlation functions with finite-resolution monochromators as used in our experiment. The following describes this theory, which is used to produce the solid curves in Fig. 19.

Working in the Heisenberg picture, a nonlinear crystal of length L is pumped by a monochromatic laser at frequency ω_p. A positive-frequency field operator $a(\omega, z)$, representing entangled photons, evolves inside the crystal and may be written in terms of an envelope $b(\omega, z)$ which varies slowly along the propagation direction: $a(\omega, z) = b(\omega, z)\exp[ik(\omega)z]$. The propagation equations describing entangled photon generation are

$$\begin{aligned} \frac{\partial b(\omega, z)}{\partial z} &= i\kappa(\omega)b^\dagger(\omega_p - \omega, z)\exp[i\Delta k(\omega)z], \\ \frac{\partial b^\dagger(\omega, z)}{\partial z} &= -i\kappa^*(\omega)b(\omega_p - \omega, z)\exp[-i\Delta k(\omega)z]. \end{aligned} \tag{7.1}$$

where $\kappa(\omega)$ and $\Delta k(\omega)$ are the coupling factor and wave-vector mismatch, respectively. The solution for the output field at $z = L$, expressed in terms of the vacuum field $a_{\text{vac}}(\omega)$ at the input of the crystal, is

$$a_{\text{out}}(\omega) = A(\omega)a_{\text{vac}}(\omega) + B(\omega)a^\dagger_{\text{vac}}(\omega_p - \omega), \tag{7.2}$$

where, to preserve the commutation relations, the functions $A(\omega)$ and $B(\omega)$ satisfy $|A(\omega)|^2 - |B(\omega)|^2 = 1$ and $A(\omega)B(\omega_p - \omega) = B(\omega)A(\omega_p - \omega)$.

The time-domain output field operator is related to its frequency-domain counterpart [Eq. (7.2)] by the inverse Fourier transform, $a_{\text{out}}(t) = \int_{-\infty}^{\infty} a_{\text{out}}(\omega)\exp(-i\omega t)d\omega$, and is normalized so that the total rate of generated photons exiting the crystal is $R_{\text{out}} = \langle a^\dagger_{\text{out}}(t)a_{\text{out}}(t)\rangle$. The generated photons are separated into two channels, denoted as Channel 1 and Channel 2, using a 50/50 beam splitter. The field operators at the outputs of the beam splitter are $a_1(t) = a_2(t) = \frac{1}{\sqrt{2}}a_{\text{out}}(t)$. The photons are modulated by periodic phase modulators whose time-domain, Fourier-series transfer functions are $m_1(t) = \sum_k q_k \exp(-ik\omega_m t)$ in Channel 1 and $m_2(t) = \sum_l r_l \exp(-il\omega_m t)$ in Channel 2, with Fourier transforms $m_1(\omega) = \sum_k q_k\delta(\omega - k\omega_m)$ and $m_2(\omega) = \sum_l r_l\delta(\omega - l\omega_m)$, respectively. With the $*$ symbol denoting convolution, the frequency-domain modulated fields are $\tilde{a}_1(\omega) = a_1(\omega) * m_1(\omega)$ and

$\tilde{a}_2(\omega) = a_2(\omega) * m_2(\omega)$. Substituting $a_1(\omega)$, $a_2(\omega)$, $m_1(\omega)$, and $m_2(\omega)$ into the expressions for $\tilde{a}_1(\omega)$ and $\tilde{a}_2(\omega)$ yields

$$\begin{aligned}
\tilde{a}_1(\omega) &= \frac{1}{\sqrt{2}} \sum_{k=-\infty}^{\infty} q_k \big[A(\omega - k\omega_m) a_{\text{vac}}(\omega - k\omega_m) \\
&\quad + B(\omega - k\omega_m) a^{\dagger}_{\text{vac}}(\omega_p - \omega + k\omega_m) \big], \\
\tilde{a}_2(\omega) &= \frac{1}{\sqrt{2}} \sum_{l=-\infty}^{\infty} r_l \big[A(\omega - l\omega_m) a_{\text{vac}}(\omega - l\omega_m) \\
&\quad + B(\omega - l\omega_m) a^{\dagger}_{\text{vac}}(\omega_p - \omega + l\omega_m) \big].
\end{aligned} \tag{7.3}$$

The modulated photons are frequency correlated by passing each through identical monochromators whose output slits may be translated to select frequencies $\omega_1 = \beta x_1$ in Channel 1 and $\omega_2 = \beta x_2$ in Channel 2, where the constant β is the linear dispersion of the grating systems. The monochromators (spectral filters) have field transmission functions $H_1(\omega - \beta x_1)$ and $H_2(\omega - \beta x_2)$. The filtered field operators in Channels 1 and 2 are $\tilde{a}_{1\text{f}}(\omega, x_1) = \tilde{a}_1(\omega) H_1(\omega - \beta x_1)$ and $\tilde{a}_{2\text{f}}(\omega, x_2) = \tilde{a}_2(\omega) H_2(\omega - \beta x_2)$, respectively. The count rates at the outputs of the monochromators are given by $R_1(x_1) = \langle \tilde{a}^{\dagger}_{1\text{f}}(t, x_1) \tilde{a}_{1\text{f}}(t, x_1) \rangle$ and $R_2(x_2) = \langle \tilde{a}^{\dagger}_{2\text{f}}(t, x_2) \tilde{a}_{2\text{f}}(t, x_2) \rangle$. These rates are

$$\begin{aligned}
R_1(x_1) &= \frac{1}{4\pi} \sum_{k=-\infty}^{\infty} |q_k|^2 \int_0^{\infty} |B(\omega - k\omega_m)|^2 \, |H_1(\omega - \beta x_1)|^2 d\omega, \\
R_2(x_2) &= \frac{1}{4\pi} \sum_{l=-\infty}^{\infty} |r_l|^2 \int_0^{\infty} |B(\omega - l\omega_m)|^2 \, |H_2(\omega - \beta x_2)|^2 d\omega.
\end{aligned} \tag{7.4}$$

Assuming a gate width T, the coincidence rate for the two detectors is related to the second-order Glauber correlation function $G^{(2)}(t_1, x_1, t_2, x_2) = \langle \tilde{a}^{\dagger}_{2\text{f}}(t_2, x_2) \tilde{a}^{\dagger}_{1\text{f}}(t_1, x_1) \tilde{a}_{1\text{f}}(t_1, x_1) \tilde{a}_{2\text{f}}(t_2, x_2) \rangle$. With the assumption that the resolution of the monochromators is high, or equivalently that the filter widths are small (as compared to the modulation frequency ω_m), it can be shown that the correlation function depends only on the difference of the arrival times $\tau = t_2 - t_1$, and the coincidence rate is

$$R_c(x_1, x_2) = \int_{-T/2}^{T/2} G^{(2)}(\tau, x_1, x_2) d\tau. \tag{7.5}$$

Equation (7.5) may be expanded using Wick's theorem and shown to be given by

$$R_c(x_1, x_2) \;=\; R_1(x_1)R_2(x_2)T + \int_{-\infty}^{\infty} \left| \sum_{k=-\infty}^{\infty} q_k r_{n-k} F_k(\tau, x_1, x_2) \right|^2 d\tau, \tag{7.6}$$

where $\Delta = \beta(x_1 + x_2) - \omega_p$, $n = \lfloor \Delta/\omega_m + \frac{1}{2} \rfloor$, and

$$\begin{aligned} F_k(\tau, x_1, x_2) \;=\; & \frac{1}{4\pi} \int_0^{\infty} A(\omega - k\omega_m) B(\omega_p - \omega + k\omega_m) \\ & \times H_1(\omega - \beta x_1) H_2(\omega_p - \omega - \beta x_2 + n\omega_m) \exp(i\omega\tau) d\omega. \end{aligned} \tag{7.7}$$

The first term in Eq. (7.6) is the result of accidental coincidences between unpaired photons in a gate width T. The second term is the coincidence rate between paired photons and captures the modulation effects described in this section. To obtain Eqs. (7.4)–(7.7), we have assumed that the transmission widths of the monochromators are small as compared to the modulation frequency and large as compared to the inverse of the temporal gate width T. In our experiment these assumptions are satisfied by factors of 3.5 and 11, respectively.

If we further assume that $A(\omega)$ and $B(\omega_p - \omega)$ are constant in the vicinity (±150 GHz in Fig. 19) of $\omega = \beta x_1$ and are equal to A_0 and B_0, respectively, then Eq. (7.6) becomes

$$R_c(\Delta) = R_1 R_2 T + c_n H^{(2)}(n\omega_m - \Delta), \tag{7.8}$$

where $H^{(2)}(\omega) = |H_1(\omega)|^2 * |H_2(\omega)|^2$, and

$$R_1 \;=\; \frac{1}{4\pi} |B_0|^2 \int_{-\infty}^{\infty} |H_1(\omega)|^2 d\omega, \tag{7.8a}$$

$$R_2 \;=\; \frac{1}{4\pi} |B_0|^2 \int_{-\infty}^{\infty} |H_2(\omega)|^2 d\omega, \tag{7.8b}$$

$$c_n \;=\; \frac{1}{8\pi} \left| A_0 B_0 \sum_{k=-\infty}^{\infty} q_k r_{n-k} \right|^2. \tag{7.8c}$$

The solid curves in Fig. 19 are theoretical fits to the data using Eq. (7.8) shifted horizontally so as to match center. The Fourier series coefficients for sinusoidal phase modulators are Bessel functions with $q_k = J_k(-\delta_1)$ and $r_l = J_l(-\delta_2)$, where δ_1 and δ_2 are the modulation depths in Channels 1 and 2, respectively ($|\delta_1| = |\delta_2| = 1.5$ in our experiment). We model the monochromator response functions in Channels 1 and 2 as Gaussians with FWHM bandwidths Γ: $H_1(\omega) = \alpha_1 \exp\left[-2\ln(2)\omega^2/\Gamma^2\right]$ and $H_2(\omega) = \alpha_2 \exp\left[-2\ln(2)\omega^2/\Gamma^2\right]$. (The monochromator in Channel 1 is the mirror image of the one in Channel 2 which has a measured FWHM bandwidth of 8.5 GHz.) The transfer functions include fitting parameters α_1 and α_2 used in Fig. 19 to account for transmission losses and the difference in detection efficiencies of the photon counters.

To obtain the constants A_0 and B_0, for each case in Fig. 19, we measure the average value of R_2 and use Eq. (7.8b) to calculate $|B_0|$. We obtain $|A_0|$ from the commutator-preserving condition $|A_0|^2 - |B_0|^2 = 1$. For all curves, the fitting parameters are taken as $\alpha_1^2 = 1.20 \times 10^{-2}$ and $\alpha_2^2 = 5.59 \times 10^{-4}$. These values are in good agreement with loss measurements and estimates of the photon counter detection efficiency, where we note that the id400 detector in Channel 1 has a detection efficiency an order of magnitude larger than the SPCM-AQR-16-FC detector in Channel 2.

The experiment and theory summarized in this section pertain to sinusoidal phase modulation. We have also developed a general theory for nonlocal modulation, presented below.

For general modulation, the modulated signal and idler field operators are described by convolution as before: $\tilde{a}_1(\omega) = a_1(\omega) * m_1(\omega)$ and $\tilde{a}_2(\omega) = a_2(\omega) * m_2(\omega)$; however, the modulation functions $m_1(t)$ and $m_2(t)$ [with Fourier transforms $m_1(\omega)$ and $m_2(\omega)$] are no longer assumed to be periodic. The resulting Glauber correlation function becomes:

$$G^{(2)}(t_1, x_1, t_2, x_2) = \mathcal{C}(t_1, x_1, t_2, x_2) + \mathcal{Q}(t_1, x_1, t_2, x_2), \tag{7.9}$$

where the functions $\mathcal{C}(t_1, x_1, t_2, x_2)$ and $\mathcal{Q}(t_1, x_1, t_2, x_2)$ are

$$\begin{aligned}
\mathcal{C}(t_1,x_1,t_2,x_2) &= \frac{1}{16\pi^2}\int_{-\infty}^{\infty}\int_{-\infty}^{\infty}\int_{-\infty}^{\infty}\int_{-\infty}^{\infty}\int_{-\infty}^{\infty}\int_{-\infty}^{\infty} m_1^*(\Omega_1)m_1(\Omega_3)m_2^*(\Omega_2)m_2(\Omega_4)\\
&\quad\times|B(\omega_1-\Omega_1)|^2|B(\omega_2-\Omega_2)|^2H_1^*(\omega_1-\beta x_1)H_1(\omega_1-\Omega_1+\Omega_3-\beta x_1)\\
&\quad\times H_2^*(\omega_2-\beta x_2)H_2(\omega_2-\Omega_2+\Omega_4-\beta x_2)\\
&\quad\times\exp\{i[(\Omega_2-\Omega_4)t_2+(\Omega_1-\Omega_3)t_1]\}d\omega_1 d\omega_2 d\Omega_1 d\Omega_2 d\Omega_3 d\Omega_4,\\
\mathcal{Q}(t_1,x_1,t_2,x_2) &= \frac{1}{16\pi^2}\Bigg|\int_{-\infty}^{\infty}\int_{-\infty}^{\infty}\int_{-\infty}^{\infty} m_1(\Omega_1)m_2(\Omega_2)A(\omega-\Omega_1)B(\omega_p-\omega+\Omega_1)\\
&\quad\times H_1(\omega-\beta x_1)H_2(\omega_p-\omega+\Omega_1+\Omega_2-\beta x_2)\\
&\quad\times\exp[i(\omega-\Omega_1-\Omega_2)(t_2-t_1)]\exp[-i(\Omega_1+\Omega_2)t_1]d\omega d\Omega_1 d\Omega_2\Bigg|^2. \qquad (7.10)
\end{aligned}$$

In order to observe nonlocal modulation interference, the modulating waveform must vary slowly as compared to the temporal correlation width of the entangled photons (as described by the paper by Harris in 2008). In Eqs. (7.10), the slow modulation condition may be applied by taking $A(\omega)$ and $B(\omega)$ to be constants (representing a transform-limited, infinite-bandwidth biphoton whose temporal correlation is a delta function). We also assume that the frequency correlation measurement has infinite resolution: $H_1(\omega) = H_2(\omega) = \delta(\omega)$. With these assumptions, $\mathcal{C}(t_1,x_1,t_2,x_2)$ becomes a constant, independent of x_1 and x_2 (or, equivalently, Δ); it is a classical background term arising from coincidences between uncorrelated photons from different entangled pairs. $\mathcal{Q}(t_1,x_1,t_2,x_2)$ becomes

$$\begin{aligned}
\mathcal{Q}(t_1,x_1,t_2,x_2) &\propto |(m_1 * m_2)(\Delta)|^2\\
&= |\mathcal{F}\{m_1(t)m_2(t)\}|^2, \qquad (7.11)
\end{aligned}$$

where $(m_1 * m_2)(\omega) = m_1(\omega) * m_2(\omega)$, and $\mathcal{F}\{f(t)\} = \frac{1}{2\pi}\int_{-\infty}^{\infty} f(t)\exp(i\omega t)dt$ is the Fourier transform. If $m_1(t)$ and $m_2(t)$ are phase modulation waveforms, i.e. $m_1(t) = \exp[i\Phi_1(t)]$ and $m_2(t) = \exp[i\Phi_2(t)]$, then the modulators interfere so as to produce a frequency domain correlation proportional to the square of the Fourier transform of $\exp\{i[\Phi_1(t)+\Phi_2(t)]\}$. For this relation to hold, it is required that $\Phi_1(t)$ and $\Phi_2(t)$ both vary slowly as compared to the temporal width of the two-photon wavefunction.

8 Hiding Single Photons with Spread Spectrum Technology

In this section we describe a proof-of-principal experiment demonstrating the use of spread spectrum technology at the single photon level. We show how single photons with a prescribed temporal waveform may be transmitted through a noisy environment that is created by either narrow band thermal photons, or as in this work, an interfering laser beam that has an average power that is about a thousand times larger than the average power of the beam of single photons. We do this by using two synchronously driven electro-optic phase modulators. As shown in Fig.20(a), the modulator at the transmitter, M_1 broadens the spectrum of the incident photon beam from about 1 MHz to about 10 GHz and thereby reduces the spectral power density by a factor of 10^4. The receiver modulator, M_2 is run in anti-phase to the transmitter modulator so as to demodulate the photon beam and reduce its bandwidth to the original 1 MHz, thereby allowing it to be transmitted through a narrow bandpass filter, F_2.

Now suppose that one wishes to transmit the single photon beam through an environment of thermal photons that have a linewidth that is comparable to that of the original photon beam. If this noise, or instead, a narrowband interfering laser beam is injected after the first modulator [Fig.20(a)], it is spectrally broadened by the second modulator and only a fraction of its power is transmitted through the narrow band filter at the receiver. As a result, the signal-to-noise is increased approximately in the ratio of the modulation bandwidth to the bandwidth of the final filter, and in the language of spread spectrum technology the system experiences a "processing gain". In this work we demonstrate a processing gain of a factor of 50.

In this experiment we use narrowband time-energy entangled pairs of photons (biphotons) produced as described earlier. We set the optical depth of the MOT at 30. With $2\gamma_{13}$ equal to the spontaneous decay rate out of state $|3\rangle$, we set the coupling laser Rabi frequency $\Omega_c = 4.01\gamma_{13}$, the pump laser Rabi frequency $\Omega_p = 1.66\gamma_{13}$ and the pump laser detuning, $\Delta\omega_p = 48.67\gamma_{13}$. Under these conditions the source produces narrowband biphotons with an estimated linewidth of 3.5 MHz at a rate of about 11500 pairs/s.

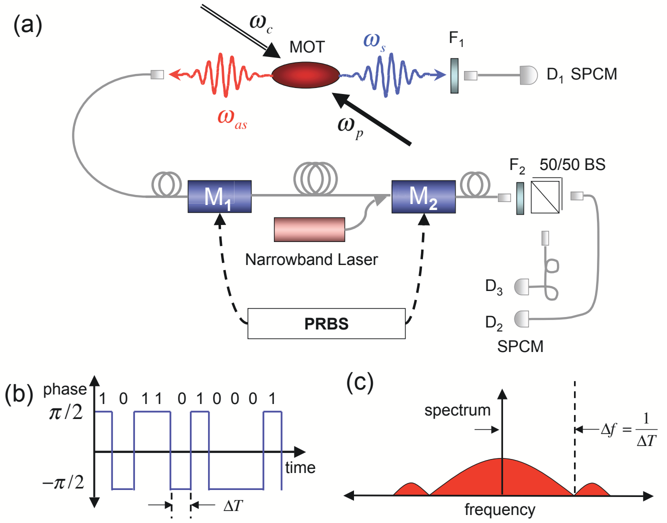

Figure 20: Schematic of paired photon generation and spread spectrum experiment. (a) The spectrum of anti-Stokes photons produced in a magneto-optic trap is spread and narrowed by phase modulators M_1 and M_2 driven by a pseudorandom bit sequence (PRBS) generator. A weak narrowband laser is used to hide the photons. F_1 and F_2 are narrowband filters. A 50/50 beamsplitter (BS) is used to verify the presence of single photons. (b) Pseudorandom phase modulation in the time domain. The labels 1, 0 refer to the outputs of the PRBS generator. (c) Schematic of the optical spectrum after phase modulation by the PRBS generator.

The detection of the Stokes photon by detector D_1 sets the time origin for measurement of the biphoton wavefunction at detector D_2. The anti-Stokes photon is sent through a 20-GHz electro-optic phase modulator (Eospace Inc.) driven by one of two differential data outputs of a pseudorandom bit sequence (PRBS) generator (Centellax TG2P1A) with a bit rate tunable between 0.05-10 Gb/s. In each time slot ΔT, equal to the inverse bit rate, the PRBS outputs a random voltage equal to $V_\pi/2$ (corresponding to logic 1) or $-V_\pi/2$ (logic 0), where V_π is the half-wave voltage of the phase modulators. We choose a bit pattern consisting of 32767 ($2^{15} - 1$) random bits. At a bit rate of 10 Gb/s, the phase therefore switches randomly [Fig.20 (b)] between $-\pi/2$ and $\pi/2$ radians every 0.1 ns. This process of random phase modulation in the time domain spreads the spectrum in the frequency domain from about 3.5 MHz for the unmodulated photon to about 10 GHz for the modulated photon. The envelope of the spread spectrum is a sinc-squared function with the first null, as shown in Fig.20 (c), at a frequency equal to the bit rate.

The phase-modulated anti-Stokes photon is transmitted over a channel consisting of a long single-mode optical fiber [Fig.20(a)]. At the receiver end, the photon is sent through a second phase modulator, identical to the first and driven by the complementary output of the PRBS generator. The two phase modulators are synchronized by adjusting the lengths of the electric cables connecting them to the PRBS generator such that the relative time delay, Δt_{RF} of the radio frequency signal sent to the two modulators equals the travel time, Δt_p, of the anti-Stokes photon between the modulators. Fine adjustment of Δt_{RF} is achieved by means of a radio frequency waveguide of variable length connected to one of the two rf cables. When the phase modulators are run in synchronism such that the phase imposed on the photon by the first modulator is exactly undone by the second modulator, the spectral width of the photon is restored to its original value of 3.5 MHz. When the phase modulators are not run in exact phase opposition, the uncompensated residual phase results in a spectrum that is wider than 3.5 MHz. After passing through the second phase modulator the anti-Stokes photon is sent through a 65-MHz fiber based Fabry-Perot filter (Micron Optics) with a free spectral range of 13.6 GHz. If the spectral width of the photon after the second phase modulator is less than the filter bandwidth, the photon passes through with little loss of probability amplitude. Conversely, if the spectral width of the photon is larger, then it is attenuated by the filter. The spectrum of narrowband noise entering the channel after the first modulator is spread by the second modulator and is attenuated by the filter. To hide the photon we use an attenuated beam from an external-cavity diode laser with a linewidth of about 300 kHz set at the same frequency as the anti-Stokes photon. A 50/50 beamsplitter (BS) and a third detector D_3 is placed after the filter to verify the single photon nature of the experiment.

With both phase modulators and the (noise simulating) laser turned off, the shape of the anti-Stokes photon wavepacket is shown in Fig. 21(a). This shape is measured by recording coincidence counts between detectors D_1 and D_2, with the beamsplitter removed, as a function of the difference in arrival times of the Stokes, t_s, and anti-Stokes, t_{as}, photons at the two detectors. When the first phase modulator is switched on, the spectrum of this photon is spread to about 10 GHz. If the second phase modulator is off, the anti-Stokes

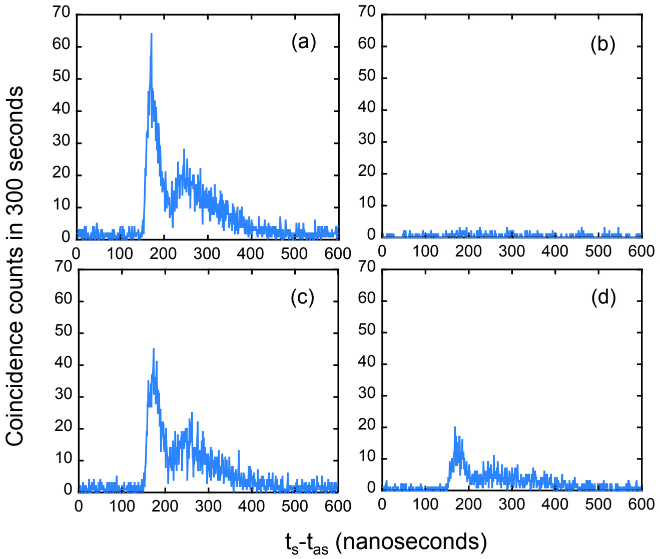

Figure 21: Shape of the anti-Stokes photon wavepacket measured by recording coincidence counts between detectors D_1 and D_2 with the beamsplitter removed. (a) Anti-Stokes photon wavepacket measured when modulators M_1 and M_2 are off. (b)Modulator M_1 is on and modulator M_2 is off. (c) Both modulators are on and run synchronously. (d) Both modulators are on with $\Delta t_{RF} > \Delta t_p$ (see text).

photon is severely attenuated by the narrowband filter F_2 and very little photon probability amplitude leaks through to detector D_2. This is shown in Fig.21 (b). When the second phase modulator is switched on and driven so as to cancel the phase imposed by the first modulator, the photon spectrum is narrowed and passes through filter F_2 with little loss of probability amplitude. This is shown in Fig.21(c). The small residual loss in photon probability amplitude probably arises from a slight mismatch between the two modulators and their complementary driving signals. In Fig.21(d), the difference in lengths of the electric cables connecting the PRBS to the two modulators is chosen such that Δt_{RF} is greater than Δt_p by about 40ps. As a result, the phase imposed on the photon by the first modulator is not exactly negated by the second modulator. Now, after transmission through filter F_2 we observe a reduced, but not zero, coincidence count rate. A similar result is obtained when $\Delta t_{RF} < \Delta t_p$.

We next deliberately inject a weak diode laser beam to hide the the anti-Stokes photon. With additional laser photons at a rate of 40000 s^{-1} and anti-Stokes signal photons at a rate

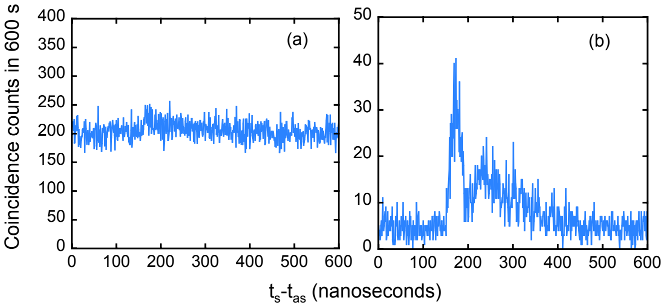

Figure 22: Retrieval of the anti-Stokes photon from injected noise. (a) Anti-Stokes photon wavepacket as hidden by an additional laser beam that is injected into the channel. Here, both modulators are off. (b) Switching on both modulators and running them synchronously recovers the anti-Stokes photon

of 30 s^{-1} [Fig. 22 (a)], anti-Stokes photons can no longer be seen. If the two modulators are now turned on and run in synchronism, the spectrum of the anti-Stokes photon is spread by the first modulator and compressed by the second modulator so that the photon passes through the filter and arrives at the detector with very little attenuation. The spectrum of the laser photons, on the other hand, is spread by the second phase modulator and attenuated by the filter and very little of the laser power reaches the detector. When this is the case, the shape of the anti-Stokes photon wavepacket can be recovered from the noise [Fig.22(b)]. The decrease in the level of the flat uncorrelated background by a factor of about 50 corresponds to the spread spectrum processing gain.

The quality of a single photon source can be quantified by means of the conditional Glauber correlation function, $g^{(2)}_{cond}(0)$ defined in Eq 5.2. We turn off the the weak narrowband laser beam and measure $g^{(2)}_{cond}(0)$ as a function of the rate of detected Stokes photons with both modulators turned off (blue line in Fig. 23) and with both modulators turned on and running synchronously (red line in Fig. 23). At a Stokes rate of approximately $1200 s^{-1}$ we obtain $g^{(2)}_{cond}(0) = 0.22 \pm 0.06$ for the unmodulated photon and $g^{(2)}_{cond}(0) = 0.14 \pm 0.04$ for the phase modulated-demodulated photon. These values of $g^{(2)}_{cond}(0)$ are less than the classical limit of 1 (dashed line in Fig. 23) and reasonably less than the limiting value of 0.5; i.e., the conditional Glauber correlation function for a two-photon Fock state.

We have shown how narrowband single photons may be phase modulated so as to increase the width of their spectrum by several orders of magnitude while at the same time retaining

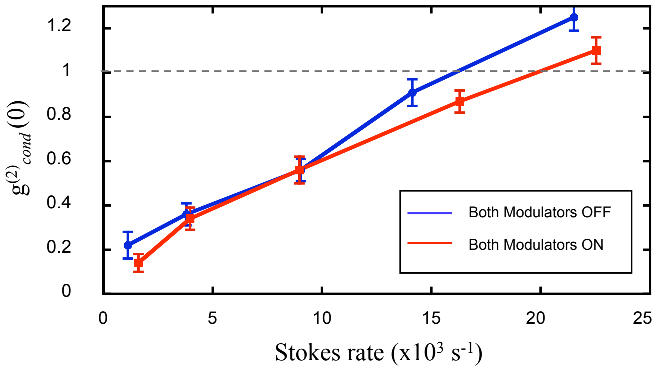

Figure 23: Conditional threefold correlation function as a function of Stokes rate with both modulators off (blue) and with both modulators on (red). The dashed line is the classical limit. The errors are calculated by assuming a Poisson distribution for the coincidence rates.

the information that characterizes their waveform. By compensation with an anti-phased modulator, the biphoton waveform may be reconstructed at a distant location. We have also shown how spread spectrum technology may be used to hide a single photon in the presence of laser photons of the same frequency and similar linewidth. Applications may include an additional level of classical security for quantum key distribution, and someday, multiplexing of single photon communication channels. This work may also be the first use of spread spectrum techniques combined with single photon detection.

9 Joint Support

The work described in this report was jointly supported by the U.S. Air Force Office of Scientific Research, the Defense Advanced Research Projects Agency, and the U.S. Army Research Office. This joint support was essential for all aspects of this project.

APPENDIX:

A DARPA Supported Publications During Grant Period

(1) V. Balic, D. A. Braje, P. Kolchin, G. Y. Yin, and S. E. Harris, “ Generation of Paired Photons with Controlable Waveforms, ” *Phys. Rev. Lett.* **94**, 183601 (May 2005)

(2) P. Kolchin, S. Du, C. Belthangady, G. Y. Yin, and S. E. Harris, “ Generation of Narrow Bandwidth Paired Photons: Use of a Single Driving Laser, ” *Phys. Rev. Lett.* **97**, 113602 (September 2006)

(3) S. Du, J. Wen, M. H. Rubin, and G. Y. Yin, “ Four-Wave Mixing and Biphoton Generation in a Two-Level System, ” *Phys. Rev. Lett.* **98**, 053601 (February 2007).

(4) S. Du, J. Wen, M. H. Rubin, and G. Y. Yin, “Four-Wave Mixing and Biphoton Generation in a Two-Level System,” *Phys. Rev. Lett.* **98**, 053601 (2007).

(5) Jianming Wen, Shengwang Du, and Morton H. Rubin, “Biphoton Generation in a Two Level Atomic Ensemble,” *Phys. Rev.* **A75**, 033809 (2007).

(6) P. Kolchin, “Electromagnetically-Induced-Transparency-Based Paired Photon Generation,” *Phys. Rev.* **A75**, 033814 (2007).

(7) Shengwang Du, Eun Oh, Jianming Wen, and Morton H. Rubin, “Four-wave Mixing in three-level Systems: Interference and Entanglement,” *Phys. Rev.* **A 76**, 013803 (2007).

(8) Jianming Wen, Shengwang Du, and Morton H. Rubin, “Spontaneous Parametric Down-Conversion in a Three-Level System,” *Phys. Rev.* **A76**, 013825 (2007).

(9) Shengwang Du, Pavel Kolchin, Chinmay Belthangady, G.Y. Yin, S.E. Harris, “Subnatural Linewidth Biphotons with Controllable Temporal Length,” *Phys. Rev. Lett.* **100**, 183603 (May 2008).

(10) S. E. Harris, “Nonlocal Modulation of Entangled Photons,” *Phys. Rev.* **A78**, 021807 (August 2008).

(11) Pavel Kolchin, Chinmay Belthangady,Shengwang Du, G.Y. Yin, and S.E. Harris, "Electro-Optic Modulation of Single Photons," *Phys. Rev. Lett.* **101**, 103601 (2008).

(12) Shengwang Du, Chinmay Belthangady, Pavel Kolchin, G.Y. Yin, and S.E. Harris, "Observation of Optical precursors at the Biphoton Level," *Opt Lett*, **33**, 2149 (2008).

(13) Chinmay Belthangady, Shengwang Du, Chih-Sung Chuu, G.Y. Yin, and S. E. Harris, "Modulation and Measurement of Time-Energy Entangled Photons," Phys. Rev. A 80, 031803(R) (2009)

(14) S. Sensarn, G.Y. Yin, and S.E. Harris, "Observation of Nonlocal Modulation with Entangled Photons," Phys. Rev. Lett. 103, 163601 (October, 2009).

(15) C.Belthangady, C. Chuu, I. A. Yu, G.Y. Yin, J. M. Kahn, and S.E. Harris,"Hiding Single Photons With Spread Spectrum Technology", *Phys. Rev. Lett.*, (to be published)

B Construction and Operation of the 2-D MOT

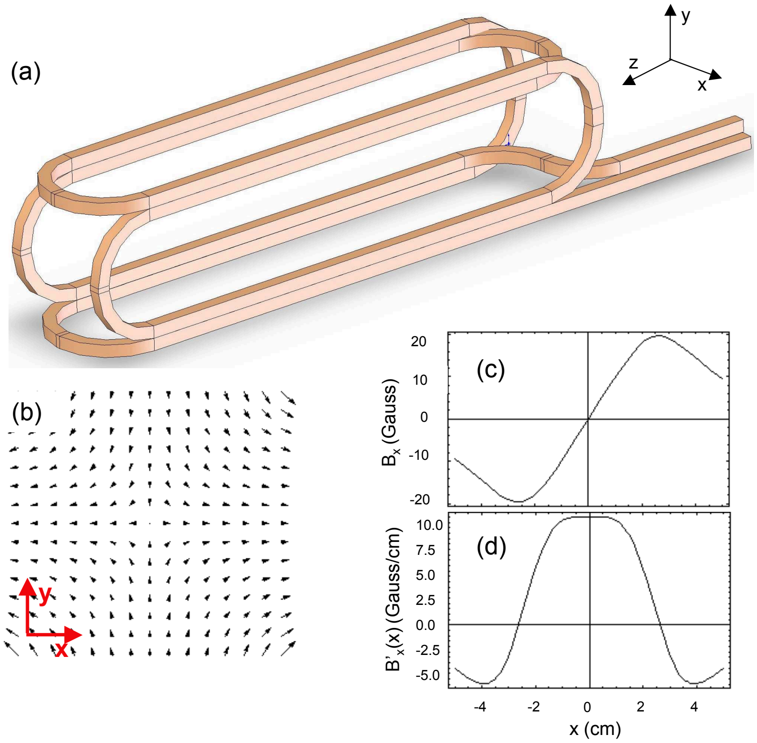

Figure 24: Magnetic field coil and field geometry for a two-dimensional magneto-optic trap (2D MOT). (a) The coil used to produce the linearly varying magnetic field. (b) Magnetic field in the $x-y$ plane. (c) Magnetic field as a function of x coordinate for coil current of 62A. (d) Gradient of the magnetic field as a function of x coordinate. The field gradient at the center of the trap is about 10 gauss/cm.

Trapping of neutral atoms in a MOT is accomplished by applying a magnetic field which varies linearly with the spatial coordinate around the region where the atoms are to be trapped. To trap the atoms in a cigar shaped MOT, we provide spatial confinement along the two transverse directions only, with no magnetic field gradient along the longitudinal axis. Instead of the anti-Helmholtz coils of a 3D MOT, we use an elongated coil as shown in Fig.24(a). This coil provides a magnetic field gradient of about 10 gauss/cm (at a coil current of 62 A) in the transverse direction and an almost negligible gradient along the longitudinal z direction. The coil is shaped like a racetrack and is made with a square copper wire of 5 mm size with a hollow core. Water is circulated through this core to cool the coil and allow operation up to about 100A. The shape of the coil is chosen to reduce its inductance and to therefore facilitate fast switch on and switch off of the coil current. Fig. 24(b) shows a field plot of the magnetic field in the transverse plane. At the center of the trap, the magnetic field is zero and away from this center it increases linearly as a function of the radial coordinate. Fig. 24 (c) and (d) show the magnitude of the magnetic field and its gradient as a function of the distance from the center of the trap.

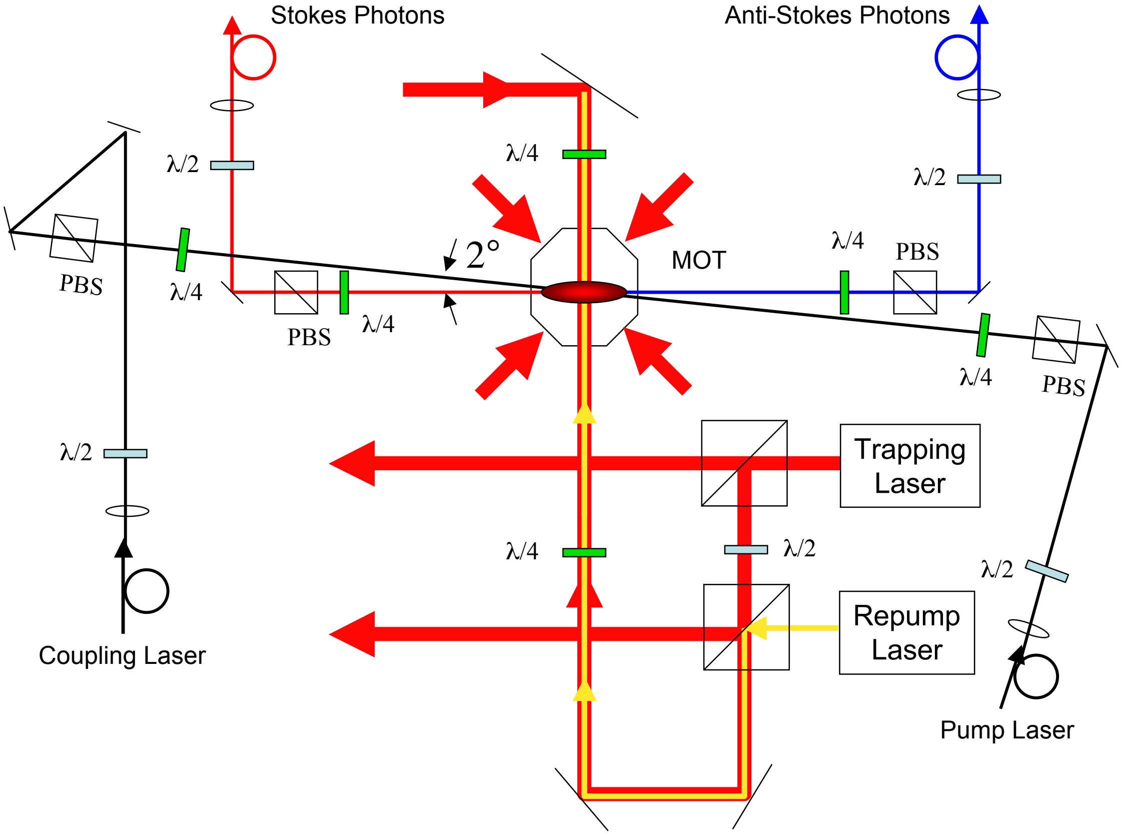
Stokes Photons
Anti-Stokes Photons
λ/4
λ/2
λ/2
λ/4
PBS
2°
MOT
λ/4
PBS
PBS
λ/4
PBS
λ/4
λ/4
PBS
λ/2
Trapping Laser
λ/4
λ/2
λ/2
Repump Laser
Coupling Laser
Pump Laser

Figure 25: Optical layout of 2D MOT and biphoton generation experiment.

C Optical Layout

Fig. 25 shows the layout of the MOT beams and the EIT lasers. The trapping laser is divided into four beams two of which counterpropagate along an axis perpendicular to the axis of the MOT. The remaining two beams are sent long an axis set at 45 degrees to the

MOT axis. The power distribution between the beams is set to optimize the shape of the MOT and to ensure that the atom cloud expands isotropically when the magnetic field is switched off. Of importance, there are no trapping beams and no magnetic field gradient along the axis of the MOT. The repump laser beam is sent at right angles to the MOT axis. The trapping and MOT beams are 2 cm in diameter. The pump laser beam has a $1/e^2$ diameter of 1.46 mm and is circularly polarized ($\sigma-$). The coupling laser beam has a diameter of 1.63 mm and has the opposite polarization ($\sigma+$). The pump and coupling laser axis forms an angle of 2° with the MOT axis. Stokes and anti-Stokes photons are collected along the axis of the MOT. The Stokes and anti-Stokes fiber-to-fiber coupling efficiency is 70% and their $1/e^2$ diameter is 220 μm. Quarter-wave plates and polarization beam-splitters are used to select particular polarizations of the Stokes and anti-Stokes photons and also provide an additional level of filtering of the generated photons from the strong pump and coupling beams. To measure the optical depth and EIT, a weak probe beam is sent through the Stokes fiber and its transmission though the MOT as a function of the detuning from line center is recorded using a photomultiplier tube (PMT).

D Lasers

The wavelengths of the lasers used in MOT preparation depends upon the choice of the atoms used in the trap. Our 2D MOT, as originally designed, trapped ^{85}Rb and some of the early experiments were performed on this system. In order to implement an optical pumping scheme, we later switched to a ^{87}Rb MOT and some later experiments described in this report have been done with ^{87}Rb atoms. Rubidium was chosen because of the large hyperfine splitting of the $5P_{1/2}$ and $5P_{3/2}$ levels. In alkali atoms of lower atomic weights, the hyperfine splitting is of smaller magnitude. Another important factor that led to the choice of Rubidium was the ready availability of commercial lasers at the Rubidium D_1 and D_2 transitions.

Our optical system consists of several lasers with output frequencies locked to various Rubidium transitions. For laser cooling and trapping and for biphoton generation it is of utmost importance that the frequencies of these lasers be controlled to a high degree of

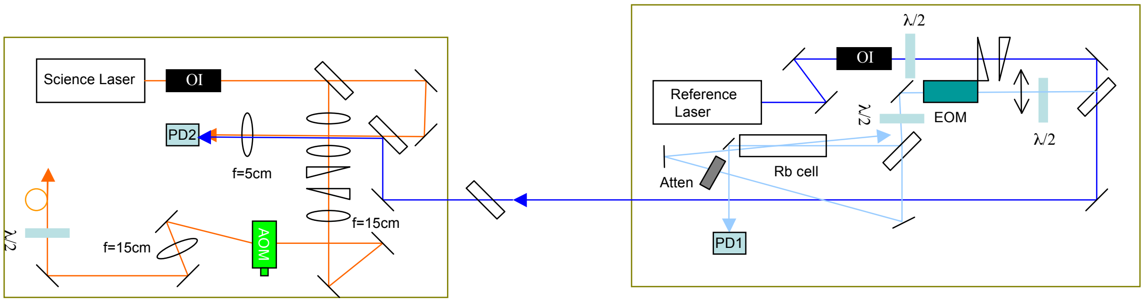

Figure 26: Locking mechanism of the MOT and EIT lasers. A reference laser (right) is first locked to a Doppler free peak of ^{85}Rb using a saturation spectroscopy set-up. Light from the reference laser is mixed with a portion of the light coming from the science laser (left) on a fast photodetector to generate a beat note. The beat note is stabilized using a phase-locked loop to lock the science laser relative to the reference laser.

precision. In the experiment this is done by locking first, a reference laser to one of the peaks of a Doppler free saturation spectroscopy spectrum. The other lasers are locked relative to this reference laser by mixing a part of the output of these lasers with the reference laser beam and then using phase-locked loops to stabilize the resulting beat notes.

A schematic of the locking scheme is shown in Fig. 26. A small portion of the light coming from an external cavity diode laser, referred to henceforth as the reference laser, is sent through an electro-optic phase modulator (Thorlabs EO-PM-NR-C1, half-wave voltage $V_\pi \approx 175V$) driven with a sinusoidal voltage with a frequency of 100 MHz and a peak-to-peak amplitude of about 50V. As a result of this phase modulation, the instantaneous frequency of the laser light varies sinusoidally as a function of time. This beam is then sent through a room temperature Rubidium cell to a photodiode (PD1). To see the Doppler-free saturation spectroscopy peaks, a portion of this phase modulated beam is reflected back into the cell as shown in the figure. For lasers locked to the Rubidium D1 line (795nm), the reference laser is locked to the crossover peak of the $F = 3 \rightarrow F' = 2$ and $F = 3 \rightarrow F' = 3$ transitions of ^{85}Rb. For the D2 line (780nm), the reference laser is locked to the crossover peak of the $F = 3 \rightarrow F' = 2$ and $F = 3 \rightarrow F' = 4$ transitions of ^{85}Rb. The lasers are locked to the maxima of the crossover peaks using the technique of Pound, Drever and Hall.

After the reference laser has been locked, a portion of the light from the laser is mixed with a part of the beam of the science laser as shown in Fig. 26. The photodiode PD2

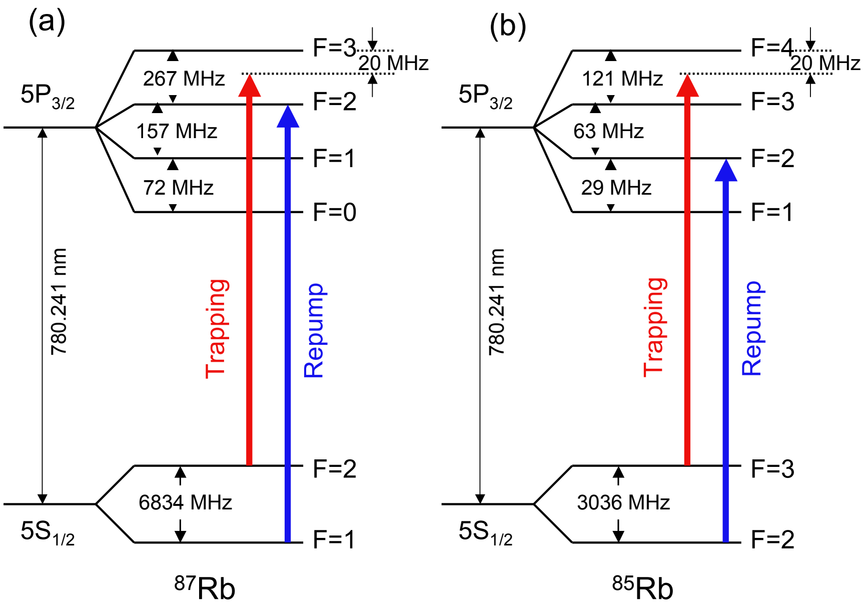

Figure 27: Lasers used to prepare MOT. The trapping laser cools and traps atoms. The repump laser pumps atomic population to the upper ground state for laser cooling. (a) ^{87} Rb energy level diagram for D_2 line and laser positions. The trapping laser is red-detuned by 20 MHz from the cycling $|2\rangle \rightarrow |3\rangle$ transition. The repump laser keeps the $F = 1$ state empty. (b)^{85} Rb energy level diagram for D_2 line and laser positions for cooling and trapping.

outputs a beat note at a frequency equal to the difference between the frequencies of the reference and science lasers. This beat note is then frequency stabilized to that of a local oscillator using a phase-locked loop. The frequency of the local oscillator can be varied to tune the science laser to the desired Rubidium transition.

The primary laser used for laser cooling is a Titanium Sapphire laser (Coherent MBR 110) pumped by a diode pumped ND-YAG laser (Coherent Verdi V10). This laser has a peak output of about 650 mW and is red detuned by about 20 MHz from the $|5S_{1/2}F = 2\rangle \rightarrow |5P_{3/2}, F' = 3\rangle$ transition of ^{87}Rb to trap atoms of this isotope. Due to the proximity of the other levels of the $5P_{3/2}$ manifold, there is a finite probability of exciting the atoms to the $F' = 1$ and $F' = 2$ levels. Atoms thus excited may, through spontaneous emission, decay down to the $|5S_{1/2}, F = 1\rangle$ level and are then no longer cooled by the trapping laser. To return these atoms back to the$|5S_{1/2}, F = 2\rangle$ state, a second laser, called the repump laser tuned on resonance with the $|5S_{1/2}F = 1\rangle \rightarrow |5P_{3/2}, F' = 2\rangle$ transition is used. Fig. 27 shows the positions of the trapping laser and repump lasers used to trap ^{87}Rb (a) and ^{85}Rb

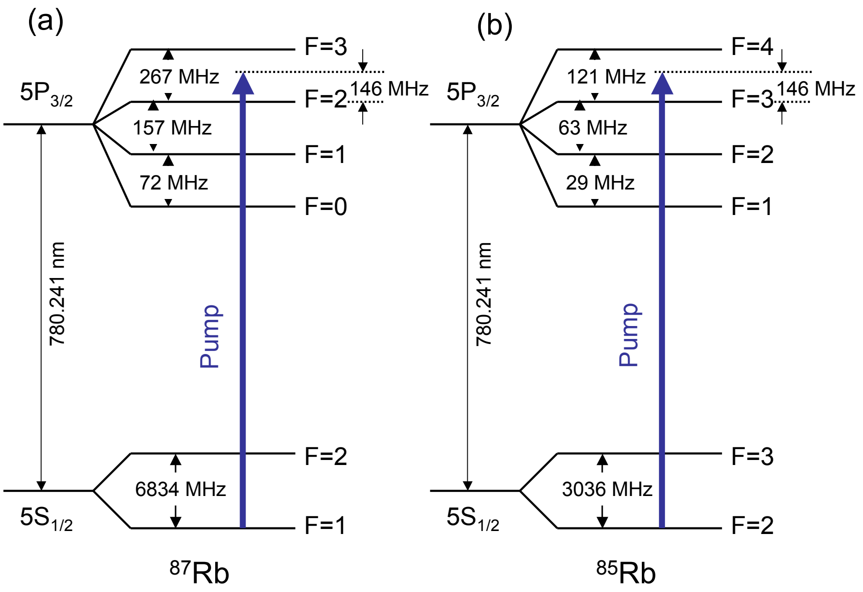
(a)
5P3/2
267 MHz
157 MHz
72 MHz
F=3
F=2
F=1
F=0
146 MHz
780.241 nm
Pump
6834 MHz
F=2
F=1
5S1/2
87Rb
(b)
5P3/2
121 MHz
63 MHz
29 MHz
F=4
F=3
F=2
F=1
146 MHz
780.241 nm
Pump
3036 MHz
F=3
F=2
5S1/2
85Rb

Figure 28: Locking position of the pump laser used in biphoton generation for ^{87}Rb (a) and ^{85}Rb (b).

(b) atoms. A 780nm external cavity diode laser (ECLD) (Sacher Lasertechnik Littrow TEC series) with a peak power of ≈ 200 mW is used as the repump laser. These lasers are locked using the technique described earlier.

In Fig. 28 and Fig. 29, we show the locking positions of the lasers used for EIT measurements and for biphoton generation. The pump laser (Sacher Lasertechnik Littman TEC series) operates at 780nm and is blue-detuned 146 MHz from the $5S_{1/2}F = 2 \rightarrow 5P_{3/2}F' = 3$ transition of ^{85}Rb or the $5S_{1/2}F = 1 \rightarrow 5P_{3/2}F' = 2$ transition of ^{87}Rb as shown in Fig. 28. The coupling laser (New Focus Vortex diode laser) operating at 795nm is locked on the D1 line as shown in Fig. 29. The probe laser beam is generated by sending a portion of the coupling laser light through a double-pass acousto-optic modulator (AOM) operated at a frequency of ≈ 1.57 GHz (for ^{85}Rb) or ≈ 3.47 GHz for ^{87}Rb. The probe frequency can be swept by 40 MHz on either side of the transition to perform optical depth and EIT measurements.

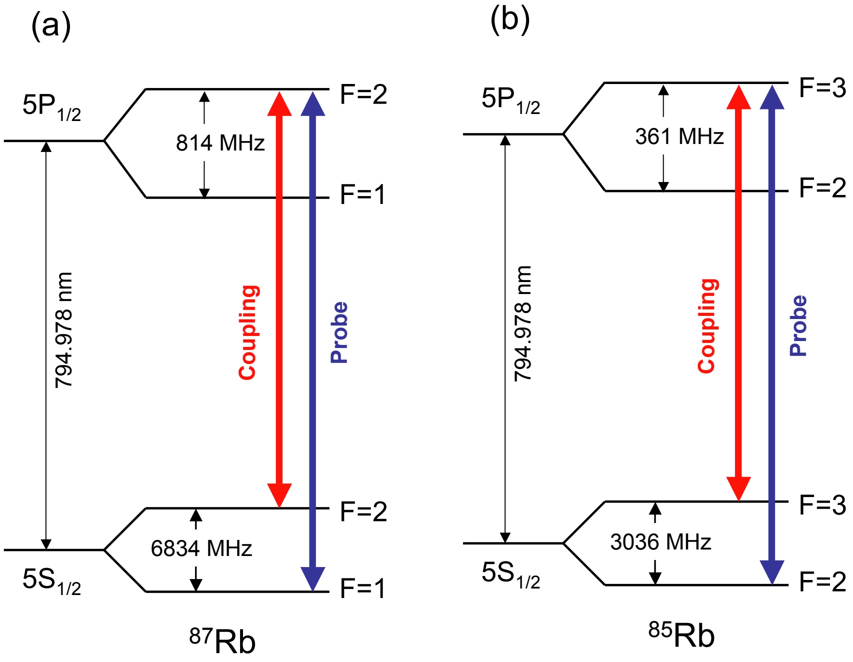

Figure 29: Locking position of the coupling and probe lasers used in EIT measurements and biphoton generation for ^{87}Rb (a) and ^{85}Rb (b).

E Vacuum System

The MOT is prepared in a ultra-high vacuum system consisting of an octagonal ceramic and glass cell [Fig. 30 (a)] mounted on a six-way cross connected to a pumping station. The pumping system consists of a roughing pump, a turbo pump and an ion pump. The vacuum assembly is shown in Fig. 30(b). The turbo pump (Varian Turbo-V70) is used during initial pump down and when baking the system. It is then switched off and the ion pump (Varian VacIon Plus 40 StarCell) is used to obtain a vacuum of about 10^{-8} torr. Small leaks in the interface between the windows and the alumina cell limit the vacuum to this value. In the absence of such leaks, vacua of the order of 10^{-10} should be achievable. To one port of the six-way cross an electrical feed-through is connected and four Rubidium dispensers are spot welded between the terminals. When a current is sent through these terminals, the dispensers are heated to a high temperature and release an isotopic mixture of ^{85}Rb and ^{87}Rb atoms into the vacuum system. Depending on the positions of the laser locks, either of these atomic species can be trapped in the MOT.

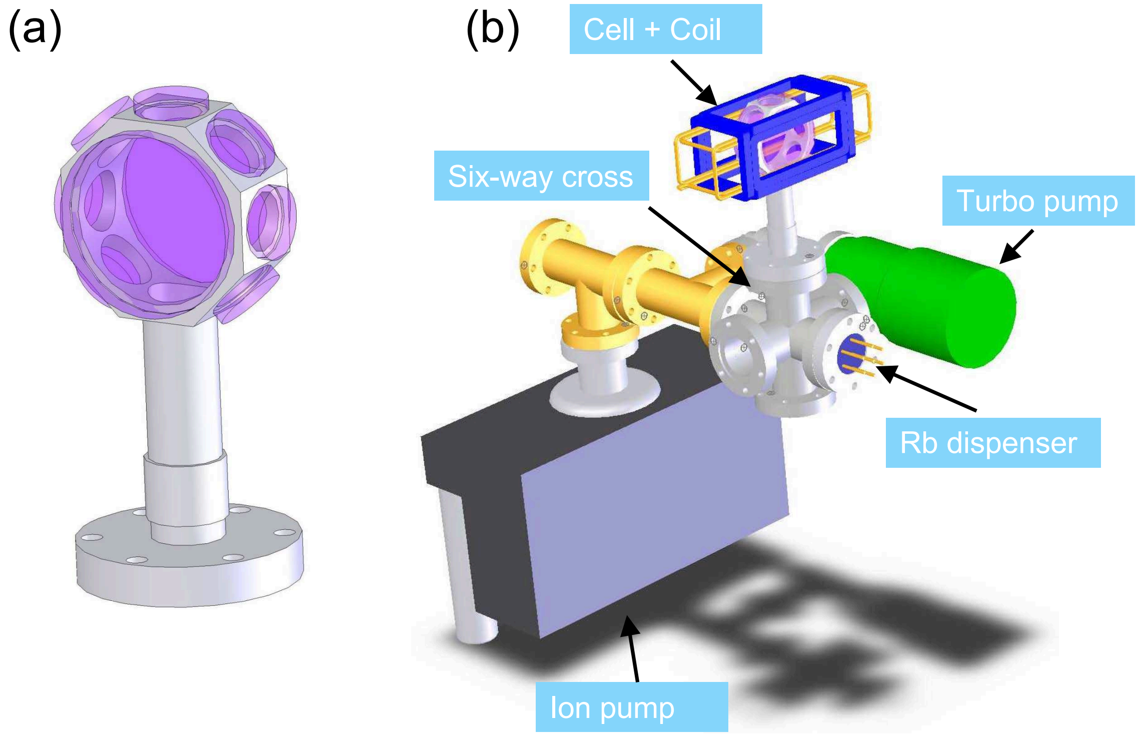

Figure 30: (a) Octagonal vacuum cell. The cell is machined from alumina and anti-reflection coated windows are bonded onto its surfaces. (b) The vacuum assembly showing the octagonal cell and vacuum pumps. Rubidium dispensers are spot-welded to an electrical feedthrough connected to one flange of the six-way cross.

F Experimental Cycle

The lasers locked to the various Rubidium lines are switched on and off in a fixed sequence during the biphoton generation experiment. The switching of the laser beams is done using AOMs (ISOMET 1206C) operating at 110 MHz and with a transmission of ≈ 70-80% in the first order diffracted beam. The AOMs are driven by home-built RF drivers and the relative timing of the lasers is controlled by a series of timing boxes (Stanford Research Systems DG535 Digital Pulse Generator) which have a resolution of 1 ps. The duration of the experiment is divided into time slots of length equal to the inverse of what we call the repetition rate. When the repetition rate is 200 Hz, for example, the experimental cycle i.e. the length of this time slot is 5 ms. During this 5 ms cycle, the trapping and repump lasers are kept on for about 4.5 ms to prepare the MOT. During the remaining 500 μs, the

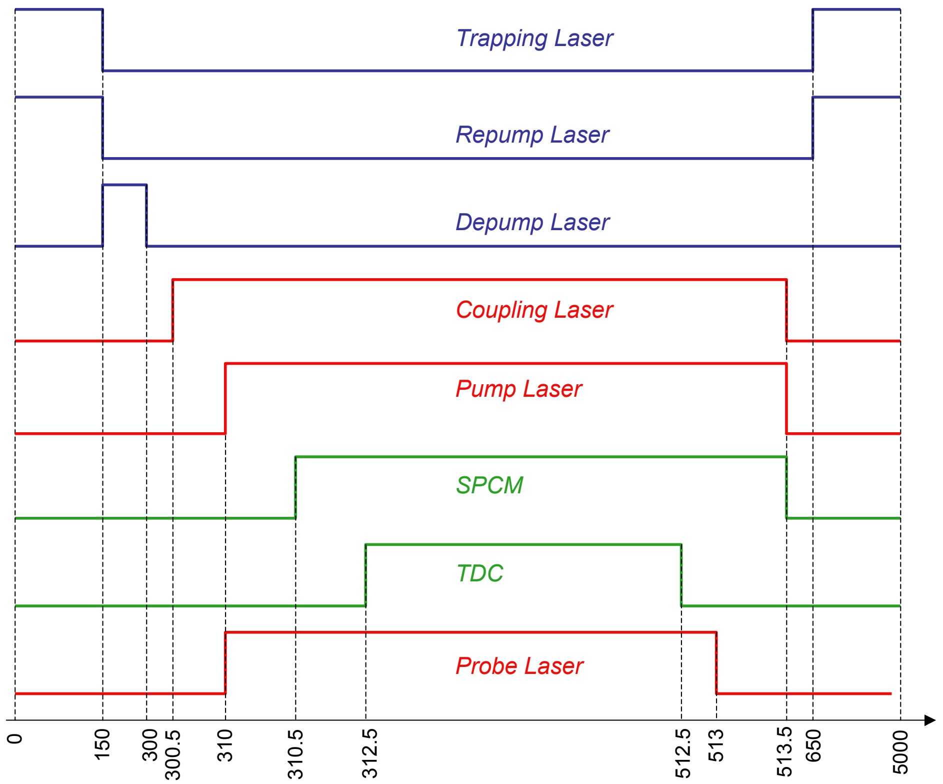

Figure 31: Timing sequence of laser and detector operation. The cooling lasers are switched off during the experimental window. All times are in microseconds.

trapping and repump lasers are switched off and the pump and coupling lasers are switched on for the biphoton generation experiment or the coupling and probe lasers are turned on for EIT/OD measurements. For all the experiments described in this report, the MOT magnetic field continued to remain on through the entire experimental cycle. A schematic of the experimental cycle is shown in Fig.31. The cycle begins with the arrival of a trigger signal at $t = 0$. The trapping and repump lasers are switched off 150 μs after the arrival of the trigger pulse. A depump beam is then turned on for 150 μs to transfer the atomic population from the upper $5S_{1/2}$ state to the lower $5S_{1/2}$ state. The coupling laser and pump lasers are then switched on 0.5 μs and 10 μs respectively after the depump beam has been turned off. The cloud of Rubidium atoms now starts emitting paired Stokes and anti-Stokes photons. The single photon counting modules (SPCM) and the time-to-digital converter (TDC) are then activated to record the coincidences between the photons as shown in the figure. The photon counting equipment and the pump and coupling lasers are turned off

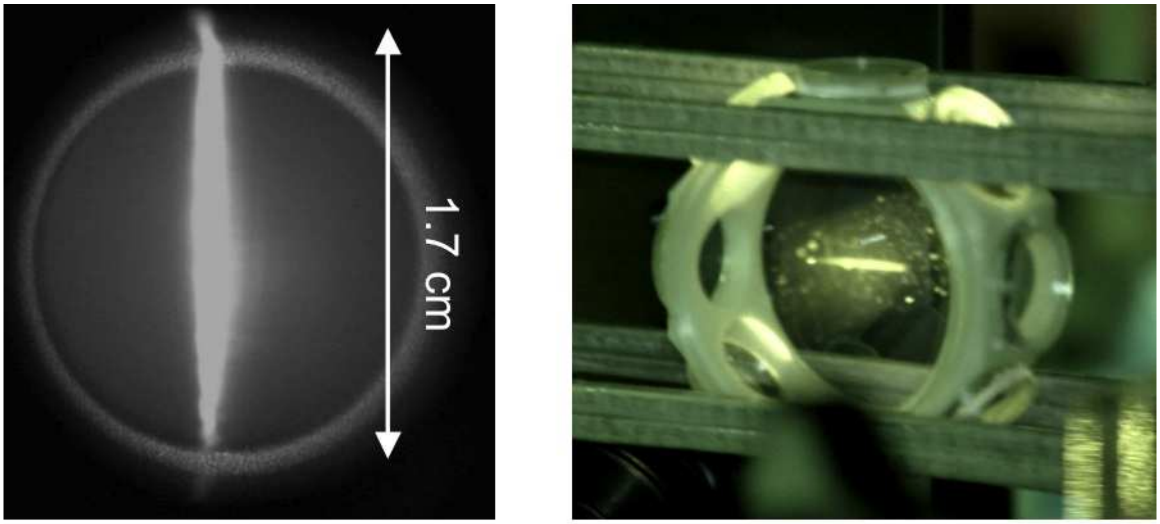

Figure 32: The two-dimensional MOT atom cloud at left and the atom cloud imaged through the vacuum cell on the right.

and the cooling lasers are turned back on 650 μs after the arrival of the trigger pulse and continue to remain on till the end of the experimental cycle. In this manner, the MOT is operated with a 10 percent duty cycle with the MOT-preparation time equal to 4.5 ms and the experimental window for photon counting equal to about 500 μs. To measure the optical depth and EIT curves, probe and coupling lasers are used during the experimental window. Their timing is shown in the figure. The other lasers and the photon counting equipment remain off during these measurements.

G MOT Characteristics

A picture of the 2D MOT is shown in Fig. 32. The cloud is about 1.7 cm in length and has an aspect ratio of 25. The optical depth of the MOT increases as the current to the Rubidium getters is increased. The maximum optical depth observed in our experiments is 62. From the optical depth measurement, we estimate that there are approximately 10^8 atoms trapped in the MOT.

An optical depth measurement on the $|5S_{1/2}, F = 2\rangle \rightarrow |5P_{3/2}, F' = 3\rangle$ transition of ^{85}Rb is shown in Fig. 33 (a). The blue trace is the transmission of the probe beam as a

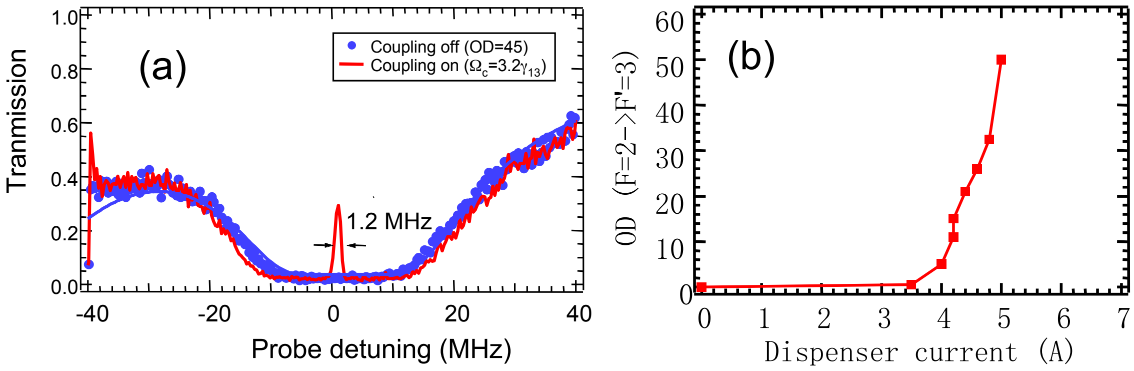

Figure 33: Optical depth and EIT measurements of the 2D MOT. (a) Transmission of the probe beam as a function of detuning from line center with (red) and without (blue) the coupling laser. (b) Optical depth as a function of the dispenser current.

function of detuning from line center (0 MHz) without the coupling laser. The optical depth as estimated by a nonlinear curve fit to this data is 45. When coupling laser is switched on, a narrow transparency window opens up at line center as shown by the red trace. The width of the transparency window is about 1.2 MHz which is smaller than the natural linewidth of Rubidium (5.9 MHz). We thus have subnatural EIT. In Fig. 33 (b) we show the optical depth measured on this transition as a function of the current sent through the Rubidium dispenser. To reduce the risk of exhausting the Rubidium dispensers, we always operate the dispensers below 5A.

H Chapter 4 of Pavel Kolchin's Dissertation

4.1 Theory of paired photon generation 30
4.2 Heisenberg-Langevin description 32
4.3 Solution of Coupled Equations 34
4.4 Characteristics of generated photons 36
4.5 Ideal Spontaneous Parametric Down Converter 39
4.6 EIT based Paired Photon Generator 41
4.7 Mathematical Apparatus 51

The original dissertation pp. 29 - 65 are included after this page.

Chapter 4

Theory of EIT based Paired Photon Generation

Correlated and entangled photon pairs are widely used in quantum communication, quantum cryptography [31] and quantum imaging [32, 33]. These photon pairs are usually produced via spontaneous parametric down conversion in nonlinear crystals. A few years ago a new approach to the generation of paired photons has been experimentally demonstrated by two groups, both use electromagnetically induced transparency (EIT) to generated paired photons in an otherwise opaque atomic medium. Working with hot atoms, Lukin and colleagues have demonstrated correlation between generated pulses of light, as well as storage and delayed extraction [34]. Working with a MOT, Kimble and colleagues have shown the generation of nonclassical photon pairs with a programmable delay [35]. Recently, the Harris research group at Stanford has demonstrated generation and rudimentary waveform control of narrow band biphotons [36]. More recently, Kolchin and colleagues have shown paired photon generation with a single pump beam in a right angle geometry and paired photon generation in the ensemble of cold two-level atoms [37]. A long coherence length and a controllable bandwidth of the generated paired photons are the advantages of the new approach, which might be useful for such applications as long distance quantum communication [38] as well as biphoton waveform control and shaping [1].

4.1 Theory of paired photon generation

This chapter describes the theory of correlated paired photon generation in a collection of double Λ-type atoms [39]. Using the Heisenberg-Langevin method we evaluate and analyze spectral characteristics of the generated Stokes and anti-Stokes photons and their time-correlation properties. Of importance, we predict the regime when the correlation time of generated photons is determined by the group delay caused by EIT. This theoretical prediction as well as some theoretical aspects of this work has been outlined in Ref. [36]. The complete theoretical treatment of paired photon generation with and without the approximation, that the atomic population remains in the ground state, has been given in Ref. [39].

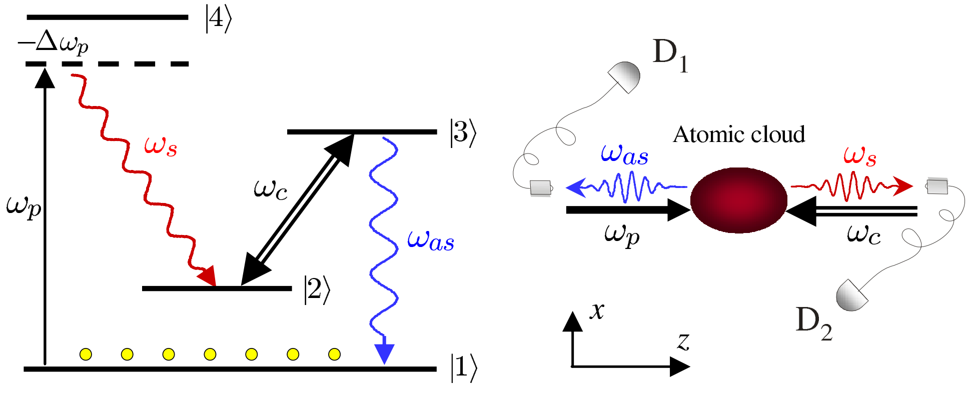

Figure 4.1: Energy level diagram and schematic for spontaneous backward-wave paired photon generation in an atomic cloud formed by double-Λ type atoms. In the presence of the pump and coupling lasers phase-matched, counter-propagating Stokes and anti-Stokes photons are generated into opposite directions.

The schematic of the process considered here is shown in Fig. 5.7. In the presence two cw beams termed as the pump and coupling lasers with frequencies ω_p and ω_c, paired spontaneous photons termed as Stokes and anti-Stokes are generated in the atomic cloud and propagate in opposite directions along the z axis. In order to keep the parametric gain small we choose the pump beam to be weak and detuned from the resonance transition $|1\rangle \rightarrow |4\rangle$. The intense coupling beam is tuned to resonance with the $|2\rangle \rightarrow |3\rangle$ transition to enhance the atom-field interaction and provide EIT for the generated anti-Stokes photon. Under such conditions we expect a small fraction of the atomic population to be in the excited states while most of it remains in the ground state $|1\rangle$. The frequencies of the generated photons obey the energy conservation $\omega_s + \omega_{as} = \omega_p + \omega_c$. In the presence of EIT the anti-Stokes photon escapes out of the atomic cloud with very slow group velocity.

---

[1] In a right-angle geometry, where Stokes and anti-Stokes photons are generated and collected at right angles from the direction of the pump-coupling axis, applying the absorption mask on the pump beam allows us to create a biphoton with a precribed waveform.

We note the connection to earlier work: Two-photon entanglement in type-II SPDC has been analyzed [40]. The possibility of quantum correlated and squeezed fields in backward wave EIT system has been predicted [41] and large parametric gain and oscillations have been observed [42]. Control of single photons has been discussed [43]. We also note the early studies on double-Λ atomic systems [44].

In this chapter we review and discuss in detail the system dynamics putting emphasis on the influence of the EIT window on paired photon generation bandwidth. We show that at low parametric gain the atomic system can operate in two different regimes. In the first regime, where the group delay is small, the intensity correlation function shows Rabi oscillations. In the second regime, where the optical depth of the atomic sample and the group delay are large, phase-matching becomes the dominant process that controls the shape of the intensity correlation function. We examine the conditions required for the system to operate in the oscillatory and group delay regimes and discuss corresponding Stokes and anti-Stokes spectral generation rates. In particularly, we predict that the group delay regime requires the optical depth much higher that 10. This point has been missed in our earlier publication [36].

We also extend our theoretical treatment of paired photon generation to go beyond the ground state approximation. This allows us to properly include and analyze the effect of Langevin noise fluctuation on the atomic system and solve the problem of its return to the ground state after the emission of Stokes and anti-Stokes photon pairs. We also address the important questions: 1) "What are the effects of the optical thickness of the atomic sample on paired and single photon generation?" 2) "Does every Stokes photon have its paired anti-Stokes photon?"

We introduce and derive the biphoton wavefunction taking into account Langevin noise terms. We also derive and discuss the relation of the Stokes photon count rate to the classical gain coefficient in the Stokes channel.

4.2 Heisenberg-Langevin description of paired photon generation

We consider a collection of identical double Λ-type atoms uniformly distributed within a pencil-shaped volume with cross section S and length L. We assume that the atomic sample is optically thin in the transverse direction, so that there is no radiation trapping effect in this direction. No restrictions are imposed on the optical thickness of the atomic sample in the z direction. We also assume that the pump and the coupling beams counter-propagate undepleted through the atomic medium. Under these assumptions we consider propagation of a single transverse spatial mode of radiation along the z axis. The pump and coupling laser beams are treated as classical quantities and their interaction with the medium is described semi-classically. In order to allow for the spontaneous initiation of the parametric fluorescence process, the generated weak Stokes and anti-Stokes fields are described by quantum-mechanical operators, in slowly varying envelope approximation:

$$\hat{E}_j^{(+)} = \sqrt{\frac{\hbar\omega_j}{2\epsilon_0 V}}\hat{a}_j(z,t)\exp\left(-i\omega_j t + i\vec{k}_j\cdot\vec{z}\right), \tag{4.1}$$

where subscript j denotes either Stokes or anti-Stokes photon, $\omega_s = \omega_4 - \omega_2 + \Delta\omega_{14}$, $\omega_{as} = \omega_3 - \omega_1$, $V = L \times S$ is the interaction volume.

Adopting the notations of Lukin and Fleischhauer [45, 46], in the rotating wave approximation we write the interaction Hamiltonian in continuous form as

$$\hat{V} = -\frac{\hbar N}{L}\int\limits_0^L dz\Big(\Delta\omega_{14}\tilde{\sigma}_{44}(z,t) + g_{31}\hat{a}_{as}(z,t)\tilde{\sigma}_{31}(z,t) \\ + \frac{\Omega_c}{2}\tilde{\sigma}_{32}(z,t) + \frac{\Omega_p}{2}\tilde{\sigma}_{41}(z,t) + g_{42}\hat{a}_s(z,t)\tilde{\sigma}_{42}(z,t) + h.c.\Big), \quad (4.2)$$

where $\tilde{\sigma}_{jk}(z,t)$ are the collective slowly varying atomic operators, defined in the Appendix 4.7.1, N is the total number of atoms in the atomic ensemble, $\Delta\omega_{14}$ is the detuning of the pump laser from the $|1\rangle \rightarrow |4\rangle$ transition, $\Omega_c = \frac{2\wp_{23}E_c}{\hbar}, \Omega_p = \frac{2\wp_{41}E_p}{\hbar}$ are pump and coupling laser Rabi frequencies with E_p, E_c as the complex amplitudes of the electric fields, $g_s = \frac{\wp_{42}\mathcal{E}_s}{\hbar}$ and $g_{as} = \frac{\wp_{31}\mathcal{E}_{as}}{\hbar}$ are the coupling constants with $\wp_{jk}$ as the dipole moment for the $|j\rangle \rightarrow |k\rangle$ transition and $\mathcal{E}_j = \sqrt{\frac{\hbar\omega_j}{2\epsilon_0 V}}$ as the electric field of a single photon.

The propagation of the Stokes and anti-Stokes fields and their interaction with the atoms are described by the set of Maxwell and Heisenberg-Langevin equations. The Heisenberg-Langevin equations are responsible for the atomic evolution:

$$\frac{\partial}{\partial t}\tilde{\sigma}_{jk} = \frac{i}{\hbar}[\hat{V}, \tilde{\sigma}_{jk}] - \gamma_{jk}\tilde{\sigma}_{jk} + r^A_{jk} + \tilde{F}_{jk}, \quad (4.3)$$

where γ_{jk} are the dephasing rates, r^A_{jk} are the spontaneous emission rates, $\tilde{F}_{jk}(z,t)$ are the collective atomic δ-correlated Langevin noise operators. The full set of the Heisenberg-Langevin equations is shown explicitly in Sec. 4.7.2

The fluctuations of δ-correlated collective Langevin noise operators $\tilde{F}_{jk}(z,t)$ is given by

$$\langle\tilde{F}_{jk}(z,t)\tilde{F}_{j'k'}(z',t')\rangle = \frac{L}{N}\mathcal{D}_{jk,j'k'}(z,t)\delta(t-t')\delta(z-z'), \quad (4.4)$$

where $\mathcal{D}_{jk,j'k'}$ is a Langevin diffusion coefficient. The derivation of Eq.(4.4) and relevant diffusion coefficients is shown in Sec. 4.7.4.

The evolution of the annihilation a_s and creation $a_{as}^{\dagger}$ operators for the slowly varying Stokes and anti-Stokes fields is described by the coupled propagation equations

$$\begin{aligned} \left(\frac{\partial}{\partial t} + c\frac{\partial}{\partial z}\right) \hat{a}_s(z,t) &= i g_s N \tilde{\sigma}_{24}(z,t) \\ \left(\frac{\partial}{\partial t} - c\frac{\partial}{\partial z}\right) \hat{a}_{as}^{\dagger}(z,t) &= -i g_{as} N \tilde{\sigma}_{31}(z,t). \end{aligned} \tag{4.5}$$

The following analysis of the system involves calculation of the expected values of quantum field operators and their combinations. We note that in the Heisenberg picture operators evolve and the system is always in its initial state, which in our case corresponds to no Stokes and anti-Stokes input beams at the left and right boundaries.

4.3 Solution of Coupled Equations

Due to complexity and nonlinearity it is not possible to obtain an analytic solution for the combined set of the field propagation equations and Heisenberg-Langevin equations. Nevertheless, under the condition that Stokes and anti-Stokes fields are much weaker than the coupling and pump fields, and Stokes and anti-Stokes photon densities are much smaller than the atomic density N/V [45], the Heisenberg-Langevin equations can be linearized with Stokes $\hat{a}_s$ and anti-Stokes $\hat{a}_{as}$ fields as perturbation parameters. The linearization procedure is described in detail in the Appendix 4.7.3.

In order to solve the set of the linearized Heisenberg-Langevin Eq. (4.35) and coupled propagation Eq. (4.5), we first Fourier transform them. Then, extracting the solutions for $\tilde{\sigma}_{24}(\omega), \tilde{\sigma}_{31}(\omega)$ and substituting them into Fourier transformed Eq.(4.5), we obtain the coupled equations for $\hat{a}_s(z,\omega)$ and $\hat{a}_{as}^{\dagger}(z,-\omega)$ in the form

$$\begin{aligned} \frac{\partial \hat{a}_s}{\partial z} + g_R \hat{a}_s + \kappa_s \hat{a}_{as}^{\dagger} &= \sum_{\alpha_i} \xi_{\alpha_i}^{s} \tilde{f}_{\alpha_i} \\ \frac{\partial \hat{a}_{as}^{\dagger}}{\partial z} + \Gamma_{as} \hat{a}_{as}^{\dagger} + \kappa_{as} \hat{a}_s &= \sum_{\alpha_i} \xi_{\alpha_i}^{as} \tilde{f}_{\alpha_i} \end{aligned} \tag{4.6}$$

where $g_R(\omega)$, $\Gamma_{as}(\omega)$ are the Raman gain, EIT profile coefficients respectively, $\kappa_s(\omega)$ and $\kappa_{as}(\omega)$ are Stokes and anti-Stokes mode coupling coefficients. In Eq. 4.6 $\tilde{f}_{\alpha_i}(z,\omega)$ are the renormalized Langevin noise operators: $\tilde{f}_{\alpha_i}(z,\omega) = \sqrt{N/c} \times \tilde{F}_{\alpha_i}(z,\omega)$. The sum is taken over the relevant Langevin noise operators $\{\tilde{f}_{21}, \tilde{f}_{24}, \tilde{f}_{31}, \tilde{f}_{34}\}$.

The general solution of Eq. (4.6) can be written as

$$\begin{pmatrix} \hat{a}_s(L) \\ \hat{a}^{\dagger}_{as}(L) \end{pmatrix} = e^{-\tilde{M}L} \begin{pmatrix} \hat{a}_s(0) \\ \hat{a}^{\dagger}_{as}(0) \end{pmatrix} + \sum_{\alpha_i} \int_0^L dz\, e^{\tilde{M}(z-L)} \begin{pmatrix} \xi^s_{\alpha_i} \\ \xi^{as}_{\alpha_i} \end{pmatrix} \tilde{f}_{\alpha_i} \tag{4.7}$$

where $\tilde{M} = \begin{pmatrix} g_R & \kappa_s \\ \kappa_{as} & \Gamma \end{pmatrix}$

For the following derivation, let us define the coefficients of matrix $e^{-\tilde{M}L}$ as

$$\begin{pmatrix} A_1 & B_1 \\ C_1 & D_1 \end{pmatrix} = e^{-\tilde{M}L} \tag{4.8}$$

Due to the linearity of Eq. (4.7), the unknown variables $a^{\dagger}_s(L)$ and $a_{as}(0)$ of the backward wave problem can be written as a linear combination of the initial boundary values and the noise terms:

$$\begin{pmatrix} \hat{a}_s(L) \\ \hat{a}^{\dagger}_{as}(0) \end{pmatrix} = \begin{pmatrix} A & B \\ C & D \end{pmatrix} \begin{pmatrix} \hat{a}_s(0) \\ \hat{a}^{\dagger}_{as}(L) \end{pmatrix} + \sum_{\alpha_i} \int_0^L dz \begin{pmatrix} P_{\alpha_i} \\ Q_{\alpha_i} \end{pmatrix} \tilde{f}_{\alpha_i} \tag{4.9}$$

where

$$\begin{pmatrix} A & B \\ C & D \end{pmatrix} = \begin{pmatrix} A_1 - \frac{B_1 C_1}{D_1} & \frac{B_1}{D_1} \\ -\frac{C_1}{D_1} & \frac{1}{D_1} \end{pmatrix} \tag{4.10}$$

$$\begin{pmatrix} P_{\alpha_i} \\ Q_{\alpha_i} \end{pmatrix} = \begin{pmatrix} 1 & -\frac{B_1}{D_1} \\ 0 & -\frac{1}{D_1} \end{pmatrix} e^{\tilde{M}(z-L)} \begin{pmatrix} \xi^s_{\alpha_i} \\ \xi^{as}_{\alpha_i} \end{pmatrix}. \tag{4.11}$$

The coefficients A, B, C and D are the functions of ω, whereas $P_{\alpha_i}, Q_{\alpha_i}$ are the functions of ω and z.

4.4 Characteristics of generated photons

4.4.1 Stokes and Anti-Stokes photon generation rates

We evaluate the output generation rates of Stokes and anti-Stokes photons into a single transverse mode, for example, into a pair of mode-matched optical fibers. The generation rates at the corresponding boundaries z_j are

$$R_j = \frac{c}{L}\langle \hat{a}_j^\dagger(z_j,t)\hat{a}_j(z_j,t)\rangle, \tag{4.12}$$

where subscript j denotes either Stokes or anti-Stokes photon, $z_s = L$ and $z_{as} = 0$.

Of importance are the spectral properties of the generated photons. The power spectrum of the output Stokes and anti-Stokes fields are related to their first order coherence functions $G_j^{(1)}(\tau) = \langle a_j^\dagger(z_j,t)a_j(z_j,t+\tau)\rangle$ as

$$R_j(\omega) = \frac{c}{L}\int\limits_{-\infty}^{+\infty} d\tau\, e^{i\omega\tau} G_j^{(1)}(\tau) \tag{4.13}$$

We use the solutions for $a_s(L,\omega)$ and $a_{as}^\dagger(0,-\omega)$ field operators, given by Eq. (4.9), the commutation relations for the input field operators $[a_j(z_j,\omega), a_j^\dagger(z_j,-\omega')] = L/(2\pi c)\delta(\omega+\omega')$ and Eq. (4.41). We apply inverse Fourier transformation $a(t) = \int d\omega e^{-i\omega t}a(\omega)$ and $a^\dagger(t) = \int d\omega e^{-i\omega t}a^\dagger(-\omega)$ and obtain the Stokes and anti-Stokes generation rates from Eq. (4.12) in the form

$$R_s = \int \frac{d\omega}{2\pi}\left(|B|^2 + \sum_{\alpha_i,\alpha_j}\int\limits_0^L dz\, P_{\alpha_i}^* \mathcal{D}_{\alpha_i^\dagger,\alpha_j} P_{\alpha_j}\right) \tag{4.14}$$

$$R_{as} = \int \frac{d\omega}{2\pi}\left(|C|^2 + \sum_{\alpha_i,\alpha_j}\int\limits_0^L dz Q_{\alpha_i} \mathcal{D}_{\alpha_i,\alpha_j^\dagger} Q_{\alpha_j}^*\right) \tag{4.15}$$

The integrands of Eq. (4.14) and Eq. (4.15) are Stokes and anti-Stokes spectral generation rates respectively.

As seen from Eq. (4.14) and Eq. (4.15), Stokes and anti-Stokes spectral generation rates consist of parametric counts, characterized by the transfer functions $C(\omega)$ and $B(\omega)$, and of noise counts, that originate from Langevin noise fluctuations. If the pump is weak and far detuned, $B(\omega) = -C(\omega)$, and therefore the parametric terms in Stokes and anti-Stokes rates are equal. We also note that the contribution of Langevin noise fluctuations to spectral generation rates can not be neglected and becomes dominant at low optical depth of the atomic sample.

Using the commutator conservation relation for the Stokes field at the right boundary $z = L$, obtained from Eq. (4.9), the Stokes spectral generation rate can be expressed as

$$R_s(\omega) = |A|^2 - 1 + \sum_{\alpha_i,\alpha_j} \int\limits_0^L dz P_{\alpha_i} \mathcal{D}_{\alpha_i,\alpha_j^\dagger} P^*_{\alpha_j} \tag{4.16}$$

When the pump is far detuned from the atomic transition and Stokes photon losses are small, the contribution of Langevin noise fluctuation in Eq. (4.16) is negligible. Thus, the Stokes spectral generation rate can be written as

$$R_s(\omega) \approx |A|^2 - 1 \tag{4.17}$$

Eq. (4.17) can be interpreted in terms of the quantum theory of linear amplification [47]: in the absence of the Stokes input beam and losses for the Stokes photon, the Stokes generation rate is just the additive noise caused by the amplification process, that is characterized by the gain coefficient $A(\omega)$.

4.4.2 Two-photon intensity correlation function and biphoton wave-function

In order to address another important issue - the time correlation properties of the generated photons, we calculate the Glauber two-photon correlation function of time delay τ between Stokes and anti-Stokes photons:

$$G^{(2)}_{s-as}(\tau) = \langle \hat{a}^\dagger_s(L,t) \hat{a}^\dagger_{as}(0,t+\tau) \hat{a}_{as}(0,t+\tau) \hat{a}_s(L,t) \rangle \tag{4.18}$$

Using the Stokes and anti-Stokes operators at the boundaries derived earlier [Eq. (4.9)] and the commutator relations for the input fields, we obtain the intensity correlation function as

$$G^{(2)}_{s-as}(\tau) = \iiiint d\omega_1 d\omega_2 d\omega_3 d\omega_4 e^{-i\omega_1 t - i\omega_2(t+\tau) - i\omega_3(t+\tau) - i\omega_4 t} \times \left\langle \hat{a}^{\dagger}_{s}(L,-\omega_1)\hat{a}^{\dagger}_{as}(0,-\omega_2)\hat{a}_{as}(0,\omega_3)\hat{a}_{s}(L,\omega_4)\right\rangle \quad (4.19)$$

The intensity correlation function contains the fourth-order Langevin noise correlations. According to Gaussian moment theorem [48, 49] they can be decomposed preserving the order into the sum of the products of second order Langevin noise correlations. As a result the intensity correlation function can be simplified to

$$\begin{aligned} G^{(2)}_{s-as}(\tau) &= \langle a^{\dagger}_{as}(0,t+\tau)a_{as}(0,t+\tau)\rangle\langle a^{\dagger}_{s}(L,t)a_{s}(L,t)\rangle + |\langle a_{as}(0,t+\tau)a_{s}(L,t)\rangle|^2 \\ &= G^{(1)}_{s}(0) \times G^{(1)}_{as}(0) + |\Phi_{s-as}(\tau)|^2 \end{aligned} \quad (4.20)$$

The first term in Eq. (4.20) represents flat uncorrelated background, the second term, expressed through $\Phi_{s-as}(\tau)$ function, describes the correlation part. $\Phi_{s-as}(\tau)$ is equal to

$$\begin{aligned} \Phi_{s-as}(\tau) &= \langle \hat{a}_{as}(0,t+\tau)\hat{a}_{s}(L,t)\rangle \quad (4.21) \\ &= \frac{L}{2\pi c}\int d\omega\, e^{i\omega\tau}\left(BD^{*} + \sum_{\alpha_i,\alpha_j}\int_{0}^{L} dz Q^{*}_{\alpha_i}\mathcal{D}_{\alpha^{\dagger}_{i},\alpha_j}P_{\alpha_j}\right) \end{aligned}$$

We note that $e^{-i\omega_s t - i\omega_{as}(t+\tau)}\Phi_{s-as}(\tau)$ represents a two photon wavefunction or a biphoton wavefunction on the condition that peak value of normalized $g^{(2)}_{s-as} >> 1$, where $g^{(2)}_{s-as}(\tau) = G^{(2)}_{s-as}(\tau)/(G^{(1)}_{s}(0) \times G^{(1)}_{as}(0))$.

Similarly, we can define $\Phi_{as-s}(\tau) = \langle \hat{a}_{s}(L,t)\hat{a}_{as}(0,t+\tau)\rangle$. This function can be obtained in the form

$$\Phi_{as-s}(\tau) = \frac{L}{2\pi c}\int d\omega\, e^{i\omega\tau}\Big(AC^* + \sum_{\alpha_i,\alpha_j}\int_0^L dz P_{\alpha_i}\mathcal{D}_{\alpha_i,\alpha_j^\dagger}Q^*_{\alpha_j}\Big) \tag{4.22}$$

For a wide range of input parameters we numerically verify that $\Phi_{as-s}(\tau) = \Phi_{s-as}(\tau)$.

For the case where $\Omega_p/\Delta\omega_{14} << 1$ and $\Delta\omega_{14}/\gamma_{14} >> 1$, we numerically verify that the contribution of Langevin noise fluctuations to $\Phi_{as-s}(\tau)$ is negligible, therefore Eq. (4.22) can be simplified to

$$\Phi_{as-s}(\tau) = \frac{L}{2\pi c}\int d\omega\, e^{i\omega\tau}AC^* \tag{4.23}$$

4.5 Ideal Spontaneous Parametric Down Converter

Before we proceed to the discussion of the interesting cases of the atomic correlation functions and photon spectral densities, we want to make an analogy to the well-known parametric down converter in crystals [40]. We consider the ideal model - non-degenerate parametric down converter in which a generated signal photon has a very slow group velocity V_g as compared to an idler photon. We assume that both idler and signal photon escape SPDC without losses, therefore the Langevin noise terms in Eq. (4.6) can be neglected. In crystals the coupling coefficient can be approximated as a constant over the broad spectral range $\kappa_s(\omega) = \kappa_{as}(\omega) = \kappa$. We also neglect Raman gain $g_R(\omega)$ and approximate EIT profile as $\Gamma(\omega) = -i\omega/V_g$. Under these assumptions the signal and idler photons have identical spectral characteristics and rates. Using the Eq. (4.14), we obtain the photon spectral density $R(\omega)$ and spectrally integrated generation rate $R = 1/(2\pi)\int d\omega R(\omega)$ in the form:

$$
\begin{aligned}
R(\omega) &= |\kappa|^2 L^2 \mathrm{sinc}^2\left(\frac{\omega L}{2V_g}\right) \\
R &= V_g |\kappa|^2 L.
\end{aligned}
\tag{4.24}
$$

As seen from Eq. (4.24), the spectral bandwidth of the SPDC in crystals is limited by $\Delta\omega \sim 2\pi V_g/L$ due to the phase mismatch of the off-centered counts resulting from the group delay in the signal channel. In principle, the bandwidth can be made very small by making the group delay $\tau_g = L/V_g$ large. For the atomic system κ is proportional to the atomic density $\mathcal{N} = N/V$, therefore the spectral density of the generated photons scales as $(\mathcal{N}L)^2$. Taking into account that the EIT induced group velocity of a wave is $V_g = \Omega_c^2/(2\gamma_{13}\mathcal{N}\sigma_{13})$, where $\sigma_{13} = \wp_{13}^2\omega_{13}/(c\epsilon_0\hbar\gamma_{13})$ is the atomic cross section of the $|1\rangle \rightarrow |3\rangle$ transition, the total count rate scales linearly with $\mathcal{N}L$.

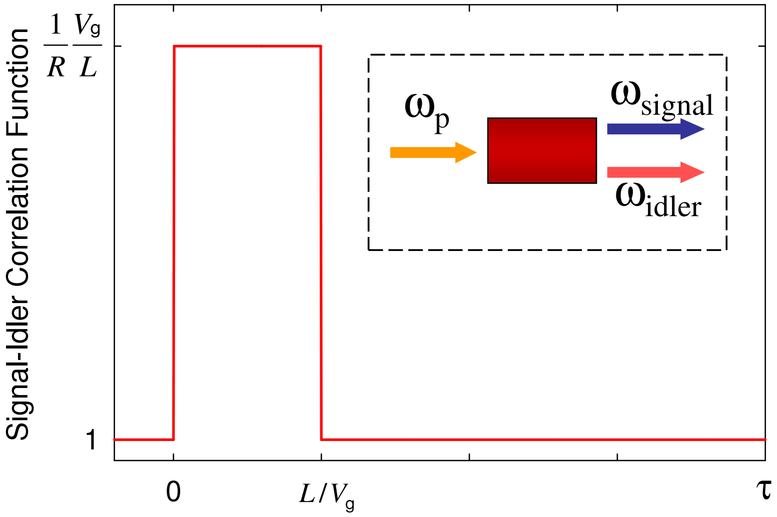

Figure 4.2: Normalized signal-idler intensity correlation function for the ideal SPDC with the condition of a large group delay L/V_g for a signal photon. R is the paired photon generation rate.

Fig. 4.2 shows the normalized signal idler intensity correlation function. Since the probability of emitting a photon pair is uniformly distributed along the crystal of length L and the signal photon has a group delay relative to the idler, the $g_{s-i}^{(2)}(\tau)$

is expected to be the shifted rectangle with the width equal to the group delay $\tau_g = L/V_g$. By varying the group delay we can control the width of the waveform. The peak height of $g^{(2)}_{s-i}$ is equal to $1/(\kappa L)^2$ and can be interpreted as a duty ratio: $g^{(2)}_{s-i} = 1/(R\tau_g)$. In the regime of very small parametric gain $\kappa L << 1$, which can be achieved, for example, by lowering the intensity of the pump, the atomic system can produce highly correlated photon pairs $g^{(2)}_{s-i} >> 1$.

4.6 EIT based Paired Photon Generator

Now we turn from the discussion of the ideal SPDC to the discussion of the EIT based paired photon generator. In the EIT based generator, coupling between Stokes and anti-Stokes modes is bandwidth limited. Moreover, the generated Stokes photon undergoes Raman gain $g_R(\omega)$, whereas a paired anti-Stokes photon propagates slowly and undergoes absorbtion at the poles of EIT profile $\omega = \pm\Omega_c/2$.

We first obtain the coefficients of Eq. (4.6) with the assumption that the pump is weak and far detuned from the $|1\rangle \to |4\rangle$ transition and $\Delta k = (\vec{k}_p + \vec{k}_c - \vec{k}_s - \vec{k}_{as}) \cdot \hat{z} = 0$:

$$\Gamma_{as} = \frac{2i\mathcal{N}\sigma\gamma_{13}(\omega + i\gamma_{12})}{G(\omega)}, \tag{4.25a}$$

$$g_R = \left(\frac{{\Omega_p}^2}{2\Delta\omega_{14}^2}\right)\frac{i\mathcal{N}\sigma\gamma_{13}(\omega + i\gamma_{13})}{G(\omega)}, \tag{4.25b}$$

$$\kappa_s = \kappa_{as} = -\left(\frac{\Omega_p}{2\Delta\omega_{14}}\right)\frac{i\mathcal{N}\sigma\gamma_{13}\,\Omega_c}{G(\omega)}, \tag{4.25c}$$

$$\xi_{21}^{s} = -\left(\frac{\Omega_p}{\Delta\omega_{14}}\right)\frac{\sqrt{2}(\omega + i\gamma_{13})\sqrt{\mathcal{N}\sigma\gamma_{13}}}{G(\omega)}, \tag{4.25d}$$

$$\xi_{24}^{s} = -\frac{\sqrt{\mathcal{N}\sigma\gamma_{13}}}{\sqrt{2}\Delta\omega_{14}}, \tag{4.25e}$$

$$\xi_{31}^{s} = -\left(\frac{\Omega_p}{\Delta\omega_{14}}\right)\frac{\Omega_c\sqrt{\mathcal{N}\sigma\gamma_{13}}}{\sqrt{2}G(\omega)}, \tag{4.25f}$$

$$\xi_{34}^{s} = -\frac{\Omega_c\sqrt{\mathcal{N}\sigma\gamma_{13}}}{2\sqrt{2}{\Delta\omega_{14}}^2}, \tag{4.25g}$$

$$\xi_{21}^{as} = \frac{\sqrt{2}\Omega_c\sqrt{\mathcal{N}\sigma\gamma_{13}}}{G(\omega)}, \tag{4.25h}$$

$$\xi_{24}^{as} = -\left(\frac{\Omega_p}{\Delta\omega_{14}}\right)\frac{\Omega_c\sqrt{\mathcal{N}\sigma\gamma_{13}}}{\sqrt{2}G(\omega)}, \tag{4.25i}$$

$$\xi_{31}^{as} = \frac{2\sqrt{2}(\omega + i\gamma_{12})\sqrt{\mathcal{N}\sigma\gamma_{13}}}{G(\omega)}, \tag{4.25j}$$

$$\xi_{34}^{as} = -\left(\frac{\Omega_p}{\Delta\omega_{14}}\right)\frac{\sqrt{2}(\omega + i\gamma_{12})\sqrt{\mathcal{N}\sigma\gamma_{13}}}{G(\omega)}, \tag{4.25k}$$

where $\mathcal{N}$ is an atom density, $G(\omega) = |\Omega_c|^2 - 4(\omega + i\gamma_{12})(\omega + i\gamma_{13})$, σ is the absorption cross section for all allowed transitions: $\sigma = \sigma_{14} = \sigma_{24} = \sigma_{23} = \sigma_{13}$.

4.6.1 Ground state approximation

The approximation that the atomic population remains in the ground state $\tilde{\sigma}_{11} = 1$ gives two significant diffusion coefficients $\mathcal{D}_{12,21} = 2\gamma_{12}$ and $\mathcal{D}_{13,31} = \Gamma_3$ corresponding to F_{21}, F_{31} Langevin noise operators. Due to small atomic population in the excited states, the rest of the diffusion coefficients are approximated as zeros and the corresponding Langevin noise operators are neglected [36].

We numerically examine the emission rates and intensity correlation function for the EIT based paired photon emitter. We take other parameters similar to those of a Rb MOT: atom density $\mathcal{N} = 10^{11}$ atoms per cm^3, atomic cross sections $\sigma = \sigma_{13} = \sigma_{14} = \sigma_{24} = 10^{-9}$ cm^2 and dephasing rates equal to one half of the Einstein A coefficient, i.e., $\gamma_{13} = \gamma_{14} = \gamma_{24} = \gamma_{23} = 1.79 \times 10^7$ radians. We choose the strength and the detuning of the pump laser from the $|1\rangle \rightarrow |4\rangle$ transition as $\Delta\omega_{14} = 24\gamma_{13}$ and $\Omega_p/\Delta\omega_{14} = 0.1$.

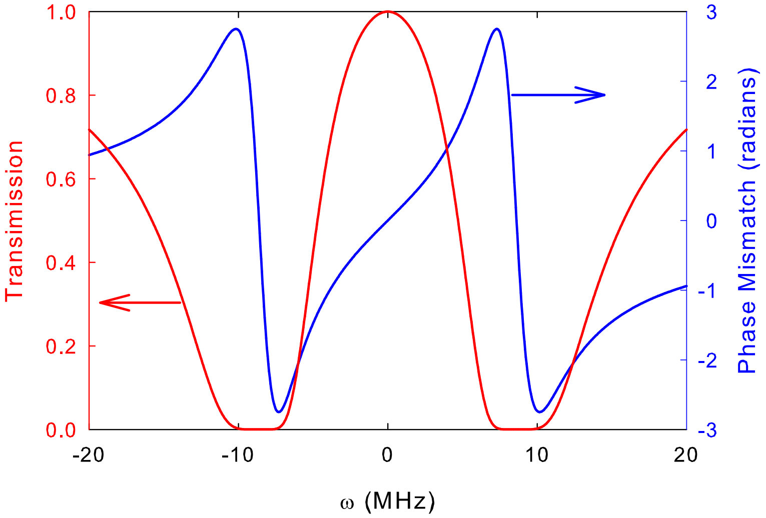

Figure 4.3: Transmission and phase mismatch as functions of detuning ω

Fig. 4.3 shows the EIT transmission profile and phase mismatch as a function of the detuning of the anti-Stokes frequency ω. We take $\Omega_c = 6\gamma_{13}$, $\mathcal{N}\sigma L = 11$ and $\gamma_{12} = 0$. Fig. 4.4 shows the profiles of the coupling coefficient $|\kappa(\omega)|$ and the Raman

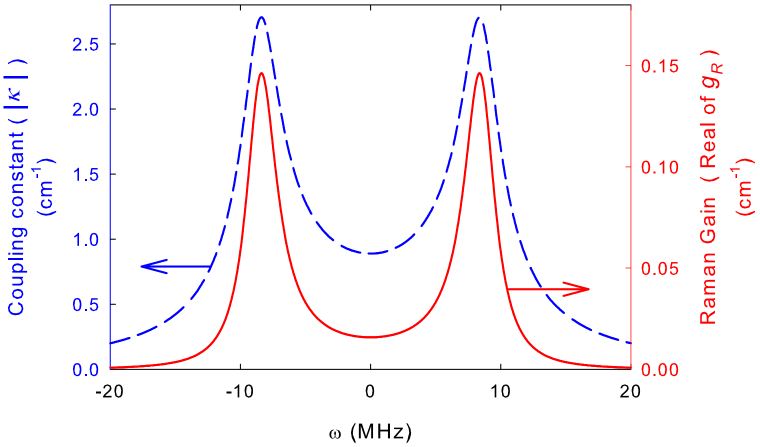

Figure 4.4: Coupling constant and Raman gain as functions of detuning ω.

gain coefficient $Re(g_R(\omega))$ for the same parameters as in Fig. 4.3.

EIT based spontaneous emitters allow a variable emission bandwidth. The bandwidth and profile of the spontaneous emission rates are controlled by the strength of the coupling laser Ω_c and the optical depth of the atomic sample $\mathcal{N}\sigma L$. By reducing the strength of the coupling laser, the emission linewidth can be made much smaller than the natural linewidth, with the minimum width ultimately limited by the dephasing rate γ_{12} of the $|1\rangle \to |2\rangle$ transition. At small optical depth $\mathcal{N}\sigma L < 1$, the Raman gain coefficient $g_R(\omega)$ and the coupling coefficients $\kappa_s(\omega)$, $\kappa_{as}(\omega)$ determine the emission spectrum. At high optical depth $\mathcal{N}\sigma L > 1$, the EIT transmission window and the phase mismatch, introduced by a large group delay in the anti-Stokes channel, affect the spontaneous emission spectrum.

In Fig. 4.5, Fig. 4.6 and Fig. 4.7 we show the variations of the coincidence count rate $R_c(\tau)$ in a 1 ns bin and the corresponding Stokes power spectral density depending on the optical depth. With a bin size $\Delta T = 1$ ns much smaller than the correlation time, the coincidence count rate is obtained from the intensity correlation function as $R_c(\tau) = \Delta T(c/L)^2 G^{(2)}_{as-s}(\tau)$. Compared to the ideal case, described earlier, the intensity correlation function and the emission spectrum for the EIT based atomic SPDC show some interesting features. The shape of the intensity correlation function

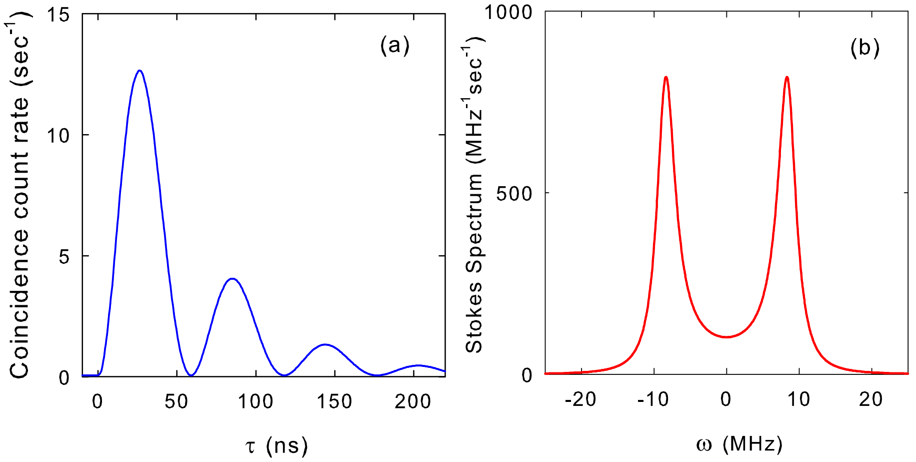

Figure 4.5: The oscillatory regime: (a) Coincidence count rate in a 1 ns bin and (b) Stokes spectral generation rate. $\mathcal{N}\sigma L = 0.3$, $\Omega_c = 6\gamma_{13}$ and $\gamma_{12} = 0$.

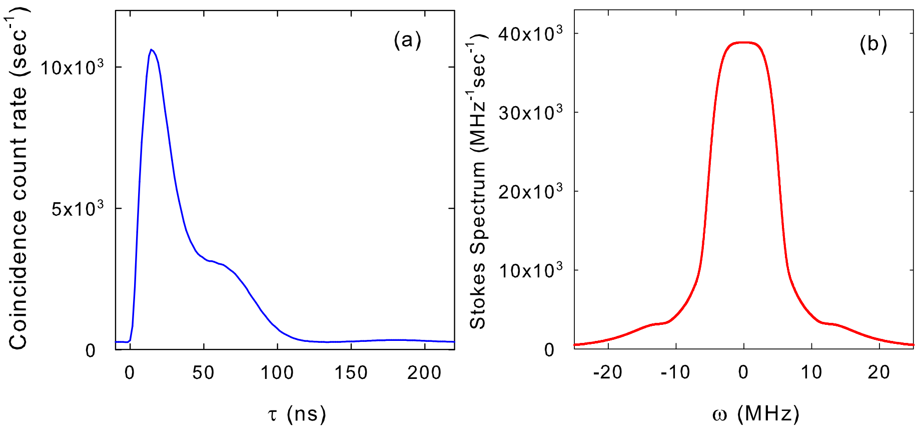

Figure 4.6: The group delay regime: (a) Coincidence count rate in a 1 ns bin and (b) Stokes spectral generation rate. $\mathcal{N}\sigma L = 20$, $\Omega_c = 6\gamma_{13}$ and $\gamma_{12} = 0$.

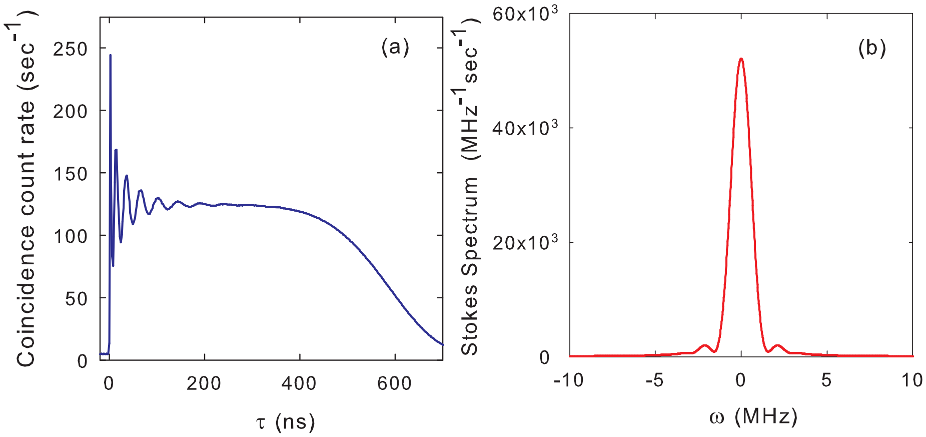

Figure 4.7: The group delay regime: (a) Coincidence count rate in a 1 ns bin and (b) Stokes spectral generation rate. $\mathcal{N}\sigma L = 200$, $\Omega_c = 6\gamma_{13}$, $\Omega_p = 0.3\gamma_{13}$ and $\gamma_{12} = 0$.

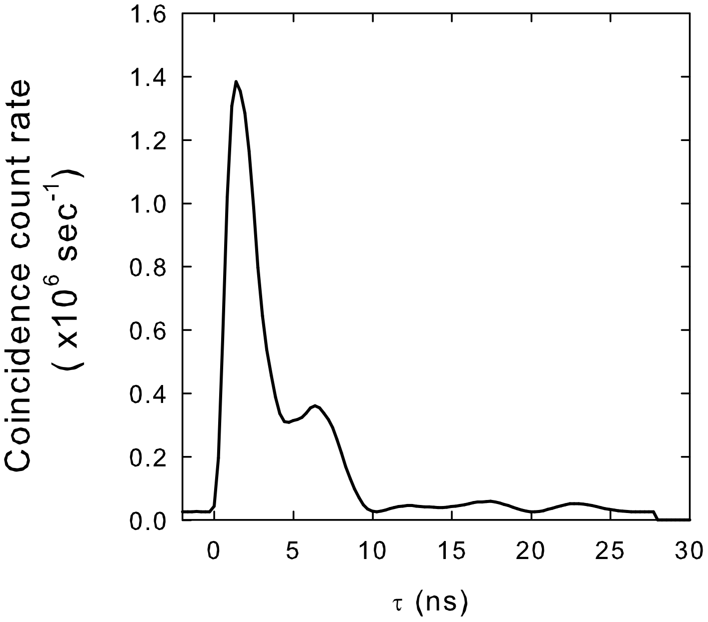

Figure 4.8: Intensity correlation function with the correlation time smaller than the spontaneous decay time, $\tau_r < \tau_g < 1/(2\gamma_{13})$. $\mathcal{N}\sigma L = 200$, $\Omega_c = 65\gamma_{13}$, $\gamma_{12} = 0$ and $1/(2\gamma_{13}) = 25$ ns.

and the emission profile depend on the relation of three characteristic times. The first is the inverse Rabi frequency of the coupling laser $\tau_r = 2\pi/\sqrt{\Omega_c^2 - \gamma_{13}^2}$, the second is the group delay between Stokes and anti-Stokes photons $\tau_g = L/V_g = 2\gamma_{13}\mathcal{N}\sigma L/\Omega_c^2$ and the third is a minimal pulse length required to pass through EIT medium [50] $\tau_{p(min)} = 8\ln(2)\gamma_{13}\sqrt{\mathcal{N}\sigma L}/\Omega_c^2$.

When the EIT effect is small, which occurs, for example, at low optical depth, the atomic system behaves like a single atom [51]. In such a regime the intensity correlation function reveals the damped Rabi oscillations (Fig. 4.5). The oscillations observed in the intensity correlation function have the time period of $\tau_r = 2\pi/\sqrt{\Omega_c^2 - \gamma_{13}^2}$ and occur on the condition that $\tau_r > \tau_g, \tau_{p(min)}$ and the coupling laser is strong enough to force the oscillations to overcome damping $\Omega_c > \gamma_{13}$. Once the metastable state $|2\rangle$ is excited by the Raman process $|1\rangle \rightarrow |4\rangle \rightarrow |2\rangle$, the probability amplitude between $|2\rangle$ and $|3\rangle$ oscillates due to the strong interaction of the atoms with the resonant coupling beam.

In Fig. 4.6 we show the intensity correlation function and Stokes emission spectrum in the group delay regime, where $\tau_g > \tau_r$ and $\tau_g > \tau_{p(min)}$. In this regime the width of the intensity correlation function is approximated by τ_g. Moreover, the frequency range over which the spontaneous generation occurs is filtered by the EIT window and mostly controlled by the phase-matching in the presence of large group delay in the anti-Stokes channel. A sufficiently wide EIT window $\tau_g > \tau_{p(min)}$ requires high optical depth $\mathcal{N}\sigma L > 10$. In the presence of the non-zero dephasing γ_{12}, the maximum group delay and therefore the maximum width of the correlation function is limited by $\sim 1/\gamma_{12}$.

By increasing the optical depth of the atomic sample, the EIT window can be made substantially larger than the emission bandwidth. A large EIT window might be very useful for such applications as bi-photon waveform control and shaping. Fig. 4.7 shows the intensity correlation function and the Stokes emission spectrum under such a condition, where $\mathcal{N}\sigma L = 200$. The tail of the correlation function decays on the time scale of $\tau_{p(min)}$.

We also note that at high optical depth it becomes possible to achieve the Stokes–anti-Stokes correlation function with the width shorter than the spontaneous decay time $1/(2\gamma_{13})$. Fig. 4.8 shows such a correlation function that is obtained for $N\sigma L = 200$ and $\Omega_c = 65\gamma_{13}$, where $\tau_r < \tau_g < 1/(2\gamma_{13})$.

We turn next to the sharp peak at the leading edge of the correlation function of Fig. 4.7. This sharp peak is Sommerfeld-Brillouin precursor [52]. It has been observed in our theoretical plots for a long time. But only recently, when it was experimentally measured, we got interested in its nature. We thank Daniel J. Gauthier who suggested that this peak is the result of simultaneously generated Stokes and anti-Stokes photons that travel at nearly the speed of light in vacuum and arrive near-simultaneously at the photodetectors. He also pointed out to the similarity of this peak to precursors which have been extensively studied [52, 53, 54]. A precursor has an approximate width that is equal to the opacity width of the atomic transition in the optically thick medium. Similar to precursors, the sharp leading edge peak has a opacity width of the EIT profile [55].

4.6.2 No ground state approximation

If the pump is weak and far detuned and therefore most of the atomic population is in the ground state, we verify that the ground state approximation gives a correct prediction for the Bi-photon function and the Stokes generation rate. Nevertheless it does not properly account for an atom return to the ground state $|1\rangle$. Ideally one would expect the Stokes and anti-Stokes rates to be equal, since an atom, making a complete cycle on the energy level diagram (Fig. 5.7), returns to the ground state. Even at zero dephasing rate $\gamma_{12} = 0$ of the $|1\rangle \rightarrow |2\rangle$ transition, the ground state approximation predicts the anti-Stokes generation rate to be smaller than the Stokes generation rate. For example, $R_{as}/R_s = 0.65$ for $\mathcal{N}\sigma L = 10$, $\Omega_p/\Delta\omega_{14} = 0.1$ and $\Omega_c = 6\gamma_{13}$.

In order to treat properly an atom's return to the ground state we will retain in Eq. (4.6) all four Langevin noise operators $\{\tilde{f}_{21}, \tilde{f}_{24}, \tilde{f}_{31}, \tilde{f}_{34}\}$ and take into account small incoherent population in excited states, resulting from the steady state solutions of Eqs. (4.27a)-(4.27f). With these inclusions the solution of Eq. (4.6) predicts the Stokes and anti-Stokes spectral generation rates to be equal at a zero dephasing rate

$\gamma_{12} = 0$ [Fig. 4.9(a)]. A non-zero dephasing rate $\gamma_{12} \neq 0$ reduces EIT and therefore introduces additional losses for anti-Stokes photons. As a result the output Stokes rate exceeds the anti-Stokes rate. For example, for $\mathcal{N}\sigma L = 10$, $\Omega_p/\Delta\omega_{14} = 0.1$, $\Omega_c = 6\gamma_{13}$ and $\gamma_{12} = 0.6\gamma_{13}$ we obtain $R_{as}/R_s \approx 0.8$. The corresponding Stokes and anti-Stokes spectral generation rates are shown in Fig. 4.9(b). We believe that the "missing" anti-Stokes photons are absorbed and are then reemitted in a solid angle of 4π. The atomic sample is assumed to be optically thin in the radial direction.

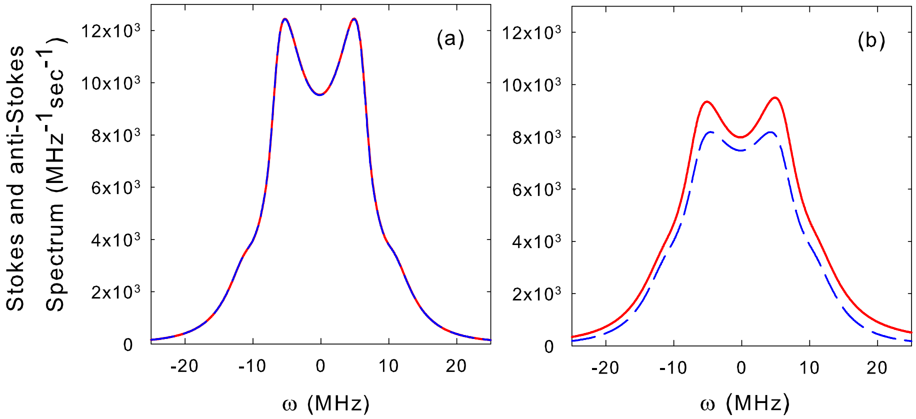

Figure 4.9: Stokes (solid curve) and anti-Stokes (dash curve) spectral generation rates at (a) zero dephasing $\gamma_{12} = 0$ and (b) non zero dephasing $\gamma_{12} = 0.6\gamma_{13}$. $\mathcal{N}\sigma L = 10$, $\Omega_c = 6\gamma_{13}$ $\Omega_p = 2.4\gamma_{13}$, $\Delta\omega_{14} = 24\gamma_{13}$

Compared to the ideal SPDC, where each generated signal photon has its paired idler photon, the real atomic system has uncorrelated noise counts in both Stokes and anti-Stokes channels that result from Langevin noise fluctuations. In Fig. 4.10 we examine the dependence of the Stokes (anti-Stokes) and paired count rates on the optical depth $\mathcal{N}\sigma L$. The parameters for the curves are $\gamma_{12} = 0$, $\Omega_c = 5\gamma_{13}$, $\Delta\omega_{14} = 24\gamma_{13}$ and $\Omega_p/\Delta\omega_{14} = 0.1$. The paired count rate (R_p) is defined as the area under the Stokes–anti-Stokes coincidence count rate function minus the area under the uncorrelated background. One may show that $R_p \approx 1/(2\pi) \int d\omega \, |AC^*|^2$. At small optical depth the paired rate scales quadratically with the optical depth and is much smaller than the Stokes rate. At high optical depth the paired rate varies linearly

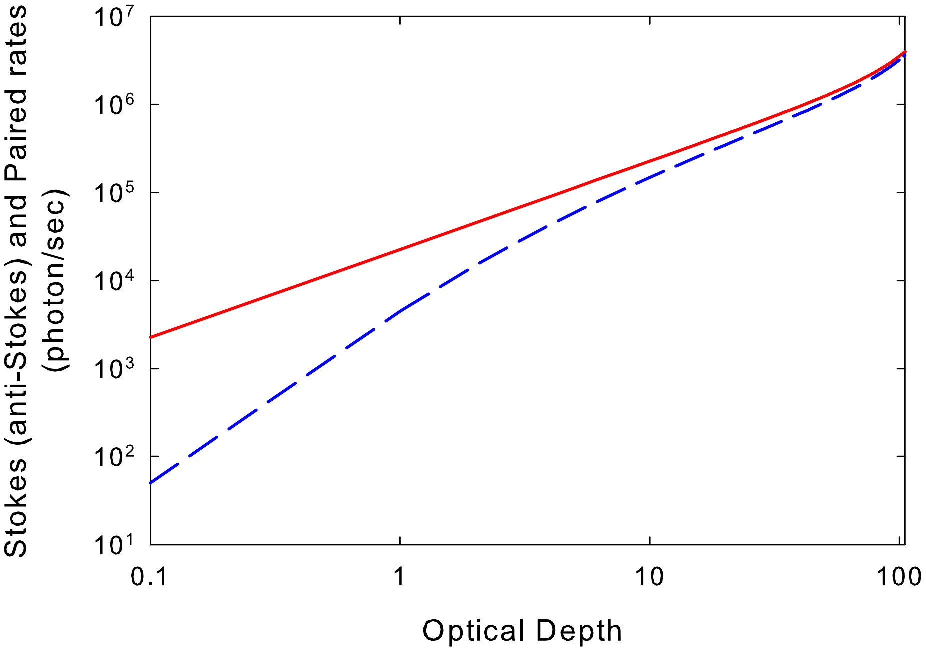

Figure 4.10: Stokes, anti-Stokes (solid curve) and Paired (dashed curve) photon generation rates as a function of the optical depth. $\Omega_c = 5\gamma_{13}$, $\gamma_{12} = 0$, $\Delta\omega_{14} = 24\gamma_{13}$ and $\Omega_p/\Delta\omega_{14} = 0.1$. At optical depth of 100, the paired rate reaches 90% of the Stokes rate.

with $\mathcal{N}\sigma L$ and converges logarithmically to the Stokes emission rate.

In this chapter we describe the theory of paired photon generation in double-Λ atomic system. With low parametric gain and high optical depth we show that the system can produce highly correlated photon pairs. The shape of the intensity correlation function and the emission bandwidth depend on the coupling laser Rabi frequency and the optical depth of the atomic sample. Compared to the ideal SPDC, paired photon generation in the double-Λ atomic system is affected by Raman gain in the Stokes channel and EIT in the anti-Stokes channel. EIT, through the absorption at the poles, cuts the emission bandwidth. In order to enter a regime where the EIT window is sufficiently large and therefore the emission bandwidth is controlled to a large extent by the phase-matching process in the presence of large group delay, the optical depth of the atomic sample has to be large $\mathcal{N}\sigma L > 10$. High optical depth substantially reduces the influence of Langevin noise fluctuations on paired photon generation so that the Stokes and anti-Stokes photons are generated mostly in pairs. We therefore suggest the use of a cigar shaped atomic cloud with high optical depth in the longitudinal direction.

4.7 Mathematical Apparatus

4.7.1 Collective slowly varying atomic operators

To describe the quantum properties of the atomic system we use the collective slowly varying atomic operators [56, 57, 58, 46, 59] $\hat{\sigma}_{jk}(z,t)$, defined as

$$\tilde{\sigma}_{jk}(z,t) = \frac{1}{N_z} \sum_{i \in N_z} |j\rangle_i \langle k| \exp\left(-i\nu_{jk} t + i k_{jk} z\right), \tag{4.26}$$

where the averaging is done over each atom i in a small interval Δz that contains large number of atoms $N_z >> 1$. The slowly varying variables are assumed to stay unchanged over Δz. $\nu_{41} = \omega_4 - \omega_1 + \Delta\omega_{14}$, $\nu_{42} = \omega_4 - \omega_2 + \Delta\omega_{14}$, $\nu_{14} = -\nu_{41}$, $\nu_{24} = -\nu_{42}$, the rest of $\nu_{jk} = \omega_j - \omega_k$. $k_{31} = \vec{k}_{as} \cdot \hat{z}$, $k_{42} = \vec{k}_s \cdot \hat{z}$, $k_{41} = \vec{k}_p \cdot \hat{z}$, $k_{32} = \vec{k}_c \cdot \hat{z}$ are the projections of the anti-Stokes, Stokes, pump and coupling k-vectors on the z axis, $k_{43} = k_{41} - k_{31}$, $k_{21} = -k_{24} + k_{41}$, the rest of $k_{jk} = -k_{kj}$.

4.7.2 Heisenberg-Langevin equations

The full set of Heisenberg-Langevin equations for the four state system consists of 16 equations. Here, we show explicitly 10 of them, the other 6 for the adjoint off-diagonal atomic operators are not shown.

$$\frac{\partial}{\partial t}\tilde{\sigma}_{44} = \tilde{F}_{44} - \Gamma_4\tilde{\sigma}_{44} + i\left(\frac{\Omega_p}{2}\tilde{\sigma}_{41} + g_s\hat{a}_s\tilde{\sigma}_{42} - g_s\hat{a}_s^\dagger\tilde{\sigma}_{24} - \frac{\Omega_p^*}{2}\tilde{\sigma}_{14}\right) \tag{4.27a}$$

$$\frac{\partial}{\partial t}\tilde{\sigma}_{41} = \tilde{F}_{41} - \left(\gamma_{41} + i\Delta\omega_{14}\right)\tilde{\sigma}_{41} + i\left(-g_{as}\hat{a}_{as}^\dagger\tilde{\sigma}_{43} + g_s\hat{a}_s^\dagger\tilde{\sigma}_{21} + \frac{\Omega_p^*}{2}\left(\tilde{\sigma}_{11} - \tilde{\sigma}_{44}\right)\right) \tag{4.27b}$$

$$\frac{\partial}{\partial t}\tilde{\sigma}_{33} = \tilde{F}_{33} - \Gamma_3\tilde{\sigma}_{33} + i\left(g_{as}\hat{a}_{as}\tilde{\sigma}_{31} + \frac{\Omega_c}{2}\tilde{\sigma}_{32} - g_{as}\hat{a}_{as}^\dagger\tilde{\sigma}_{13} - \frac{\Omega_c^*}{2}\tilde{\sigma}_{23}\right) \tag{4.27c}$$

$$\frac{\partial}{\partial t}\tilde{\sigma}_{32} = \tilde{F}_{32} - \gamma_{32}\tilde{\sigma}_{32} + i\left(-g_{as}\hat{a}_{as}^\dagger\tilde{\sigma}_{12} + g_s\hat{a}_s^\dagger\tilde{\sigma}_{34} + \frac{\Omega_c^*}{2}\left(\tilde{\sigma}_{33} - \tilde{\sigma}_{22}\right)\right) \tag{4.27d}$$

$$\frac{\partial}{\partial t}\tilde{\sigma}_{22} = \tilde{F}_{22} + \Gamma_{32}\tilde{\sigma}_{33} + \Gamma_{42}\tilde{\sigma}_{44} + i\left(-\frac{\Omega_c}{2}\tilde{\sigma}_{32} - g_s\hat{a}_s\tilde{\sigma}_{42} + g_s\hat{a}_s^\dagger\tilde{\sigma}_{24} + \frac{\Omega_c^*}{2}\tilde{\sigma}_{23}\right) \tag{4.27e}$$

$$\frac{\partial}{\partial t}\tilde{\sigma}_{11} = \tilde{F}_{11} + \Gamma_{31}\tilde{\sigma}_{33} + \Gamma_{41}\tilde{\sigma}_{44} + i\left(-g_{as}\hat{a}_{as}\tilde{\sigma}_{31} - \frac{\Omega_p}{2}\tilde{\sigma}_{41} + g_{as}\hat{a}_{as}^\dagger\tilde{\sigma}_{13} + \frac{\Omega_p^*}{2}\tilde{\sigma}_{14}\right) \tag{4.27f}$$

$$\begin{aligned}\frac{\partial}{\partial t}\tilde{\sigma}_{34} &= \tilde{F}_{34} - \left(\gamma_{34} - i\Delta\omega_{14}\right)\tilde{\sigma}_{34} \qquad (4.28a)\\ &+i\left(\frac{\Omega_p}{2}\tilde{\sigma}_{31} + g_s\hat{a}_s\tilde{\sigma}_{32} - g_{as}\hat{a}_{as}^{\dagger}\tilde{\sigma}_{14} - \frac{\Omega_c^*}{2}\tilde{\sigma}_{24}\right)\\ \frac{\partial}{\partial t}\tilde{\sigma}_{31} &= \tilde{F}_{31} - \gamma_{31}\tilde{\sigma}_{31} \qquad (4.28b)\\ &+i\left(g_{as}\hat{a}_{as}^{\dagger}\left(\tilde{\sigma}_{33} - \tilde{\sigma}_{11}\right) - \frac{\Omega_c^*}{2}\tilde{\sigma}_{21} + \frac{\Omega_p^*}{2}\tilde{\sigma}_{34}\right)\\ \frac{\partial}{\partial t}\tilde{\sigma}_{24} &= \tilde{F}_{24} - \left(\gamma_{24} - i\Delta\omega_{14}\right)\tilde{\sigma}_{24} \qquad (4.28c)\\ &+i\left(\frac{\Omega_p}{2}\tilde{\sigma}_{21} - \frac{\Omega_c}{2}\tilde{\sigma}_{34} + g_s\hat{a}_s\left(\tilde{\sigma}_{22} - \tilde{\sigma}_{44}\right)\right)\\ \frac{\partial}{\partial t}\tilde{\sigma}_{21} &= \tilde{F}_{21} - \gamma_{21}\tilde{\sigma}_{21} \qquad (4.28d)\\ &+i\left(-\frac{\Omega_c}{2}\tilde{\sigma}_{31} - g_s\hat{a}_s\tilde{\sigma}_{41} + g_{as}\hat{a}_{as}^{\dagger}\tilde{\sigma}_{23} + \frac{\Omega_p^*}{2}\tilde{\sigma}_{24}\right)\end{aligned}$$

Here, for simplicity, we assume that $\Delta k = (\vec{k}_p + \vec{k}_c - \vec{k}_s - \vec{k}_{as}) \cdot \hat{z} = 0$. In Eq. (4.27a)-Eq. (4.28d) Γ_i is the total decay rate from state $|i\rangle$, Γ_{ij} is the decay rate from state $|i\rangle$ to state $|j\rangle$ and γ_{ij} is the dephasing rate between state $|i\rangle$ and state $|j\rangle$. The dephasing rates for the double-Λ system in the absence of the collisional dephasing can be obtained from total decay rates Γ_3 and Γ_4 from state $|3\rangle$ and $|4\rangle$ to two ground states $|1\rangle$ and $|2\rangle$ as

$$\gamma_{31} = \gamma_{32} = \frac{\Gamma_3}{2} \qquad (4.29)$$

$$\gamma_{41} = \gamma_{42} = \frac{\Gamma_4}{2} \qquad (4.30)$$

$$\gamma_{43} = \frac{\Gamma_3 + \Gamma_4}{2} \qquad (4.31)$$

4.7.3 Linearization procedure

In zeroth order perturbation expansion, in which $\hat{a}_s$ and $\hat{a}_{as}$ go to zero, the Heisenberg-Langevin equations for $\tilde{\sigma}_{11}, \tilde{\sigma}_{14}, \tilde{\sigma}_{22}, \tilde{\sigma}_{23}, \tilde{\sigma}_{32}, \tilde{\sigma}_{33}, \tilde{\sigma}_{41}, \tilde{\sigma}_{44}$ atomic operators are decoupled. Under the assumption that pump and coupling beams propagate without depletion, we obtain the steady state solution for Eqs. (4.27a)-(4.27f) in form

$$\tilde{\sigma}^0_{jk} = \langle \tilde{\sigma}^0_{jk} \rangle + \sum \epsilon_{mn} \tilde{F}_{mn} \tag{4.32}$$

With the definition of the denominator as

$$T = \Gamma_{31} \left(\Gamma_4^2 + 4\Delta\omega_{14}^2 + 2\left|\Omega_p\right|^2 \right) \left|\Omega_c\right|^2 \\ + \Gamma_{42} \left(\Gamma_3^2 + 2\left|\Omega_c\right|^2 \right) \left|\Omega_p\right|^2 , \tag{4.33}$$

the steady state expectation values for the zeroth order atomic operators are equal to

$$\left\langle \tilde{\sigma}^0_{11} \right\rangle = \frac{\Gamma_{31} \left|\Omega_c\right|^2 \left(\Gamma_4^2 + 4\Delta\omega_{14}^2 + \left|\Omega_p\right|^2 \right)}{T} \tag{4.34a}$$

$$\left\langle \tilde{\sigma}^0_{22} \right\rangle = \frac{\Gamma_{42} \left(\Gamma_3^2 + \left|\Omega_c\right|^2 \right) \left|\Omega_p\right|^2}{T} \tag{4.34b}$$

$$\left\langle \tilde{\sigma}^0_{33} \right\rangle = \frac{\Gamma_{42} \left|\Omega_c \Omega_p\right|^2}{T} \tag{4.34c}$$

$$\left\langle \tilde{\sigma}^0_{44} \right\rangle = \frac{\Gamma_{31} \left|\Omega_c \Omega_p\right|^2}{T} \tag{4.34d}$$

$$\left\langle \tilde{\sigma}^0_{14} \right\rangle = -\frac{\Gamma_{31} \left(2\Delta\omega_{14} - i\Gamma_4 \right) \left|\Omega_c\right|^2 \Omega_p}{T} \tag{4.34e}$$

$$\left\langle \tilde{\sigma}^0_{23} \right\rangle = \frac{i\Gamma_3 \Gamma_{42} \Omega_c \left|\Omega_p\right|^2}{T}, \tag{4.34f}$$

In the first order expansion, we substitute the zeroth order solution for the atomic operators Eq. (4.32) into the remaining Heisenberg-Langevin equations for $\tilde{\sigma}_{21}, \tilde{\sigma}_{24}$, $\tilde{\sigma}_{31}, \tilde{\sigma}_{34}$ and their adjoint. Neglecting higher order terms like $\epsilon_{mn} \tilde{F}_{mn} \hat{a}_s$ or $\epsilon_{mn} \tilde{F}_{mn} \hat{a}^\dagger_{as}$ we obtain the linearized equations. We note that the linearized Eqs.(4.28a)-(4.28d) for $\tilde{\sigma}_{21}, \tilde{\sigma}_{24}, \tilde{\sigma}_{31}, \tilde{\sigma}_{34}$ represent an independent set of equations and can be decoupled.

For clarity we write them in vector form

$$\frac{\partial}{\partial t}\tilde{\sigma}_{\mathbf{1}} = \mathcal{A}\tilde{\sigma}_{\mathbf{1}} + \mathcal{M}\hat{\mathbf{a}} + \tilde{\mathbf{F}}_{\mathbf{1}} \tag{4.35}$$

where $\tilde{\sigma}_{\mathbf{1}} = \{\tilde{\sigma}_{21}, \tilde{\sigma}_{24}, \tilde{\sigma}_{31}, \tilde{\sigma}_{34}\}$, $\tilde{\mathbf{F}}_{\mathbf{1}} = \{\tilde{F}_{21}, \tilde{F}_{24}, \tilde{F}_{31}, \tilde{F}_{34}\}$, $\hat{\mathbf{a}} = \{\hat{a}_s, \hat{a}^\dagger_{as}\}$, matrix $\mathcal{A}$ depends on the dephasing rates γ_{jk} and pump and coupling laser rabi frequencies Ω_p, Ω_c, matrix $\mathcal{M}$ depends on the zeroth order solution for the atomic operators $\langle\tilde{\sigma}^0_{jk}\rangle$.

4.7.4 Langevin noise operators and their diffusion coefficients

By analogy with the collective slowly varying atomic operators $\tilde{\sigma}_{jk}(z,t)$, the collective Langevin noise operators are defined as

$$\tilde{F}_{jk}(z,t) = \frac{1}{N_z}\sum_{z_i\in N_z}\tilde{F}^{(i)}_{jk}(t) \tag{4.36}$$

We assume that a Langevin noise operator for a single atom is δ-correlated so that

$$\langle\tilde{F}^{(i)}_{jk}(t)\tilde{F}^{(j)}_{j'k'}(t')\rangle = \mathcal{D}^{(i)}_{jk,j'k'}(t)\delta(t-t')\delta_{ij} \tag{4.37}$$

where $\langle ... \rangle$ denotes the average over the reservoir, $\mathcal{D}^{(i)}_{jk,j'k'}(t)$ is the atomic diffusion coefficient for an i_{th} atom.

Now we consider the second order correlations for the collective Langevin noise operators

$$\langle\tilde{F}_{jk}(t,z)\tilde{F}_{j'k'}(t',z')\rangle = \frac{1}{N_z^2}\sum_{z_i\in N_z}\langle\tilde{F}^{(i)}_{jk}(t)\tilde{F}^{(i)}_{j'k'}(t')\rangle\delta_{zz'} \tag{4.38}$$

Introducing the average atomic diffusion coefficient

$$\mathcal{D}_{jk,j'k'}(t,z) = \frac{1}{N_z}\sum_{z_i\in N_z}\mathcal{D}^{(i)}_{jk,j'k'}(t) \tag{4.39}$$

the noise correlations can be expressed as

$$\langle \tilde{F}_{jk}(t,z)\tilde{F}_{j'k'}(t',z')\rangle = \frac{L}{N}\mathcal{D}_{jk,j'k'}(t,z)\delta(t-t')\delta(z-z') \tag{4.40}$$

In case $\mathcal{D}_{jk,j'k'}(t,z)$ is independent of t, in frequency domain the noise correlations are

$$\langle \tilde{F}_{jk}(\omega,z)\tilde{F}_{j'k'}(\omega',z')\rangle = \frac{L}{2\pi N}\mathcal{D}_{jk,j'k'}\delta(\omega+\omega')\delta(z-z') \tag{4.41}$$

The diffusion coefficients $\mathcal{D}_{jk,j'k'}$ can be obtained from the Heisenberg-Langevin equations (4.27a)-(4.28d) using the generalized fluctuation-dissipation theorem [60, 61]. Here we show the diffusion coefficients for the Langevin noise operators of interest $\tilde{F}_{21}, \tilde{F}_{24}, \tilde{F}_{31}, \tilde{F}_{34}$ and their adjoint $\tilde{F}_{12}, \tilde{F}_{42}, \tilde{F}_{13}, \tilde{F}_{43}$

$$\mathcal{D}_{\alpha_i,\alpha_j^\dagger} = \begin{pmatrix} 2\langle\tilde{\sigma}_{22}\rangle\gamma_{12} + \langle\tilde{\sigma}_{33}\rangle\Gamma_{32} + \langle\tilde{\sigma}_{44}\rangle\Gamma_{42} & 0 & \langle\tilde{\sigma}_{23}\rangle\gamma_{12} & 0 \\ 0 & \langle\tilde{\sigma}_{22}\rangle\Gamma_4 + \langle\tilde{\sigma}_{33}\rangle\Gamma_{32} + \langle\tilde{\sigma}_{44}\rangle\Gamma_{42} & 0 & \langle\tilde{\sigma}_{23}\rangle\Gamma_4 \\ \langle\tilde{\sigma}_{32}\rangle\gamma_{12} & 0 & 0 & 0 \\ 0 & \langle\tilde{\sigma}_{32}\rangle\Gamma_4 & 0 & \langle\tilde{\sigma}_{33}\rangle\Gamma_4 \end{pmatrix}, \tag{4.42}$$

$$\mathcal{D}_{\alpha_i^\dagger,\alpha_j} = \begin{pmatrix} 2\langle\tilde{\sigma}_{11}\rangle\gamma_{12} + \langle\tilde{\sigma}_{33}\rangle\Gamma_{31} + \langle\tilde{\sigma}_{44}\rangle\Gamma_{41} & \langle\tilde{\sigma}_{14}\rangle\gamma_{12} & 0 & 0 \\ \langle\tilde{\sigma}_{41}\rangle\gamma_{12} & 0 & 0 & 0 \\ 0 & 0 & \langle\tilde{\sigma}_{11}\rangle\Gamma_3 + \langle\tilde{\sigma}_{33}\rangle\Gamma_{31} + \langle\tilde{\sigma}_{44}\rangle\Gamma_{41} & \langle\tilde{\sigma}_{14}\rangle\Gamma_3 \\ 0 & 0 & \langle\tilde{\sigma}_{41}\rangle\Gamma_3 & \langle\tilde{\sigma}_{44}\rangle\Gamma_3 \end{pmatrix}, \tag{4.43}$$

where α_i denotes $\{21, 24, 31, 34\}$ subspace for the atomic operators, $\alpha_i^\dagger$ denotes $\{12, 42, 13, 43\}$ subspace for the adjoint atomic operators.